



UNIVERSITA' DEGLI STUDI DI PADOVA

SCUOLA DI SCIENZE

Dipartimento di Geoscienze
Direttore Prof. Fabrizio Nestola

Tesi di Laurea Magistrale in Geologia e Geologia Tecnica

**SURFACE WAVE METHOD AND ELECTRICAL
SURVEYS FOR THE CHARACTERIZATION OF A
LANDFILL SITE**

Relatore: Prof. Jacopo Boaga
Correlatori: Dott.ssa Ilaria Barone
Prof. Adrian Flores-Orozco

Laureando: Alberto Carrera

ANNO ACCADEMICO 2018/2019

*“Excellence is an art won by training and habituation:
we do not act rightly because we have virtue or excellence,
but we rather have these because we have acted rightly [...]*
We are what we repeatedly do. Excellence, then, is not an act but a habit.”

Will Durant, *The Story of Philosophy* (1926)

Ringraziamenti

al mio relatore Jacopo Boaga, per la premura e la gentilezza, la competenza e l'aiuto fornitomi durante lo sviluppo di tutto il lavoro. Il suo interessamento ha reso possibile questa esperienza che, nell'ambito del progetto Erasmus+, ha fortemente contribuito alla mia crescita personale e professionale;

al mio co-relatore Adrian Flores-Orozco, per la pazienza, le conoscenze (e gli ottimi vini) che ha condiviso con me. La sua devozione per il lavoro ed il continuo mettermi alla prova, hanno generato in me molti stimoli ed entusiasmo. Grazie alla fiducia e alle responsabilità che fin da subito mi ha affidato, ho acquisito conoscenze e migliorato le abilità di pianificazione e gestione degli imprevisti;

alla dott.ssa Ilaria Barone, co-relatrice di questa tesi ed artefice di script eccezionali e risolutivi. La sua chiarezza e prontezza nelle spiegazioni, nonché il suo rendersi sempre disponibile, mi hanno permesso di affrontare con precisione tutti i problemi;

al magnifico team della TU-Vienna: Timea, sempre attenta ad affrontare e risolvere con me dubbi e problemi di programmazione; Philipp e Stefan, miei fedeli colleghi di campagna; Walter e Sonja, braccio e mente organizzative; Matthias e Jakob, mattinieri e altruisti; Theresa e Martin, coi quali ho instaurato un rapporto speciale e collaborato a progetti in posti magnifici;

ai miei Amici, quelli veri, che hanno condiviso gioie e difficoltà durante tutto questo percorso;

a tutte le persone, quelle rimaste e quelle andate, con cui ho vissuto momenti ed esperienze che mi hanno portato ad essere quello che sono;

ai miei carissimi nonni Giuseppe ed Adriana, per il loro amore ed il continuo interessamento;

ai miei genitori e a mio fratello Aki, che mi hanno supportato, sopportato e sostenuto in ogni momento;

GRAZIE

Abstract

Nel contesto di questa tesi di laurea Magistrale, una serie di diverse tecniche geofisiche (ERT, IP, EMI e MASW) è stata adottata con l'obiettivo di determinare la struttura interna e la distribuzione dei materiali riguardanti la discarica Heferlbach situata nella cittadina di Mannswörth, Lower Austria. L'area in studio risulta essere un meandro abbandonato del Danubio, situato qualche centinaia di metri a nord, che è stata poi riempita di rifiuti solidi urbani e materiali di scarto edilizi tra gli anni '60 e '70 e di cui si possiedono scarse informazioni.

Un insieme di sondaggi elettrici ed elettromagnetici, organizzati dal Geophysical Research group della TU Vienna, è stato condotto e ripetuto tra il 2017 ed il 2019 nell'area in studio con l'intento di monitorare il contenuto di gas e percolato generatisi dai processi biogeochimici e per fornire informazioni utili alla gestione della minaccia ambientale. Queste tecniche sono da tempo applicate con successo allo studio di problematiche idrogeologiche, alla caratterizzazione di contaminanti e al monitoraggio di discariche. Tuttavia, se paragonato a precedenti lavori, l'introduzione e l'applicazione delle onde superficiali a fianco dei più classici metodi legati all'investigazione delle proprietà elettriche del sottosuolo, ha permesso una migliore comprensione ed interpretazione dei risultati.

Ancora una volta, come ampiamente riconosciuto, l'utilizzo combinato di diverse tecniche d'indagine geofisica permette di ottenere informazioni più accurate e quindi di creare un modello più veritiero del sottosuolo, specialmente dove l'area investigata risulta piuttosto eterogenea e complessa.

La parte principale di questo lavoro e l'intera attività di campagna sono state realizzate in concomitanza del periodo di Erasmus+ traineeship, svolto durante il secondo semestre dell'anno accademico 2018/2019 presso il Geophysics Research Institute della Technische Universität Wien, Department of Geodesy and Geoinformation.



TECHNISCHE
UNIVERSITÄT
WIEN
Vienna University of Technology

Index

Abstract	4
1 Introduction and site description	7
1.1 Case study: “Heferlbach”	8
2 Geophysical methods	11
3 Surface Wave Method	12
3.1 Theoretical background.....	13
3.1.2 Stress, strain and wave motion	14
3.1.3 Surface Waves	17
3.1.4 Physics	18
3.1.5 Geometric dispersion	21
3.1.6 Method.....	22
3.2 Survey configuration and field measurements	24
3.2.1 Acquisition.....	25
3.2.2 Equipment	26
3.2.3 Sampling and windowing	28
3.2.4 Measuring protocol	30
3.3 Processing and Inversion.....	32
3.3.1 Data analysis and dispersion curves.....	33
3.3.2 Modeling and data inversion.....	36
4 Geoelectrical Methods	38
4.1 Electrical Resistivity Method	38
4.1.1 Theoretical background.....	38
4.1.2 Electrical properties of rocks.....	39
4.1.3 Physics	40
4.1.4 Single electrode.....	41
4.1.5 Multiple electrodes	42
4.1.6 Electrode arrays.....	44
4.2 Induced Polarization.....	45
4.2.1 Theoretical background.....	46
4.2.2 Methods	47
4.2.3 Time-domain IP	48
4.2.4 Frequency-domain IP	49

4.2.5 The complex conductivity	51
4.3 Survey configuration and field measurements	52
4.3.1 Acquisition.....	52
4.3.2 Measuring protocol.....	53
4.3.3 Pseudosection	55
4.4 Processing and Inversion.....	56
4.4.1 Quantification of data error	56
4.4.2 Modeling and data inversion	59
5 Electromagnetic Induction Methods	62
5.1 Theoretical background	63
5.1.1 Methods	65
5.1.2 Electromagnetic methods at low induction number	66
5.1.3 Low induction number electromagnetic imaging	67
5.1.4 Attenuation and Skin Effect	70
5.2 Survey configuration and field measurements	71
5.2.1 Acquisition.....	71
5.2.2 Measuring protocol.....	72
5.3 Processing and results.....	73
6 Results and Discussions.....	75
6.1 EMI	75
6.2 ERT & IP	77
6.3 Surface Waves.....	79
7 Conclusions.....	81
Table of Figures.....	82
Bibliography	85

1 Introduction and site description

Environmental contamination is definitely the worst legacy of the contemporary society and matter of concern for the biodiversity on our planet Earth. The accelerated rhythm of industrial development, on top of a boundless growth of the urban population coupled with a consumerist economic policy, has resulted in the increasing production of various types of residues.

To remedy this were set up landfills, installations for the storage of waste in the subsurface for an indefinite period of time, provided with the constructive measures to avoid contaminations. As they are often located near urban areas and their influence extends into the surrounding environment, it becomes essential monitoring them.

However, urban waste materials (e.g. domestic garbage, plastic packages, burned oils) are usually disposed without the appropriate measures imposing a high risk to the underground water resources, especially in the third-world countries.

In several part of Europe, unofficial and now abandoned landfills were in use until the 1960s and 1970s. Their precise geometry and composition are often unknown, as well as their internal processes and resulting short- and long-term risks. As a result, these areas are often poorly understood and only monitored by measuring surrounding groundwater composition.

Ground-water pollution happens mostly due to percolation of pluvial water coupled with the infiltration of contaminants through the soil. The decomposition of organic matter produces fluids rich in dissolved salts, containing a substantial amount of polluting substances. During this process, leachates which carry toxic products are formed and for their management, a collection and transportation system, is necessarily required.

Nevertheless, if this resulting contaminant liquid reaches the aquifer, it affects the potability of underground water putting in serious danger the local community health. Hence, one of the most common demands in metropolitan areas comprises the detection of location and extent of pollutant patches in more or less engaged areas.

In such a context, the integrated use of various geophysical methods provides an important tool for the evaluation and characterization of contaminants generated by domestic and/or industrial residues. Their non-destructive nature, economy, and speed makes them advantageous and preferable rather than punctual and high-priced information derived from borehole drilling. In this regard, both drilling and excavation can be dangerous for the operators and the environment because their destructive character can facilitate the extension of the existing leachate at the bottom of the landfill. Electrical and electromagnetic methods have been found remarkably suitable for such environmental studies, due to the conductive nature of most contaminants.

Degradation of organic pollutants in acids and metabolic products triggers also an increasing in the polarization effect due to electrochemical processes at the interface

contaminant-groundwater and contaminant-grain. The elevated signature can be used to locate waste, delineate its boundaries and provide a rough estimate of its depth.

In the current work, we combined electrical resistivity tomography (ERT), induced polarization (IP), multi-channel analysis of surface waves (MASW) and low-induction number electromagnetic method (EMI) in order to investigate inner heterogeneities, assess mechanical properties and identify contaminant spots. Moreover, it is shown how important and useful is the integrated application of different methods, everyone planned to hit different sub-targets.

The objective of this work is to obtain information on lateral and in-depth changes into a landfill, related to changes in geometry, variation in composition, as well as anthropogenic structures such as drainage pipes, which were placed throughout the landfill and used for aeration and/or leachate transport system. A further purpose is to deepen the general procedure behind the surface waves method and moreover to test its ability in improving the characterization of a shallow contaminated site.

1.1 Case study: “Heferlbach”

The "Heferlbach" landfill (Fig. 1.1) is located to the north end of Mannswörth (Niederösterreich), a town 15km far away from Vienna and 700 m south to the Danube river.



Fig. 1. 1, Heferlbach landfill in Mannswörth, Niederösterreich, and the south-east investigated area

The site, whose name come from its origin as a meander lake of the Danube, was filled from 1965 to 1974 with 240.000 m³ including top soil and is characterized by an average height of 3.7 m [55, Valtl, M. 2005].

Information on the distribution of materials with depth are available from the dozens of samples collected since the 2012: the filling material occupies a volume of approximately 220.000 m³ and consists in municipal solid waste, excavated soil and construction and demolition waste (Fig. 1.2). The soil level is approximately 150m above the sea level.

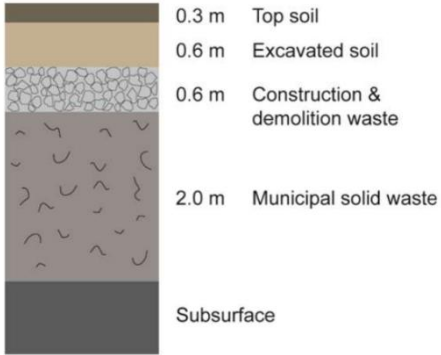


Fig. 1. 2, Average depth profile of the landfill Heferlbach, from Brandstätter et al. 2013

This profile (Fig. 1.2) illustrates the different layers of cover material and waste deposited at the site. The area lies between alluvial deposits of the Danube and terraces formed during the last ice age. The subsoil lies on top of quaternary gravels, which represent a rich aquifer, and 10m below it another groundwater reservoir is represented by tertiary sands.

The groundwater level in the landfill area is determined by water abstraction from wells (subsidence up to approx. 2 m) and in recent years has been pumped mostly under the landfill bottom. As a consequence, the residual water has become the leading cause of leachate generation and bacterial proliferation, to which is tied the biogas production (Fig. 1.3).

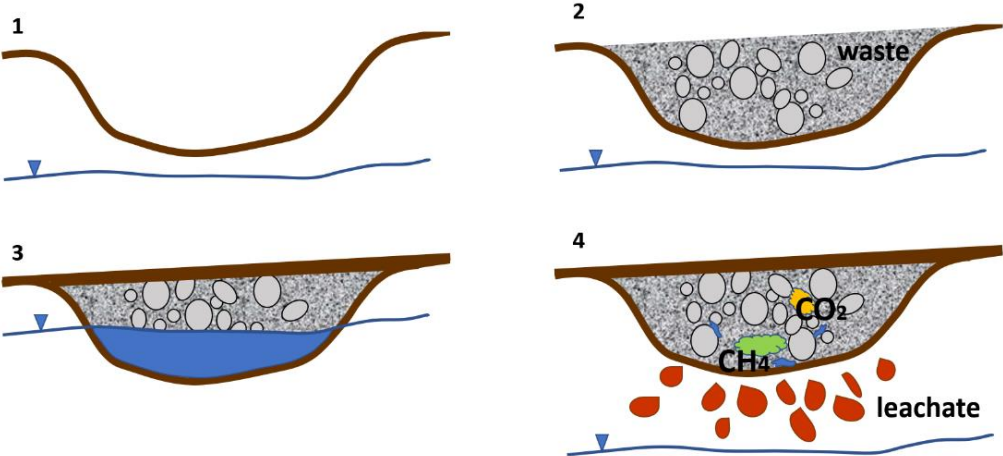


Fig. 1. 3, Schematic evolution and consequent production of leachate and biogas in Heferlbach landfill

The degradation of organic substances led to a high level of gas production with methane CH₄ contents of up to 53 % by volume and Carbon dioxide CO₂ content of up to 45 % by volume in soil air. As depicted in Brandstätter et al. 2013, the landfill was subjected to an in-situ aeration treatment to accelerate the biological stabilization and to reduce the gas production potential. However, even though the aeration system installed, residential buildings located partly on the landfill or close to it (Fig. 1.4), are potentially exposed to gas intrusion and consequently explosion hazards. Either way, due to the low leachate pollution strength, its environmental threat was considered to be of minor importance at this site.

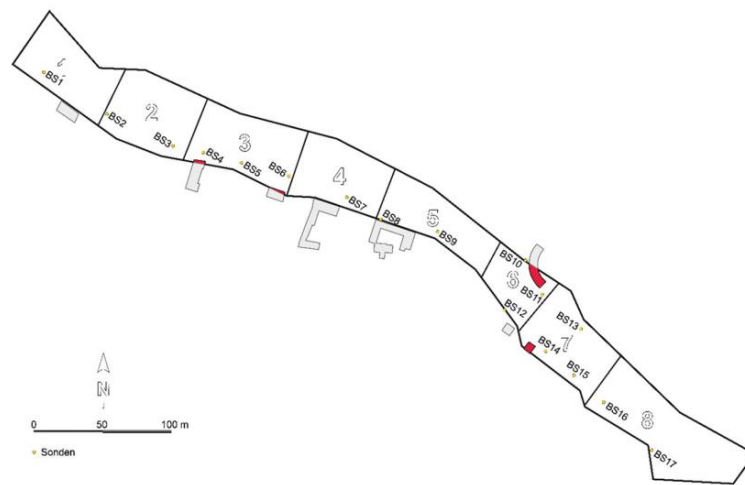


Fig. 1. 4, General plan of the Heferlbach landfill, from Brandstätter et al. 2016

Currently, in the area there is a children's playground, two parking lots, a special waste storage center, a flood control dam and, in the peripheral areas, residential buildings and a sports field. The remaining areas are used for agriculture, some lie fallow and some have been reforested.

2 Geophysical methods

The purpose of applied geophysics is to provide the subsurface site characterization of the geology, geological structure, groundwater, contamination, and human artifacts beneath the Earth's surface. The investigation of subsurface conditions in the Earth through measuring, analyzing and interpreting physical fields at the surface is based on the lateral and vertical mapping of physical property variations that are remotely sensed using non-invasive technologies.

The main geophysical prospection methods are generally subdivided in two groups: active and passive. In the first, an active source energizes properly the ground and the receivers detect the variations of some physical quantities. In the latter, intrinsic physical quantities variations are picked up without the necessity of artificial energization.

There are also covered destructive methods, based on the drill of boreholes into the ground that allow to supply important information about the stability and geotechnical parameters of the subsurface (rock density, velocity of elastic waves, shear modulus and Poisson's ratio).

Many of the geophysical technologies are traditionally used for exploration of economic materials such as groundwater, metals, and hydrocarbons. Recently, as the aftereffects of industrialization and ecological negligence become more evident, sustainable development and awareness in natural conservation promoted the implementation of methodologies and technologies to address the growing need for environmental assessment, monitoring and remediation.

During the field work has been applied four different active geophysical techniques aimed at a landfill characterization. In the following chapter, surface wave methods (MASW) will be introduced, then electrical resistivity tomography (ERT) and induced polarization (IP) methods and, to conclude, electromagnetic method (EM) at low induction number.

Each section starts with the physics behind the method, subsequently the instruments used and the field configurations are tackled. In conclusion, a description of the data analysis and the processing techniques is filed.

3 Surface Wave Method

During the last decade, surface-wave analysis has attracted the interest of researchers embracing different disciplines and, as an early young technique, is under continuous and rapid evolution.

Firstly discovered in the late XIX century by Lord Rayleigh, the lively scientific debate nowadays allowed the improvement and development of surface waves-methods.

From geophysics to engineering, passing through material science, geotechnics and acoustics, the main goal is to exploit surface waves propagation along the boundary of a domain to obtain information about the interior of that domain.

Seismic methods for site characterization are often divided into two broad categories:

- *invasive* tests (e.g. cross-hole, down-hole, cone penetration test, dilatometer test)
- *noninvasive* tests (e.g. seismic reflection, seismic refraction and surface wave tests)

Noninvasive tests are generally affected by more uncertainty, but they allow the exploration of larger, more representative volumes, and they are usually cheaper. Firstly developed using P-waves, they are currently used also with S-waves, although there are some difficulties in generating high-energy, horizontally polarized shear waves.

The wave field is complex, with multiple wave types and complex propagation paths (Fig. 3.1). Thus, seismic records are analyzed and processed to estimate the properties of different wave types and to identify them in each single trace recorded. In near surface explorations, recording simultaneously with a plurality of receivers at different locations allows the wave propagation to be observed in space and time. The acquired set of multiple traces, called seismic record or multichannel seismogram, represents the effects of the propagating wave field at different locations.

As a noninvasive technique, the geometric dispersion analysis of surface waves, together with the solution of an inverse problem for parameter identification, permit to infer the relevant medium properties in a wide range of scales (mm – km).

Concerning near-surface site characterization, the objective is to determine the shear-wave velocity and the damping ratio distributions through a properly planned acquisition. From the dispersion curve, the relationship between phase velocity and frequency we obtain a vertical profile of shear waves velocity, used e.g. for seismic hazards microzonation or to infer the mechanical properties of the medium.

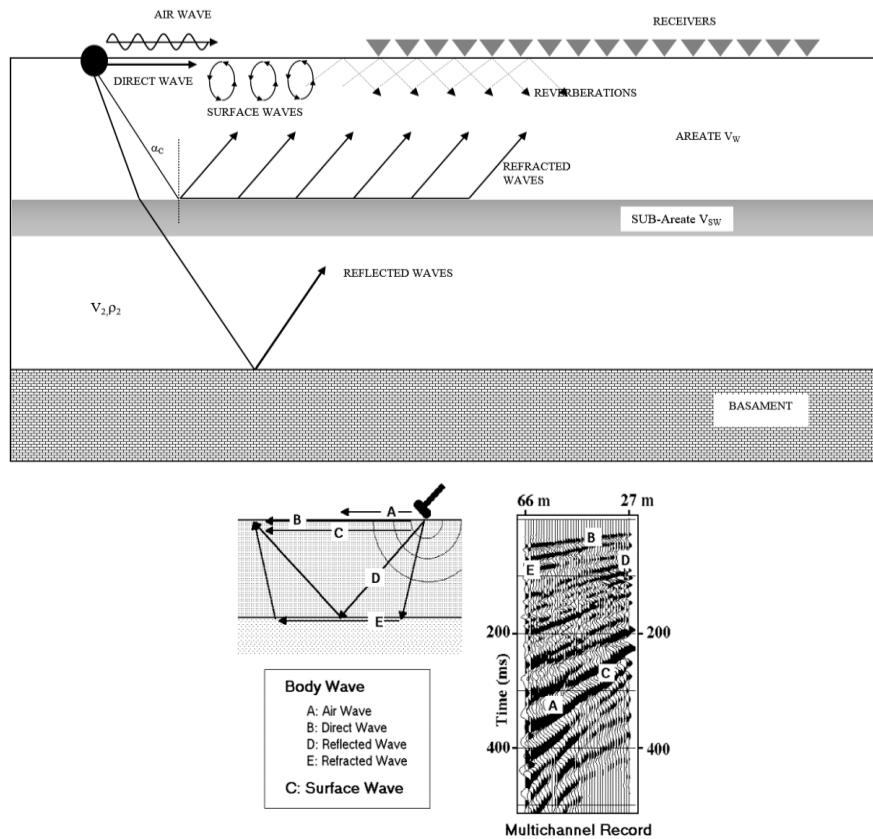


Fig. 3. 1, Up: schematic representation of various types of seismic events generated simultaneously by an impact applied to the Earth surface. Down: an example of field multichannel record (shot gather) is displayed, with identified events marked on it. From Cassiani, G. lectures and Park et al., 2001)

3.1 Theoretical background

The propagation of mechanical energy into the subsurface involves, in a wide part, elastic waves. When a stress, the ratio of a concentrated force to unit of area, is applied to an elastic body, the corresponding deformation pattern called strain is propagated outwards as an elastic wave. This particular case, in which the deformation at every point is a linear homogeneous function of the stress in the same point, is called perfect elasticity and it is described by Hooke's Law. Although it is only an approximation of the real world, many seismic waves properties are fulfilling described through this theory.

Soils and rocks are complex, multiphase, composite and discontinuous materials, thus, their mechanical behavior cannot in general be described using simple models, depending on a variety of factors. Nevertheless, continuum mechanics approaches are frequently used, including linear elastic constitutive models. This last assumption seems reasonable for very small strains, where soils exhibit an almost linear stress-strain relationship: this is the case of geophysical testing, so it is widely accepted that linear elastic theory provides a consistent framework for the interpretation of seismic tests. Besides, small-strain parameters play a significant and relevant role for a wide range of geotechnical problems.

Seismic waves, which consist of tiny packets of elastic strain energy, propagate from any seismic source at speeds determined by the elastic moduli and the densities of the media through which they pass. The effect of a sharply applied, localized disturbance in a physical medium rapidly spreads in space: this is commonly addressed as wave propagation. Every perturbation generates two main types of seismic waves: those that pass through the bulk of a medium are known as body waves; those confined within the interfaces between media with contrasting elastic properties, particularly the ground surface, are called surface waves.

Two different types of body waves propagate in an unbounded, homogeneous, and linear elastic medium: P-waves (primary or compressional waves) and S-waves (secondary or shear waves). The firsts are the fastest and propagate with particle motion in the same direction of the propagation, causing volume change without distortion. In the latter, the particle motion is perpendicular to the direction of propagation (Fig. 3.2).

Surface waves too are of several types, but the two most common are Rayleigh and Love waves. Their treatment it is meant to come in the next section (3.1.3).

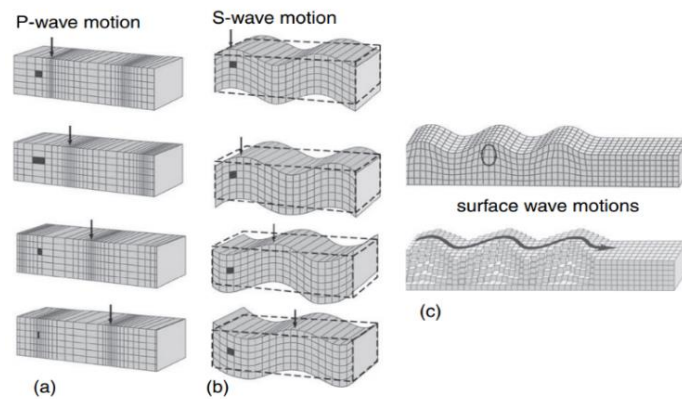


Fig. 3. 2, Particle motion associated with the propagation of seismic waves: (a) compressional, (b) shear, (c) Rayleigh (top) and Love (bottom) waves, from Everett, Mark E. 2013

3.1.2 Stress, strain and wave motion

A brief overview of elasticity theory is presented in this section. For more complete treatments see [54, Telford et al.].

To determinate the wave motion and the related seismic velocities caused by a stress σ [$\text{Pa}=1/\text{Nm}^2$] upon an elastic body, it is useful to start with the case of a uniaxial tension state ($\sigma_{yy} = \sigma_{zz} = 0$).

Strain ϵ is a dimensionless quantity defined as the fractional change in the size and shape of a body subject to loading.

In line with Hooke's Law, a linear relationship occurs between stress and strain and the body behaves elastically until a yield point is reached. Below the yield point, the body returns instantaneously to its original pre-deformed state once the acting force is

removed. At subsequent higher stresses, the body is permanently modified, behaving in a plastic or ductile manner, until it fractures.

In a Cartesian system, the relationship applies:

$$\sigma_{xx} = \varepsilon_{xx}E \quad (3.1)$$

where σ_{xx} [Pa] is the normal stress (or pressure), ε_{xx} [m/m] is the relative increase in length along the x-axis and the Young's modulus E [N/m²] is a measure of the longitudinal stress to the longitudinal strain. It is also possible to introduce the Poisson's ratio $\nu = -\varepsilon_{zz}/\varepsilon_{xx}$ that is a dimensionless measure of the transverse to longitudinal strain.

In an isotropic medium, assuming a pluriaxial stress state ($\sigma_{yy} = \sigma_{zz} \neq 0$), Hooke's law is written as:

$$\sigma_{ii} = \lambda\theta + 2\mu\varepsilon_{ii}E \quad , \text{ for } i = x, y, z \quad (3.2)$$

The quantities λ and μ are known as the Lamé parameters: the shear modulus $\mu = E/2(1+\nu)$, determines the amount of shear strain that develops in response to a given applied shear stress.

The parameter $\lambda = \nu E/(1+\nu)(1-2\nu)$ is not often used in applied geophysics. Of more practical importance is the bulk modulus K [N/m²]

$$k = \frac{3\lambda + 2\mu}{3} \quad (3.3)$$

which provides a measure of the resistance of a material to a uniform compressive stress.

The dilatation θ of a body is its fractional change in volume:

$$\theta = \frac{\Delta V}{V} = \varepsilon_{xx} + \varepsilon_{yy} + \varepsilon_{zz} \quad (3.4)$$

Therefore, it is possible to rewrite the (3.2) in tensor shape, for a generic reference system:

$$\sigma_{ij} = \lambda\theta\delta_{ij} + 2\mu\varepsilon_{ij} \quad (3.5)$$

where δ_{ij} is called Kronecker's delta and assume the values $\delta_{ij} = 0$ if $i \neq j$ or $\delta_{ij} = 1$ if $i = j$.

Suppose now to re-write Newton's law $\mathbf{F} = m\mathbf{a}$ in an infinitesimal way:

$$\rho \frac{\partial^2 v}{\partial t^2} = \frac{\partial \sigma_{xx}}{\partial x} + \frac{\partial \sigma_{xy}}{\partial y} + \frac{\partial \sigma_{xz}}{\partial z} \quad (3.6)$$

where ρ [kg/m³] is the density and v the velocity [m/s], we can substitute the Hooke's law for homogeneous media into the equation of motion (3.6) in terms of displacement \mathbf{u} :

$$\rho \frac{\partial^2 v}{\partial t^2} = (\lambda + \mu)\nabla\theta + \mu\nabla^2\mathbf{u} \quad (3.7)$$

where $\nabla^2 = \partial^2/\partial x^2, \partial^2/\partial y^2, \partial^2/\partial z^2$ is the Laplace operator, which indicates the divergence of the gradient of a function on Euclidean space.

Adding the results of the differentiated equations for the displacements in x,y and z directions together, we gain

$$\rho \frac{\partial^2 \theta}{\partial t^2} = (\lambda + 2\mu) \nabla^2 \theta \quad (3.8)$$

which is the wave equation for the dilation θ , with velocity

$$V_p = \sqrt{(\lambda + 2\mu)/\rho} \quad (3.9)$$

The associated waves are called compressional, or P-waves, and V_p is the P-wave velocity.

If we take the curl, the infinitesimal rotation of a vector field in three-dimensional Euclidean space, of each member of (3.7), we get a second wave equation

$$\rho \frac{\partial^2 \mathbf{v}}{\partial t^2} (\nabla \times \mathbf{u}) = \mu \nabla^2 (\nabla \times \mathbf{u}) \quad (3.10)$$

that depicts a rotational perturbation with velocity

$$V_s = \sqrt{\mu/\rho} \quad (3.11)$$

These waves are called shear, or S-waves, and V_s is the S-wave velocity.

Notice that V_p is always bigger than V_s and, because only μ is involved, shear waves can't propagate through liquids.

It is worthwhile to look at relationships amongst the seismic velocities and the elastic moduli mentioned earlier. Replacing the Lamé parameter λ and re-organizing the formulas we get:

$$V_p = \sqrt{\frac{k + 4\mu/3}{\rho}} = \sqrt{\frac{(1-\sigma)E}{(1+\sigma)(1-2\sigma)\rho}} \quad (3.12)$$

$$V_s = \sqrt{\frac{\mu}{\rho}} = \sqrt{\frac{E}{2\rho(1+\sigma)}} \quad (3.13)$$

$$\frac{V_p}{V_s} = \sqrt{\frac{2(1-\sigma)}{(1-2\sigma)}} \quad (3.14)$$

These equations form the basis for the use of seismic waves in material characterization. Indeed, their propagation rates through a linear elastic solid rely on medium's mechanical parameters as elastic modulus and density. In particular, V_p is associated with the (small-strain) longitudinal modulus and is strongly influenced by the compressibility of the pore fluid rather than the soil skeleton, whereas V_s is associated with the (small-strain) shear modulus and is only linked to the change in mass density because the pore fluid has no shearing resistance.

Empirical relationships as Nafe-Drake [33, Nafe & Drake 1957], relating P-wave velocity and density of water-saturated sediments, and Wyllie’s mixing law [57, Wyllie et al. 1958], have been widely used in exploration and crustal-scale geophysics. The latter expresses the seismic P-wave traveltimes ($\sim 1/V_{bulk}$) in a fluid-saturated medium as the porosity-weighted average of the P-wave traveltimes in the fluid and solid constituents:

$$\frac{1}{V_{bulk}} = \frac{\phi}{V_{fluid}} + \frac{1-\phi}{V_{solid}} \quad (3.15)$$

where $\phi = V_{voids}/V_{tot}$ indicates the porosity, the fraction of void space in the material.

P-wave velocities of selected geomaterials are shown in Fig. 3.3: the wide ranges are due to heterogeneities and variations in lithology and saturation.

	Velocity [m/s]		Velocity [m/s]
Air	330	Sandstone	1500–4500
Sand (dry)	200–800	Ice	3000–4000
Clay	1100–2500	Limestone	2500–6500
Sand (saturated)	800–1900	Granite	3600–7000
Water	1450	Basalt	5000–8400

Fig. 3. 3, Seismic compressional wave velocities, from Everett, Mark E. 2013

Although the most common application is the measurement of seismic wave velocities, it has been growing the interest in measure the attenuation of waves and to compute the material damping ratio of soils and geotechnical site characterization.

3.1.3 Surface Waves

Many types of seismic surface waves (e.g. Rayleigh, Love, Scholte, Lamb, and Stoneley waves), typically originated from the condition of vanishing stress at a boundary of a domain, are generally guided and highly dispersive. Recognition of these properties drove, since the late 1970s, to ground stiffness measurements using Spectral Analysis of Surface Waves (SASW) developed by Nazarian and Stokoe [34, Nazarian & Stokoe 1984]. This two-receiver approach imposes limitations on the measured frequency range, thus, the experimental dispersion curve at a site is estimated using several receiver spacings. The combination of individual experimental dispersion curves from different spacings allows to obtain a single curve to be used in the inversion process.

The historical progress in electronics and computers made possible the forward step of multichannel techniques or Multichannel Analysis of Surface Waves (MASW) [37, Park et al. 1999], which uses typically 24 or more channels and can use either an active source (e.g. hammer and plate) or passive sources (e.g. ambient noise, traffic) or both. The use of multiple receivers enhances the fieldwork rate and makes the data processing faster, more objective and robust.

Most of the surface wave tests are performed using Rayleigh waves since they are easily generated and detected on the ground surface: this can be also creditable to the fact that the ground motion is predominantly vertical, contrary to Love waves, and the largest part of commercial receivers only measure the vertical component of the motion.

These techniques share the same principle: use the geometric dispersion of surface waves to infer the properties of the medium through the estimation of shear-velocity profile, passing by the vertical variation of the small-strain shear modulus.

The final step of this approach consists in the construction of vertical profiles of shear wave velocities (V_s), through the analysis of plane-wave, fundamental mode Rayleigh waves.

3.1.4 Physics

A mechanical disturbance through a homogeneous elastic medium radiates a full spectrum of P-waves, S-waves, and R-waves. In particular, when body waves directly interact with a free surface (e.g. earth surface), the elastic wave equations allow also a Rayleigh wave (R-wave) solution (for a fulfilled explanation see [45, Richart et al. 1962]). The Rayleigh wave is instead guided along the free surface of the underlying elastic medium. The particle motion (Fig. 3.4) is in a retrograde elliptical sense in a vertical plane with respect to the surface, changing to prograde elliptical with increasing depth.

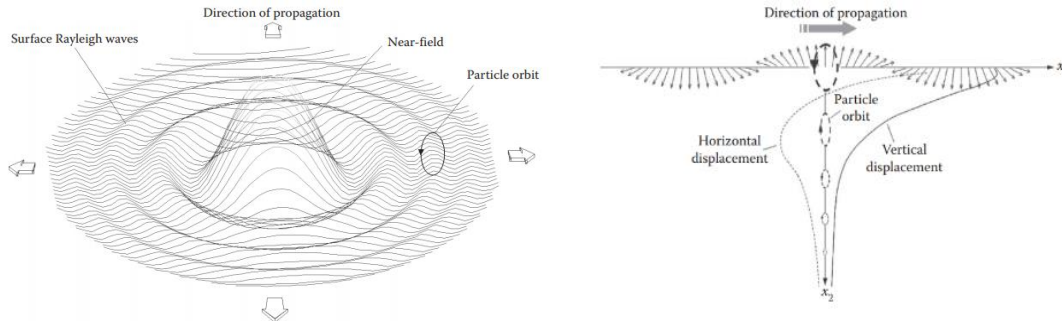


Fig. 3. 1, Left: 2D radiation pattern of Rayleigh surface waves generated by a vertical point source. Right: Elliptical polarization of particle motion in a Rayleigh wave in a homogeneous, linear elastic half-space. At the free boundary, the particle orbit is retrograde; at depth of 0.2λ it becomes prograde. From Foti, S., Lai, C. G., Rix, G. J., Strobbia C., 2012.

In order to find a solution to the equation of motion it is essential to assume a reference model that describes the soil as a stack of plane, laterally homogeneous media, bounded in a half-space with a free surface (no stress at the free surface and no stress and strain at infinity). By imposing the continuity of strain and stress at layer interface, a linear differential eigenvalues problem is obtained, with non-trivial solution only for special values of the wavenumber:

$$\frac{df(z)}{dz} = A(z) \cdot f(z) \quad (3.16)$$

The vector \mathbf{f} is formed by two displacement and two stress eigenfunctions, while \mathbf{A} is a 4x4 matrix depending on the vertical distribution of the soil properties. Among different solution techniques proposed, the propagator matrix methods are the most frequently used because of their conceptual simplicity (for exhaustive treatment see [2, Aki et al. 1980]).

In a nutshell, each layer is represented by a matrix containing its geometric and mechanical characteristics and using the continuity at the interfaces it is possible to propagate the solution across the layers. At this point, a single matrix equation representing the whole system can be assembled and, given the boundary conditions stated before and imposing a special relationship between frequency and wavenumber, a solution can be found:

$$F(k, f) = 0 \quad F_R[\lambda(z), G(z), \rho(z), k_j, f] = 0 \quad (3.17)$$

This is known as Rayleigh secular equation, where k is the wavenumber, f is the frequency, λ and G are the Lamé parameters and ρ is the mass density.

The wave packet can be decomposed by Fourier analysis into its individual frequency components, each with its own characteristic phase velocity. The shape of the phase velocity versus frequency curve is the dispersion characteristic, that will be further examined.

Therefore, for a given frequency exist a solution only for particular wavenumber values: $k=k(\omega)$.

On the other hand, in a vertical heterogeneous medium, multiple solutions typically exists and are displayed by the modal curves: for each mode, at each frequency, the four stress and displacement eigenfunctions can be computed [51, Socco et al. 2004].

During the evaluation of modes, which represents the kinematic description of the possible velocities, usually the attention goes on the first one (also known as the fundamental mode) that is considered the dominant, characterized by the lowest possible velocity. This is often not verified and sometimes higher modes can be dominant or superimposed on one another, affecting the quality of interpretation.

Each discrete possible solution shows a spike of energy concentrated exactly at a modal wavenumber and the spectrum results as in Fig. 3.5. The inverse transform of the spectrum gives a seismogram.

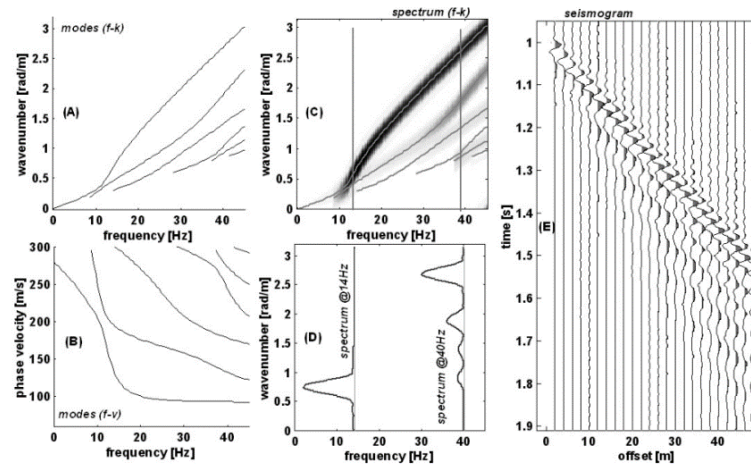


Fig. 3. 2, Modal curves in f - k (a) and f - v (b), f - k spectrum (c) with a dominant first mode, from a synthetic seismogram (e). The two sections of the spectrum (d) show the lower energy of higher modes. From Socco, L.V, Strobbia, C., 2004

The elastic energy is typically partitioned into 67% surface waves; 26% shear waves; and 7% compressional waves [32, Miller et al. 1955].

In body waves (P and S), the geometrical damping of the energy falls off as $1/r^2$, where r is the distance to the source, since the body-wave energy spreads radially outward (Fig. 3.6). The energy of R wave instead, which propagates into a cylindrical region from the source on the free surface, falls off as $1/r$. For these reasons, R wave amplitudes measured at the free surface are considerably greater also at large distances from the source [43, Rayleigh, L. 1885], explaining why surface waves often dominate seismic records.

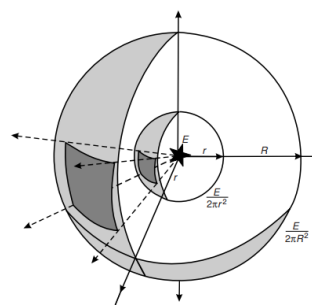


Fig. 3. 3, Spherical divergence of the energy. The progressive diminution of energy per unit area caused by spherical propagation from an energy source. From Reynolds, John M., 2011

The propagation velocity depends mainly on the shear-wave velocity V_s : in a homogeneous elastic half-space the Rayleigh-wave velocity is slightly lower than V_s ($0.87V_s < V_r < 0.96V_s$, depending on Poisson's ratio (Fig. 3.7)) and is a function of the mechanical properties of the medium, but not a function of frequency. As shear is involved, Rayleigh waves can travel only through a solid medium and, at a depth

corresponding to one wavelength, their amplitude is reduced to less than 30% of its surface value (Fig. 3.8).

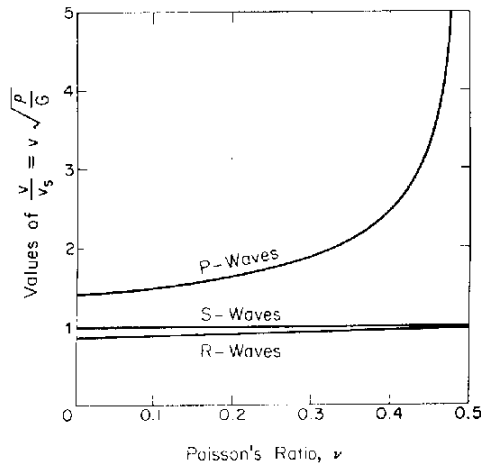


Fig. 3. 4, Relation between Poisson's ratio and velocity of propagation of compression (P), shear (S) and Rayleigh (R) waves in a linear elastic homogeneous halfspace, From Richart et al., 1962

Indeed, it is important to remark that, being the decrease with depth exponential, the particle motion amplitude becomes rapidly negligible with depth. Therefore, the wave propagation affects a confined superficial zone and consequently it is not influenced by mechanical characteristics of layers deeper than about a wavelength.

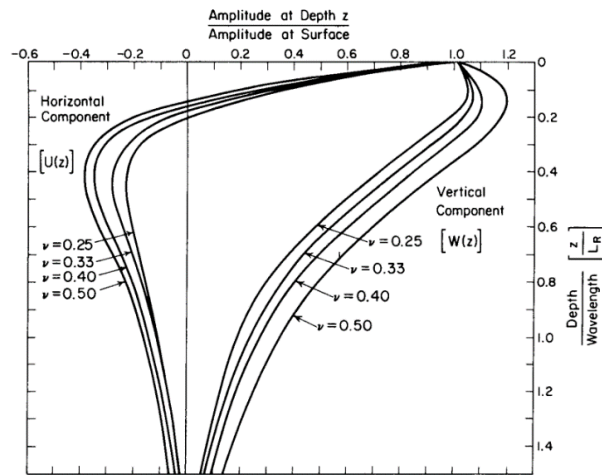


Fig. 3. 5, Amplitude ratio vs. dimensionless depth for Rayleigh wave in a homogeneous halfspace, from Richart et al., 1970

3.1.5 Geometric dispersion

The main task in surface wave testing is to extract information about the geometric dispersion of surface waves, which can be used to infer the stiffness of the medium through which it propagates.

In vertically heterogeneous media, with spatially varying elastic moduli, the phenomenon of geometric dispersion arises: different frequencies travel at different velocities (called phase velocity).

Since the depth of penetration of an R-wave scales with its wavelength, lower frequencies involve motion at large depths and their velocity is influenced by the properties of deeper layers, whereas higher frequencies are confined in thin top layers with their velocity depending on the shallow soil properties (Fig. 3.9). This means that the information about the shallow layers is carried by all the frequencies while that concerning the deep layers is carried by only a small amount of data.

As described earlier, the mechanical properties of the layers which the R-wave excites determine its velocity. Therefore, the R-wave velocity as a function of frequency, provides information about the elastic moduli of the individual layers within the system.

A broad and detailed description of dispersion can be found in [54, Telford et al.].

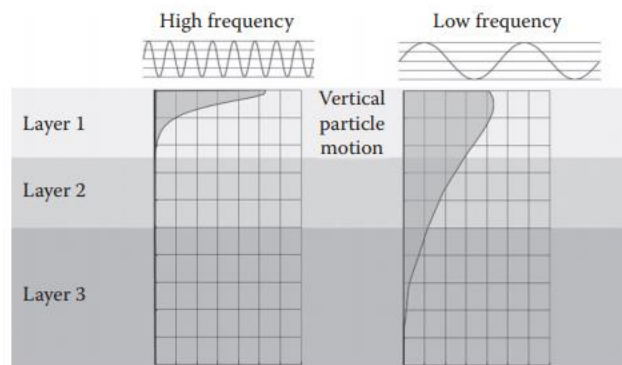


Fig. 3. 6, Geometric dispersion of Rayleigh waves: trends with depth of the vertical particle motion associated with the propagation of two harmonic waves in a layered medium. From Foti, S., Lai, C. G., Rix, G. J., Strobbia C., 2012

3.1.6 Method

The standard procedure for a multichannel surface-waves analysis can be divided in three main steps (Fig. 3.10): acquisition, processing and inversion. The method cope with surface waves in the lower frequencies (1–30 Hz) with a shallow range of investigation depth (to a few tens of meters depending on site conditions).

Surface wave data are typically collected through a traditional seismic refraction survey layout, with a set of geophones laying on the ground connected to robust and waterproof seismographs used in conjunction with field computers, allowing preliminary processing of data on-site. For the generation of surface waves, several types of sources with a sufficient energy in the frequency range of interest can be used (see paragraph 3.2.2). The frequency band interested by surface wave propagation is typically 1-30Hz, which reflects in shallow investigation depth (e.g., a few to a few tens of meters).

During data acquisition, the same source receiver configuration is moved by a certain interval to successively different locations to acquire more records: this allows to extract

information at different spatial positions, i.e. to retrieve a multi-dimensional (2D/3D) model.

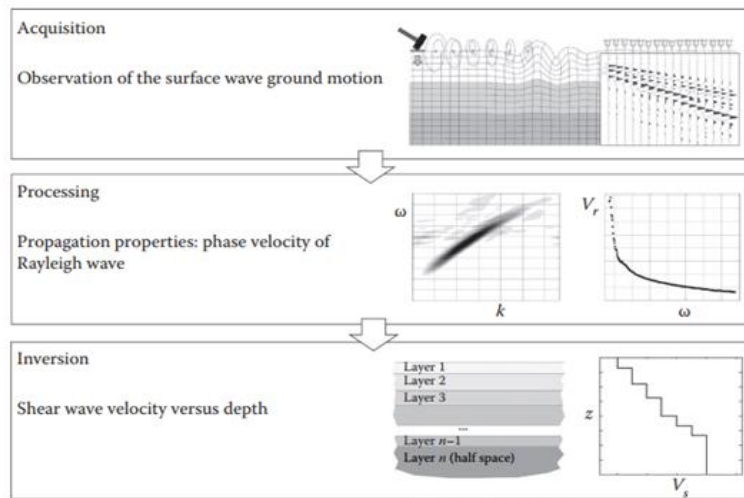


Fig. 3. 7, Flow chart of surface wave tests, from Foti, Lai, Rix, Strobbia 2012

Field data are then processed to estimate the experimental dispersion curve. A variety of signal processing techniques are applied in surface wave tests, but they mainly rely on the Fourier transform: the wave packet can be decomposed into its individual frequency components, which are subsequently processed to study the dispersion characteristic and estimate their own characteristic phase velocity.

One of the mostly used spectral domain to perform this analysis is the frequency-wavenumber (f-k): for each spread, the f-k spectrum is computed through a 2D Fourier transform and the dispersion curve is obtained by selecting the peak amplitudes for each frequency (picking).

Once apparent Rayleigh phase velocity versus frequency curves are constructed, the inverse problem is solved to obtain shear-wave depth profiles (Fig. 3.11). By collecting together all the 1D V_s profiles obtained for different seismic spreads, a 2D V_s map of the investigated area will be created.

The basis of any inversion strategy passes through the solution of a forward problem. The soil deposit is typically modeled with a one-dimensional stacking of homogeneous, linear elastic layers, and reference parameters are identified by minimizing an objective function representing the distance between the experimental and the theoretical dispersion curves. Usually this function is expressed in terms of the root mean square (RMS) of the difference between experimental and theoretical data points. In other words, the model parameters that produce a solution of the forward problem (a

theoretical dispersion curve) as close as possible to the experimental data (the experimental dispersion curve of the site) are selected as solution of the inverse problem. As a matter of fact, inverse problems are inherently ill-posed, and a unique solution does not exist. The equivalence problem is the major consequence: the same experimental dispersion curve can be explained by several shear wave velocity profiles, considering the uncertainties in the experimental data. Additional constraints and information from borehole logs or other geophysical and geotechnical tests are useful elements to mitigate the equivalence problem.

The achieved values of V_s in the shallow subsurface are useful to esteem physical properties of great interest to geotechnical and construction engineers such as stiffness, liquefaction potential, and moisture content. Besides, the shear velocity structure of the subsurface directly affect the magnitude of ground shaking in response to a nearby earthquake, thus its knowledge becomes really useful to tackle seismic hazard.

Surface wave methods are based on the solution of the inverse problem of Rayleigh wave propagation, which is aimed at estimating the shear wave velocity profile of the subsurface, widely used for soil characterization because directly related to the shear modulus of the soil skeleton.

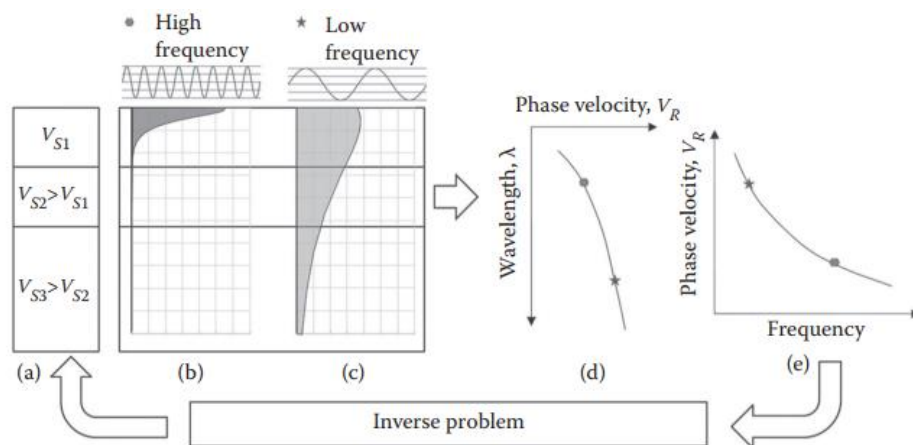


Fig. 3. 8, Parameter identification on the basis of geometric dispersion. from Foti, Lai, Rix, Strobbia 2012

3.2 Survey configuration and field measurements

Rayleigh waves are easily generated and detected at the ground surface, but an optimized acquisition requires planning, in order to obtain quality data over an adequate frequency range.

The survey design of common SW measurements is presented in this section. Basic considerations are made about the measurement mode, selection of operating frequency and time window, temporal and spatial sampling intervals.

3.2.1 Acquisition

The acquisition of seismic data is the generation and observation of the effects of the propagation of seismic waves, in time and space. The motion involves a variation of stress and strain in time within a medium, which is detected by each receiver at a specific location.

The first arrival time on ground surface of seismic waves, critically refracted at interfaces among layers having a different velocity, provide the foundations of seismic refraction methods, which suffer the intrinsic limitation related to the presence of velocity inversions or hidden layers. On the other hand, seismic reflection surveys are primarily aimed at imaging interfaces among different layers and remain mainly devoted to deep exploration, with complex processing and interpretation procedures.

In surface wave testing, the multichannel approach (MASW) is widely adopted because it enhances the possibility of mode separation and identification, attenuating errors, and does not require complex acquisition procedures. The most common survey layout identifies fundamental and higher modes of Rayleigh waves by a multiple number of receivers deployed in a linear pattern of equal receiver spacing with each receiver connected to an individual recording channel. One record consists of multiple (12, 24, 48, etc.) traces of seismic wavefields made at different distances from the source.

When logistically possible, the combination of active-source and passive data is useful for obtaining a well-constrained shear wave velocity model from the surface to large depths (Fig. 3.12). Indeed, microtremors, a wave field generated by human activities and natural events, are usually rich in low-frequency components. However, because of ambient vibration wavefield might propagate from any direction, the use of 2D arrays is mandatory.

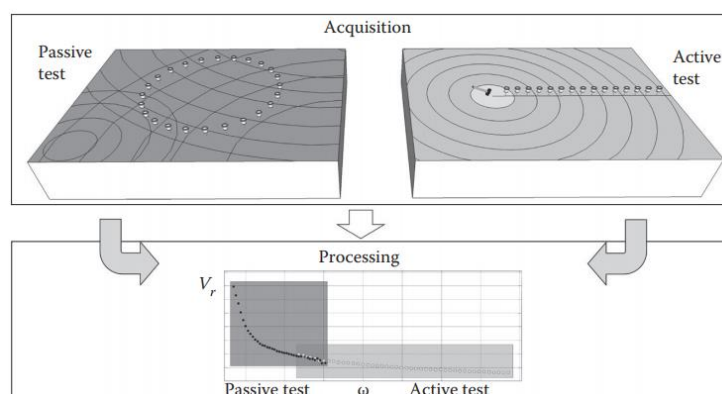


Fig. 3. 9, Combination of active and passive source surface waves measurements. From Foti, S., Lai, C. G., Rix, G. J., Strobbia C., 2012

The acquisition of seismic data requires at least a source, a set of receivers, and an acquisition system (Fig. 3.13). The equipment, measurement setup and geometry need

to be adapted to the type of survey and to the targeted wavelength range. In this section each functional element of the measurement chain will be presented, with reference to the instruments used during the field work.

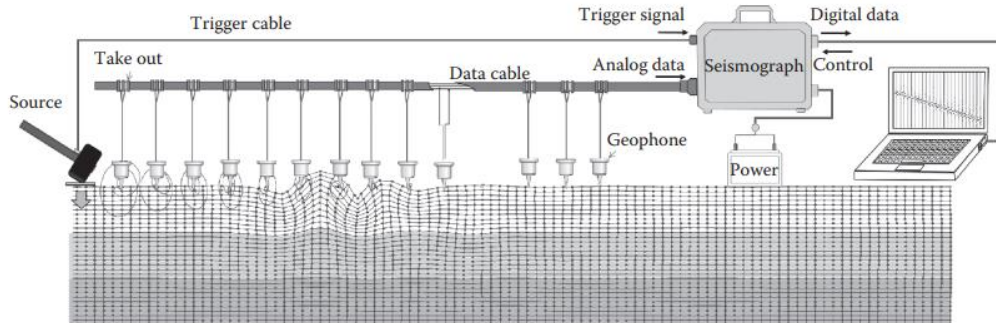


Fig. 3. 10, Schematic view of the essential field equipment: source, receivers and digital acquisition device. From Foti, S., Lai, C. G., Rix, G. J., Strobbia C., 2012

3.2.2 Equipment

The source type, alongside the material attenuation due to the site, is the responsible of the frequency content of the propagating seismic signal and the energy provided must be adequate given the target investigation depth. Generally, active sources as sledgehammers and drop weights generate energy concentrated in the frequency band from 10 to several tens of Hz. This limits the maximum resolved depth to about 15–40 m, depending on the velocity structure of the site and the mass of the impact source. Lower frequency surface waves for the investigation of deep velocity structures can be generated using very massive and onerous sources (e.g. bulldozer, vibroseis) or conversely with passive ones such as ambient vibrations, which have enough energy up to periods of tens of seconds (very low frequency).

Two main aspects have to be considered to plan an adequate source offset: near-field effects contaminate the low-frequency components of the signal at small distances, while the attenuation at large distances reduces the S/N of traces in the high-frequency band (far-field effects). As a rule of thumb, it should be adopted a source-offset equal to the desired investigation depth [37, Park et al. 1999].

Vertical geophones are typically used for the acquisition of Rayleigh wave data (Fig. 3.14). As electrodynamic velocity transducers, they are composed of a mass suspended by mechanical springs which transduce the ground motion into a measurable electric signal by relying on electromagnetic induction principles.

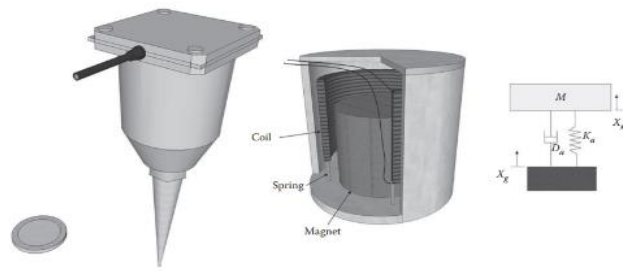


Fig. 3. 11, Schematic representation of a moving coil geophone: a coil is suspended in a magnetic field and its oscillations generate a current. From Foti, S., Lai, C. G., Rix, G. J., Strobbia C., 2012

Generally, for shallow targets, 4.5 Hz natural frequency geophones are adequate, whereas higher frequency geophones (e.g. 10–40 Hz) will be reliable for profiling to depths greater than about 10–15 m, because they will heavily attenuate the low frequencies used for surface wave measurements in shallow applications. In order to increase the survey speed, a land streamer, a platform on which geophones are attached without spikes, can be used facilitating the mobility of receiver array.



Fig. 3. 12, Geode Exploration seismographs from the University of Padova, used during the field work

Different apparatuses may be used for digitization of analog output from the geophones and recording of signals. The most common choice is the use of multichannel seismographs (Fig. 3.15), devices equipped with multiple analog-to-digital (A/D) channels, with a dynamic range determined by the number of bits available for the conversion in the corresponding hardware component. Usually, a 24-bit dynamic range seismograph, common for conventional body-wave seismic surveys in which signals are usually weak in comparison to noise, is also used for surface waves.

A 12V battery provides the power for all the acquisition period and a rugged toughbook is usually necessary to control the seismograph.

An hardware trigger cable is required to synchronize the measure with the source and multichannel seismic cables with military connectors are the linking units between geophones and seismograph.

3.2.3 Sampling and windowing

Every time we want to acquire a continuous signal, the sampling problem must be tackled.

In our case the signal, a generic physical quantity measurable over time and space, is a dataset carrying information about subsurface properties.

The data acquisition, the measurement of the wavefield at a specific location, involves an analog-to-digital conversion: the continuous signal is replaced by a discrete series of values at fixed time intervals using a transducer.

The “measurement chain” (transmission, conditioning, digitization, and recording) transforms the ground motion into a seismic trace. Thus, the seismic trace is a discrete signal and the elementary unit of seismic data: it describes the medium response to a certain source, typically sampled in terms of time in a given position in space.

This process (Fig. 3.16) implies loss of information and the fidelity of the digital data depends mainly on the density of the sampling and on the resolution of the analog-to-digital conversion, that has naturally physical limitations.

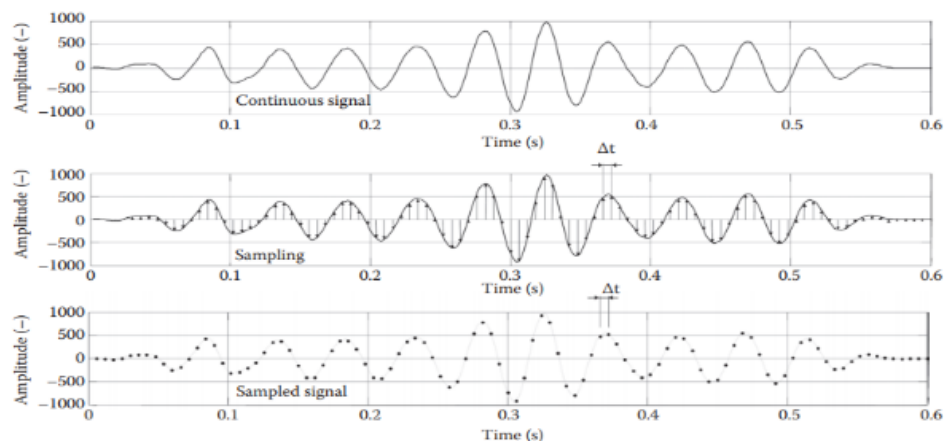


Fig. 3. 13, Sampling of a continuous signal involves reading the values of the signal at a finite discrete set of points. The sampled signal is defined only at a series of evenly spaced time instants. From Foti, S., Lai, C. G., Rix, G. J., Strobbia C., 2012

The time interval between points in a recorded waveform is named temporal sampling interval Δt and its reciprocal is the sampling frequency F_s . The sufficient condition to capture all the information from a continuous-time signal of finite bandwidth is

established by the Nyquist–Shannon theorem: the sampling frequency should be at least twice as high as the highest frequency f_{max} of the record.

From an acquisition planning perspective, given a maximum frequency in the signal f_{max} , it is possible to evaluate the sampling frequency needed to sample without loss of information as

$$F_S = \frac{1}{\Delta t_S} > 2 \cdot f_{max} \quad (3.18)$$

The Nyquist frequency F_{Nyq} is the maximum observable frequency in sampled data and it is equal to half the sampling frequency F_S .

$$F_{Nyq} = \frac{1}{2\Delta t} \quad (3.19)$$

If the chosen temporal sampling interval is too big, we bump into the subsampling problem: the maximum frequency exceeds the limit of F_{Nyq} , an overlapping of some frequencies takes place and the original signal cannot be recovered. Any frequency component above F_{Nyq} is represented as a fictitious component at a lower frequency. This distortion is known as aliasing (Fig. 3.17).

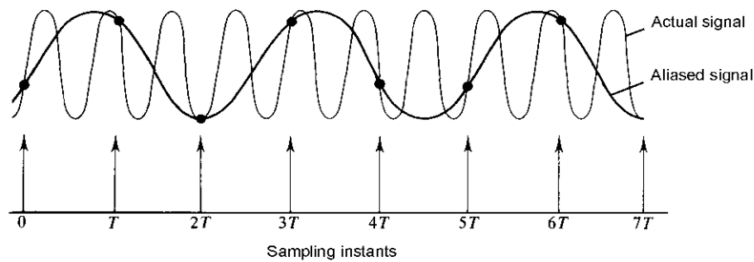


Fig. 3. 14, An example of aliasing in the time domain. From Ifeachor, E.C., Jervis, B.W., 1993

However, the sampling of the signal in space is even more crucial in seismic acquisition and it is performed by the horizontal distance between discrete measurements. As shown earl, we adopt the same reasoning for the spatial frequency (wavenumber):

$$K_{Nyq} = \frac{1}{2\Delta x} \quad (3.20)$$

Therefore, to avoid spatial aliasing we need to adopt a geophone spacing in accordance with:

$$\Delta x < \frac{1}{2 \cdot k_{max}} \quad (3.21)$$

The effect of the wave propagation is indeed detected by a limited number of receivers and is recorded on a discrete, finite set of points, in time and space.

The duration of the wave train can be large, exceeding some seconds at less than 100 m in distance and their high energy allows them to be dominant in active seismic records.

The time window determines how long the system will record signals from the receivers after the wave train has left the source position. The beginning and end of the acquisition are planned to record the whole surface wave train. Usually 2 s is sufficient for most arrays, but when testing on soft sediments (associated with low seismic velocity) it is suggested to use longer windows [20, Foti et al. 2018].

3.2.4 Measuring protocol

The acquisition was performed in the eastern part of the landfill area, the same investigated with geoelectrical and electromagnetic surveys. The MASW method was exploited to evaluate the mechanical properties of the field that hosts the landfill, through the study of Vs distribution with depth. In detail, we focused on the detection of the landfill's baseline, knowing a priori its shallow estimated depth from geotechnical information [8, Brandstätter et al. 2013].

Most of the acquisition parameters depend on the target depth and the desired resolution, thus, a careful design of the experiment was of primary importance for obtaining an optimal result.

Field measurements were done on three separate days along three different profiles, but mostly maintaining the same acquisition geometry (Fig. 3.18). In every case, we decided to energize from both the edges of the array, thus allowing normal and reverse shots analysis, also because of the assumed heterogeneity of the area.

Dealing with time sampling, we opted for 1kHz of sampling frequency (1ms) and for 2s length of the records (time window), allowing an enough margin for the specific case.

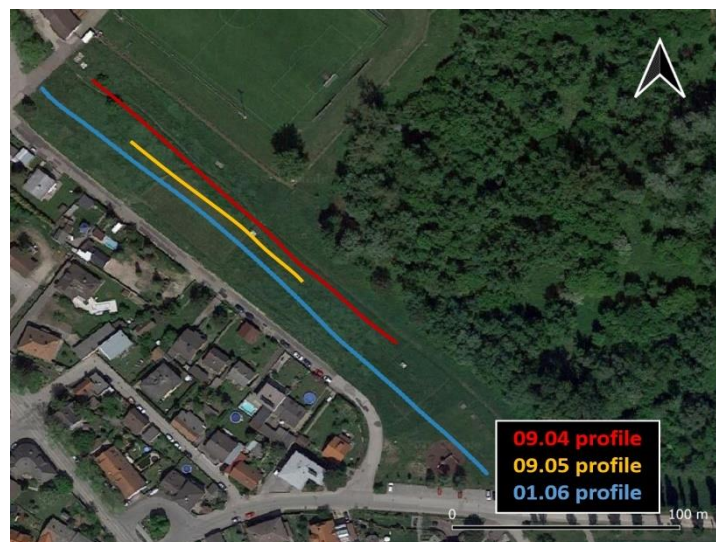


Fig. 3. 15, Schematic representation of the SW acquisitions

A first profile was acquired on April 9th with 24 channels occupied by 4.5Hz geophones and the others 24 from a land streamer. This initial measurement had the purpose to

preventively check the data quality and verify the accuracy of the settled parameters. As will be shown ahead, the S/N ratio of the streamer data was significantly lower, likely due to the poor contact of the receivers with the ground caused by the tall grass coverage of the field.



Fig. 3. 16, Geophones on land streamer, adopted for the first acquisition

The second acquisition took place on May 9th, composed by normal and reverse shots collected along one single profile whose 48 channels were all set up by 4.5Hz geophones. However, during this field day the dataset captured (on the yellow profile in Fig. 3.18) was noisy and unclean because of heavy rain that surprised us, so it had been discarded after the initial processing.

The third and definitive acquisition of June 1st was planned to properly cover the areas of interest underlined by the information in our hands gained by ERT and IP previously adopted. The data were collected on 3 consecutive linear sections (i.e. P1, P2, P3), oriented parallel to the main field length. P2 and P3 were partially overlapped and, even if the entire profile length was of approximately 250m, the subsurface covered by the survey is composed by three portions (about 50m length) in correspondence with the center of each section (Fig. 3.20).

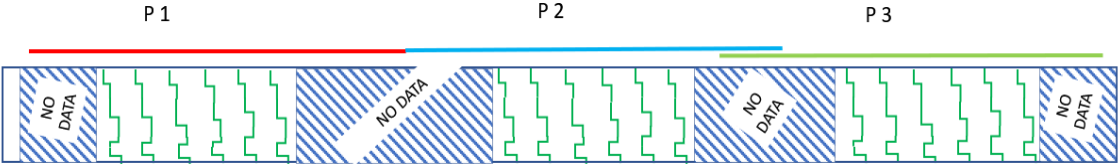


Fig. 3. 17, Schematic representation of the last acquisition with the subsurface portion covered. From Barone I.

For each of these last sections, we used multi-channel seismic cables connecting 48 geophones of 4.5Hz, with a relative spacing of 2 m. The number and the position of the receivers define the total size of each array, that in our case was of 94 m. We opted for

an initial source offset of -4m, followed by shots every 8 meters, ending 6m far away from the last geophone of each array (Fig. 3.21).

The data were acquired using two 24-channel seismographs Geode by Geonics, connected together with a multi-core cable, making possible to manage contemporary 48 channels during each single measurement. The measuring device was always placed at the center of each profile, between geophone 24 and 25.

Two external 12V car batteries, connected to the Geodes, were used to generate the current for the survey and a Panasonic toughbook allowed to manage, visualize and monitor the acquisition.

As in most shallow surveys, two different sledgehammers striking on a metal plate were used as seismic source: a small 5 kg one and a bigger of about 8 kg. The maximum offset, distance from the first geophone of the array, was always fixed at 4 m.

Redundancy in measurements allowed to suppress the noise and to further increase the signal-to-noise ratio: as with any active seismic survey, the SN ratio can be improved by stacking (summing together) the records from several shots acquired in the same position. In this case, we stacked 3 traces for each measurement.

A piezoelectric trigger system was adopted to synchronize the measure with the shot.

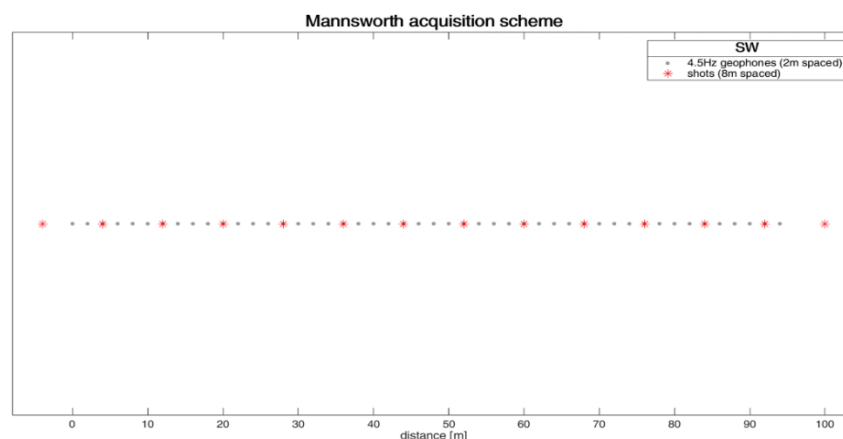


Fig. 3. 18, Acquisition scheme of each single section of the last profile

3.3 Processing and Inversion

The acquired seismograms need to be properly analyzed and elaborated to derive the correct information about wave propagation, estimating uncertainties and errors that affect the gathered data, before to turn them into the corresponding velocity profiles.

Processing and inversion should enable the interpretation of the apparent dispersion characteristics, evaluating the local quality of the data, filtering coherent noise due to other seismic events and determining energy distribution, higher modes and attenuation.

3.3.1 Data analysis and dispersion curves

Several signal analysis tools can be used for the extraction of dispersion curves from experimental data. We adopted the broadly used frequency–wavenumber (f – k) method: data collected in the time–offset domain (seismograms) are transformed by applying a 2D Fourier transform over time and distance to frequency domain, where the peaks of the amplitude spectrum are found in correspondence of pairs of wave propagation parameters.

Multichannel records were analyzed, processed and visualized with Matlab, especially through some powerful scripts kindly granted by the PhD. student Ilaria Barone.

With the aim of comparing all the collected information during the three different campaigns, we decided to compute every f – k plot from each seismogram. As standard correction, the first two geophones proximal to the source were discarded because assumed to be in the near field.

Only for visualization purposes, we normalized the individual geophone signals in the time–space domain, enabling an estimation of the decay amplitude with distance from the source (Fig. 3.22). Anyway, this appeared informative on seismic waves propagation and it will be considered and explored in the framework of conclusions.

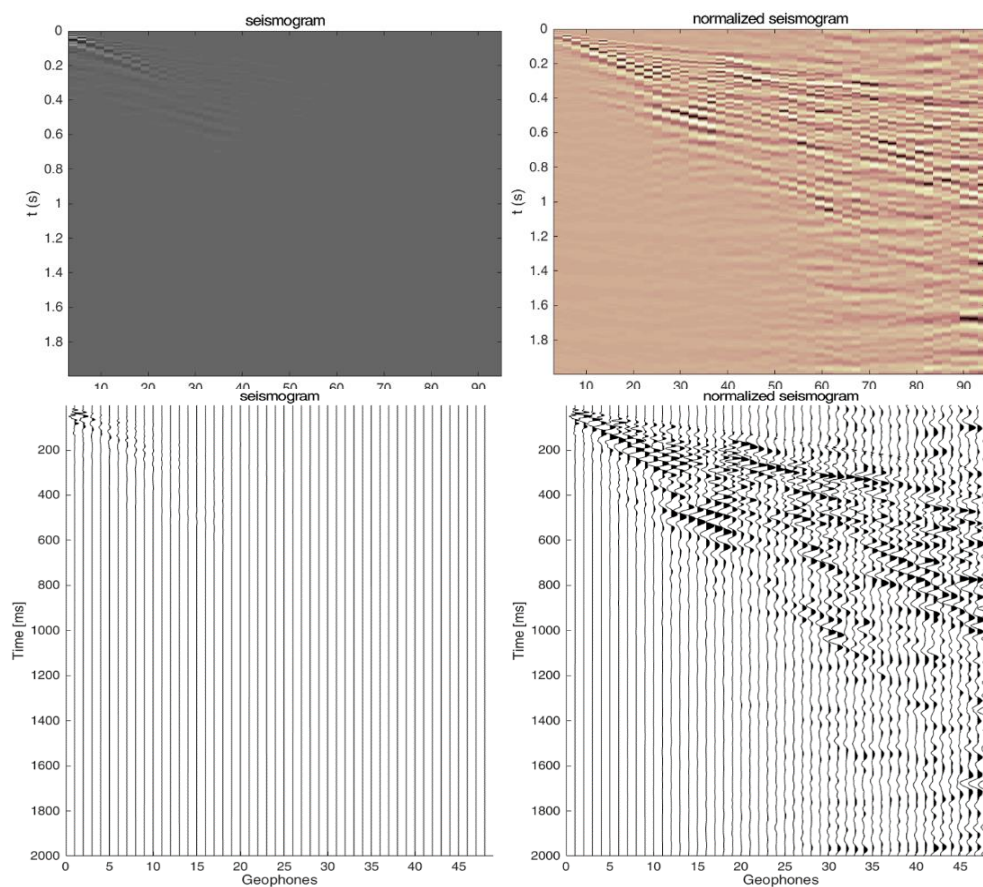


Fig. 3. 19, Acquired and normalized seismograms for the shot #1001: standard and wiggle plots

Each shot gather was transformed in a f-k spectrum. Fig. 3.23 shows an example of amplitude of the f-k spectrum for a set of experimental data. Here, fundamental and higher modes are identified and separated: the approach used for the mode selection relies on the visual inspection of the spectrum.

At a given frequency, the fundamental mode was fairly assumed to be associated to the amplitude maximum.

After the first examination, we decided to focus and work primarily on the dataset gained during the last acquisition: the cleaner traces and the wider number of shots allowed us to obtain a 2D model on the very line of electric and electromagnetic surveys.

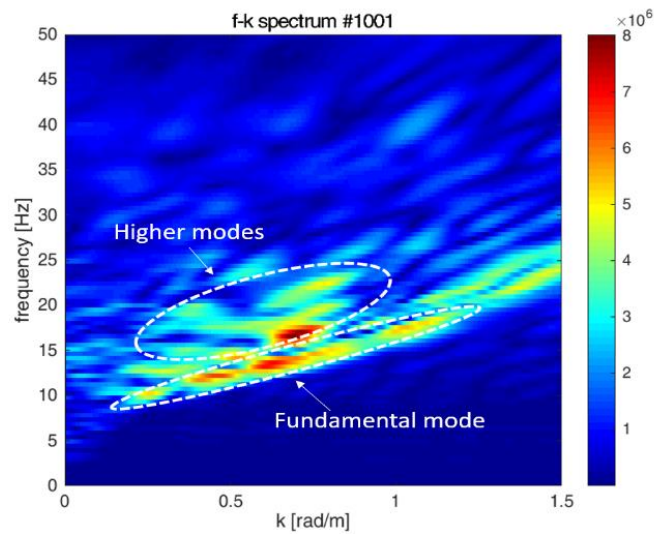


Fig. 3. 20, Fundamental and higher modes in the f-k spectrum

The first two acquisitions, on the contrary, produced fewer and much noisy seismograms, also because of logistic difficulties. This would have affected the picking accuracy, thereby preventing a robustly defined trend for the inversion.

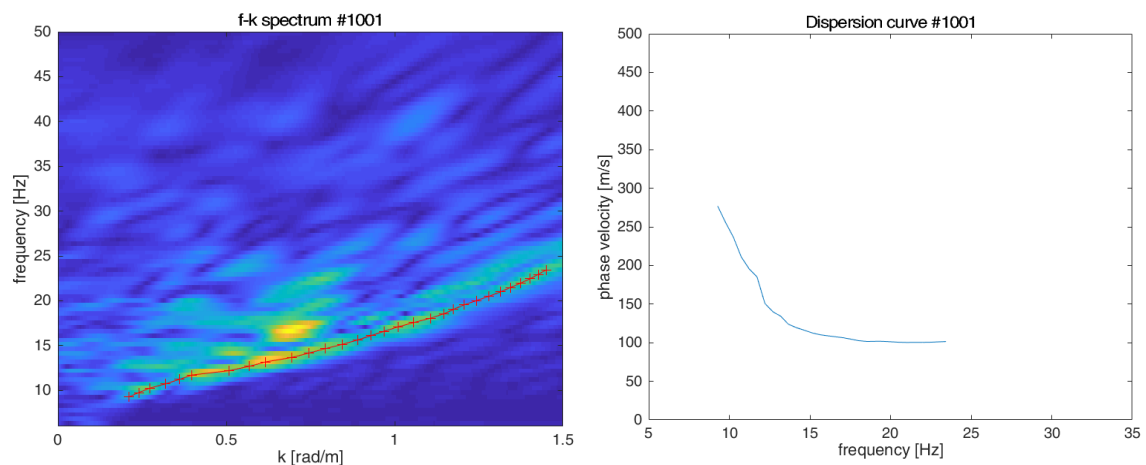


Fig. 3. 21, Picking of the maxima into the f-k spectrum and the relative dispersion curve

Picking of maxima allowed the identification of the frequency-wavenumber couples associated to the propagation of the fundamental Rayleigh mode. The procedure was manually performed, searching for a compromise between accuracy, smoothness and continuity in the selection of the main branch of the fundamental mode.

The experimental dispersion curves were then obtained by the relationship that describes the phase velocity of the surface wave V_{ph} [m/s] at frequency f [Hz] and corresponding wavenumber k :

$$V_{ph} = 2\pi/k \quad (3.22)$$

This operation is showed in Fig. 3.24.

In order to assess the lateral variations of the site, dispersion curves retrieved from forward and reverse shots were compared. In addition, we analyzed independently different subgroups of seismic traces (1:24, 25:48) from the dataset, to inquire into heterogeneities of shallow layers and keep the cleaner traces only (Fig. 3.25). Thus, we opted for a selection of the first 24 geophones response of the various shots collected along each line, considering both normal and reverse directions, in order to gain better results.

As seen in the majority of cases, f - k spectra and the related dispersion curves are less defined in the lower frequencies: this is an inherent consequence of the energy generated by the adopted seismic source and of the low-cut filtering effect of the shallow layers.

All the f - V_{ph} values obtained from this process, attributed to the central point of the 24 selected receivers, were then saved as single files and used as input parameters for the inversion.

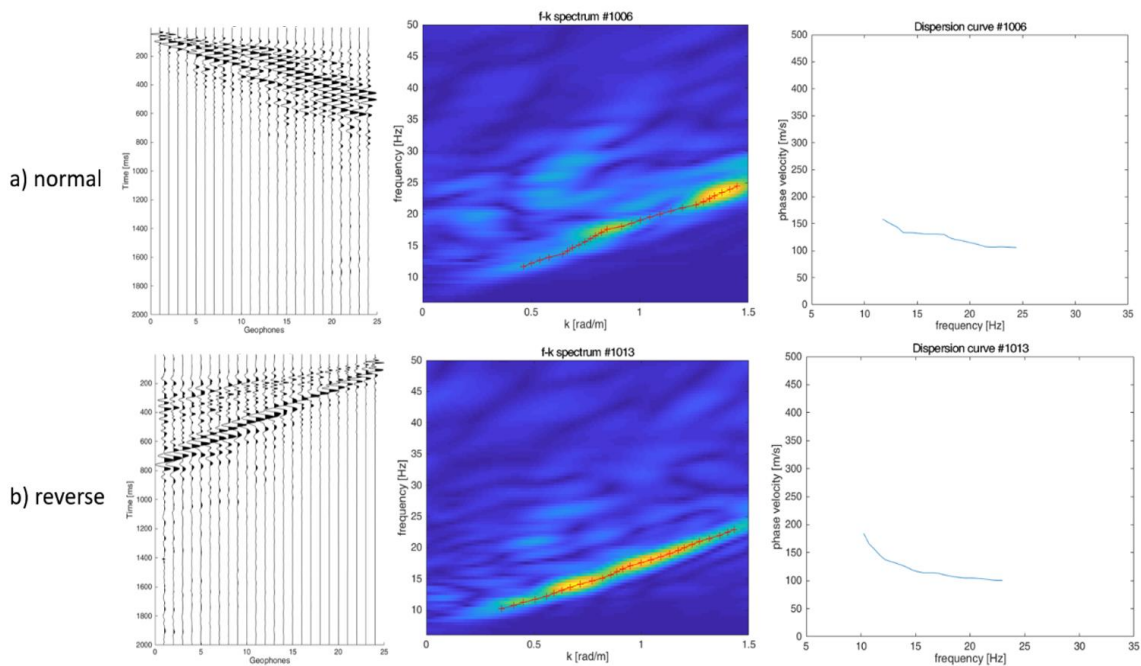


Fig. 3. 22, Comparison between normal and reverse shots from a selection of the first 24 geophones, related to the same position in depth and belonging to the first section of the 01.06 profile

3.3.2 Modeling and data inversion

Each dispersion curve was individually inverted into a 1D Vs-depth trace (Fig. 3.26).

The inversion process is aimed at searching the best subsurface velocity model whose forward response best fits the experimental data. It is based on a proper definition of the misfit function, typically a norm of the distance between the experimental and the theoretical dispersion curves, that is iteratively minimized until an acceptance error value.

However, as it is broadly known, the inverse problem is non-linear, mathematically ill-posed and it is affected by solution non-uniqueness. Indeed, several models provide an equally good fit to the experimental data, therefore appropriate a-priori assumptions on some inversion parameters (i.e., thickness, number of layers, mass densities, boundary depth, etc.) allow to constrain the result.

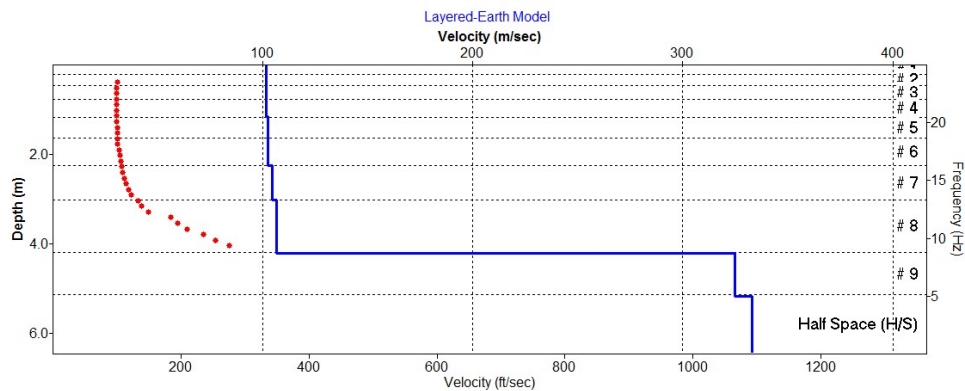


Fig. 3. 23, Inversion output of ParkSEIS. The red points denote the input values from the dispersion curve and the blue line is the Vs-depth profile obtained

The inversion was performed with the software ParkSEIS[®] 2.0, whose searching algorithm is based on the sensitivity matrix (called a "Jacobian" matrix) that depicts the relative change in phase velocity of the theoretical dispersion curve for a unit change in velocity of a particular layer in the model [41]. A significant number of empirical parameters describing the ground model, introduced in the algorithm, are necessary to make the searching process more accurate, stable, and faster (i.e. the overall frequency range [Hz] and S/N of the input dispersion curves, the number of iterations and the min. match (%) for the searching process, the number of layers and the max. depth for the model).

According to information and experience, the software requires to adjust a series of input settings that influence the reliability of the inversion result. Decision was made to test a model with 10 homogeneous layers, automatically thicker with depth, with a maximum depth of 10 m, suited for the expected resolution of the acquisitions. A constant Poisson's ratio was settled at 0.4, without specifying a density value for the layers.

The iterations were fixed at 3 and no boundary limit nor weighting factor were applied.

At the end of the process, the program displayed both measured and modeled dispersion curves to indicate how closely they match for the solution found by the program. The average final match for all the inversions performed exceed the 92%, mainly heading in the range of 95-99% (Fig. 3.27).

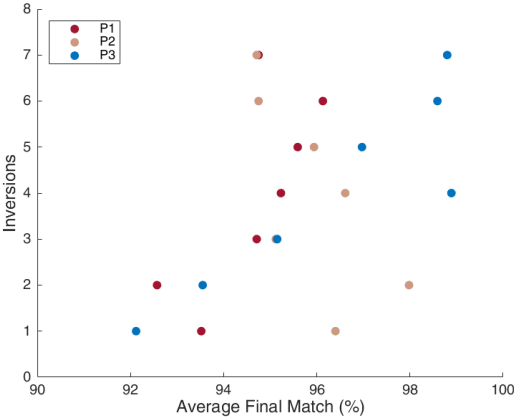


Fig. 3. 24, Overall inversion matches

Gathering all V_s -depth traces into shot station sequential order, it results in a pseudo-2D image of the shear-wave velocity field. This process was performed by linear interpolation for each of the three sections of the last acquisition, and the tomographic images generated were then located on their exact profile's position (Fig. 3.28).

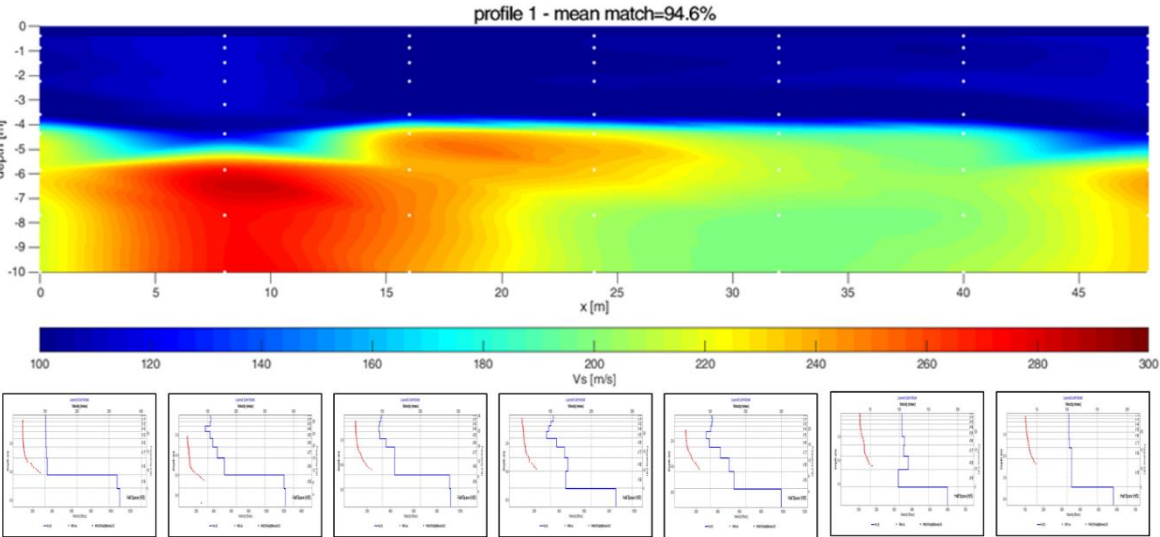


Fig. 3. 25, 2D Vs tomography obtained by linear interpolation of the gathered inversions (boxes below) constituting the first profile P1

4 Geoelectrical Methods

4.1 Electrical Resistivity Method

Electrical resistivity tomography (ERT) is a well-established geophysical method that provides insights regarding an investigated domain based on its electrical properties. The method is based on four electrode array (i.e., quadrupole), where two (potential) electrodes are used to measure the voltage and other two electrodes are used to impose to the ground an electric field.

ERT has been successfully applied for imaging subsurface structures, to characterize groundwater, faults, contaminant plumes and several environmental issues.

Usually known as Hydrogeophysics given its strong dependence on water content variations as well as on water chemistry, ERT investigates the spatial distribution of electrical resistivity of the ground involved.

The aim of this chapter is to provide a brief description of this methodology with the definition of some fundamental concepts.

4.1.1 Theoretical background

ERT, as a direct current (DC) electric method, is based upon Ohm's law

$$\Delta V = RI \quad (4.1)$$

where ΔV is the electric potential difference [V], I is the injected current [A], and R is the resistance [Ω] given by the soil to the current flow. This last parameter is related not only to electrical features but also to material and geometric properties. In fact, if we consider a current flow through a cylindrical conductor with length L [m] and area A [m²], for the second Ohm's law we have:

$$\rho = \frac{R \times A}{L} \quad (4.2)$$

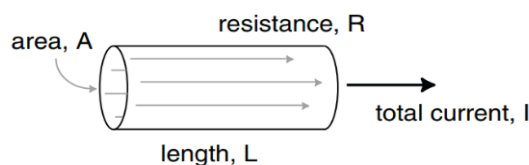


Fig. 4. 1, Definition of resistivity, from Everett, Mark E. 2013.

where ρ is the electrical resistivity [Ωm]. Electrical resistivity can also be defined as $1/\sigma$, where σ is the electrical conductivity [S/m] of the material, a measure of the ability of a material to sustain long-term electric current flow (Fig. 4.1).

4.1.2 Electrical properties of rocks

The distribution in the subsurface of the current density, a vector determining the direction and magnitude of the current flowing through a unit cross-section, depends on the electrical properties (i.e., ρ or σ) of the medium.

Resistivity ρ is a property of the considered material (Fig. 4.2) and, therefore, it does not depend on current intensity or electrode array geometry. In fact, it is particularly suitable for measuring variations in minerals and fluids content, porosity, saturation and ionic concentration of the pore water.

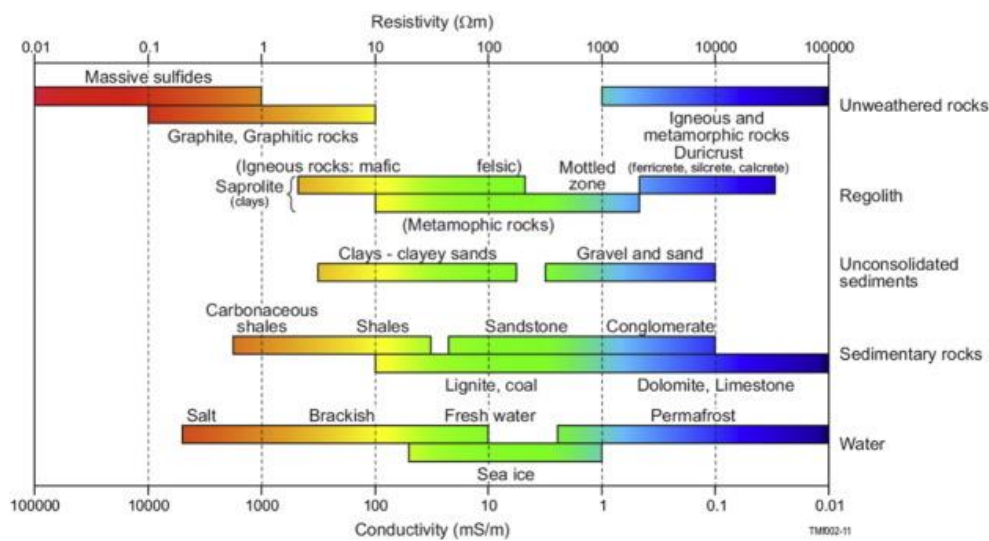


Fig. 4. 2, Conductivity-resistivity values of various geological materials. Modified after Palacky, G., 1987

Electrical conduction in most geological media is electrolytic, with ions in the pore fluids being the predominant charge carriers. The matrix conduction has usually very low values ($10^{-14} - 10^{-10}$ S/m), and if metallic grains and clay minerals, responsible of polarization phenomena, are absent, it can be negligible (Fig. 4.3).

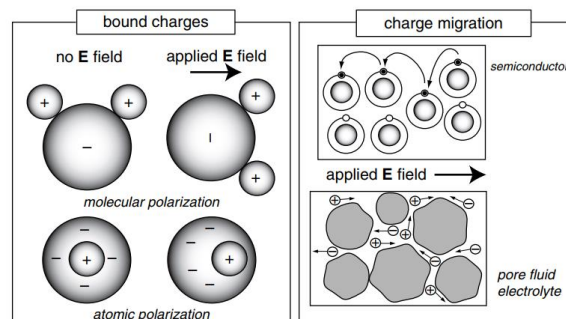


Fig. 4. 3, Electrical polarization and migration mechanisms. From Everett, Mark E. 2013

Increasing of salinity, porosity ϕ , and temperature T trigger a rising in electrolytic process and directly affect the bulk electrical conductivity. Interconnected and saturated pores represent pathways for electrical conduction, owing to the presence of dissolved ions in the pore-fluid solution.

A petrophysical model that describes the relationship between these parameters, developed for clean and unfractured sandstones, is the traditional Archie's law [Archie, 1942]

$$\rho = F\rho_w = \frac{a}{\phi^m S^n} \rho_w \quad (4.3)$$

where ρ and ρ_w are respectively the bulk resistivities of the medium and the fluid; ϕ the porosity; a , m and n empirical constants ($m =$ cementation exponent $1.3 < m < 2.4$, $0.5 < a < 1$ generally $\cong 1$, $n \cong 2$), F the formation factor linked to porosity and pore tortuosity, always > 1 ; S the water saturation $V_{\text{water}}/V_{\text{pores}}$ ($0 \leq S \leq 1$).

4.1.3 Physics

Combining equations (4.1) and (4.2) in an infinitesimal way, we have

$$\Delta I = \frac{\Delta S}{\Delta L} \cdot \frac{-\Delta V}{\rho} \rightarrow \frac{\Delta I}{\Delta S} = \frac{-\Delta V}{\Delta L} \frac{1}{\rho} \rightarrow \mathbf{J} = \frac{\mathbf{E}}{\rho} \quad (4.4)$$

where \mathbf{E} is the electric field intensity vector [V/m] and \mathbf{J} is the current intensity vector [A/m²]. Using electrical conductivity, we can write the most common

$$\mathbf{J} = \sigma \mathbf{E} \quad (4.5)$$

Since electrostatic field are conservatives, electric field can be expressed as the gradient of the scalar field of potential V

$$\mathbf{E} = -\nabla V \quad (4.6)$$

and replacing this into the equation (4.5), we get the Ohm's law (4.1) in differential way.

$$\mathbf{J} = -\sigma \nabla V \quad (4.7)$$

As stated before, a fundamental principle for the DC electrical methods is the charge conservation, expression of stationarity of electrical flow. Generally, this principle is written in differential way

$$\text{div} \mathbf{J} = \nabla \cdot \mathbf{J} = 0 \quad (4.8)$$

where $\nabla = \partial/\partial x, \partial/\partial y, \partial/\partial z$ is the Nabla operator, which indicates the divergence of the vector.

Replacing equation (4.7) in (4.8) we get the potential distribution in stationary conditions:

$$\nabla \cdot (-\sigma \nabla V) = 0 \quad (4.9)$$

$$\frac{\partial}{\partial x} \left(\sigma_x(x, y, z) \frac{\partial V}{\partial x} \right) + \frac{\partial}{\partial y} \left(\sigma_y(x, y, z) \frac{\partial V}{\partial y} \right) + \frac{\partial}{\partial z} \left(\sigma_z(x, y, z) \frac{\partial V}{\partial z} \right) = 0$$

This latter full form expression shows the possible heterogeneity and anisotropy of σ .

Given a homogeneous system, the partial derivatives of σ cancel each other

$$\sigma_x \left(\frac{\partial^2 V}{\partial x^2} \right) + \sigma_y \left(\frac{\partial^2 V}{\partial y^2} \right) + \sigma_z \left(\frac{\partial^2 V}{\partial z^2} \right) = 0 \quad (4.10)$$

and assuming it even isotropic ($\sigma = \sigma_x = \sigma_y = \sigma_z$), we can write

$$\sigma \left(\frac{\partial^2 V}{\partial x^2} + \frac{\partial^2 V}{\partial y^2} + \frac{\partial^2 V}{\partial z^2} \right) = 0 \quad (4.11)$$

that is equivalent to the Laplace's equation

$$\nabla^2 V = 0 \quad (4.12)$$

Laplace's equation generally represents the diffusion by potential gradient through a homogeneous and isotropic medium.

4.1.4 Single electrode

Due to our interest, it is useful to rewrite Laplace's equation in spherical coordinates:

$$\left(\frac{\partial^2 V}{\partial r^2} + \frac{2}{r} \frac{\partial V}{\partial r} \right) = 0 \quad (4.13)$$

In this way, it is easier to undertake a single electrode case, placed in the origin of the coordinates system ($r=0$) where the current I is injected in a homogeneous space of resistivity ρ .

The generic solution can be obtained:

$$\begin{aligned} \frac{\partial}{\partial r} \left(r^2 \frac{\partial V}{\partial r} \right) &= 0 & (4.14) \\ \rightarrow \left(r^2 \frac{\partial V}{\partial r} \right) &= \text{cost} = C_1 \\ \rightarrow V &= C_2 - \frac{C_1}{r} \end{aligned}$$

where C_1 and C_2 are the constants determined by boundary conditions. It is common to impose the condition $V=0$ when the distance r stretches to infinite; meanwhile, due to spherical symmetry and centered on the electrode in the origin, we can define current J as function of r :

$$V(r \rightarrow \infty) = 0 \rightarrow C_2 = 0 \quad (4.15)$$

$$I = 4\pi r^2 J \rightarrow I = -4\pi r^2 \sigma \frac{\partial V}{\partial r} \rightarrow I = -4\pi r^2 \sigma \frac{C_1}{r^2} \rightarrow C_1 = -\frac{I\rho}{4\pi}$$

from which

$$V(r) = \frac{I\rho}{4\pi r} \quad (4.16)$$

Therefore, it is possible to transcribe this result in the event that the electrode is placed upon the surface of a homogeneous half space (Fig. 4.4). In this more physically realistic case, the current I is distributed upon only half of the previous volume and the current density J is double:

$$V(r) = \frac{I\rho}{2\pi r} \quad (4.17)$$

$$J = \sigma E = -\frac{1}{\rho} \frac{dV}{dr} = \frac{I}{2\pi r^2} \quad (4.18)$$

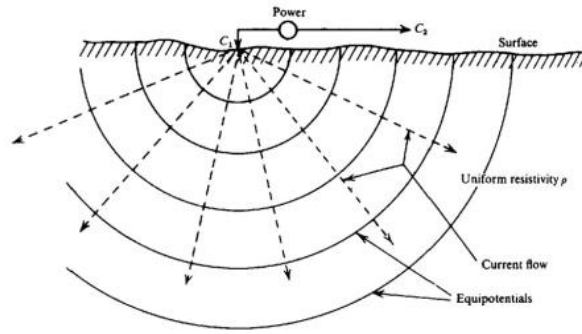


Fig. 4. 4, Electric field for a point charge in a half-space. From Telford, W.M., Geldart, L.P., Sheriff, R.E., 2010

4.1.5 Multiple electrodes

In ERT, a couple of electrodes is adopted for the current injection (C1, C2) and another couple for measuring the potential difference (P1, P2). Considering the electrodes placed at the surface of a homogeneous half-space (Fig. 4.5), then the current flows radially through a hemisphere of radius r and surface area $2\pi r^2$.

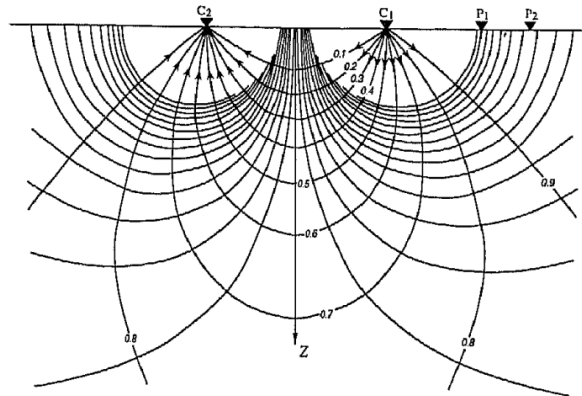


Fig. 4. 5, Current (C) and potential (P) electrodes placed on the surface of a homogeneous half-space and distribution of the current and potential lines. From Ward, S. H., 1988

Measurements could be performed with hundreds of electrodes to gain information about spatial changes in the electrical properties of the subsurface.

The difference of potential can be easily written by the effect overlapping

$$V_{p1} = \frac{I\rho}{2\pi r_1} + \frac{-I\rho}{2\pi r_2} \quad V_{p2} = \frac{I\rho}{2\pi r_3} + \frac{-I\rho}{2\pi r_4} \quad (4.19)$$

from which we obtain the measured one

$$\Delta V = \frac{I\rho}{2\pi} + \left[\left(\frac{1}{r_1} - \frac{1}{r_3} \right) - \left(\frac{1}{r_2} - \frac{1}{r_4} \right) \right] \quad (4.20)$$

The use of 4 electrodes is required to separate the contribute of the resistance given by the medium and the contact resistance, generated by different electrical properties of

electrodes and ground: the first are electronic conductors while the second is ionic conductor (Fig. 4.6). If only 2 electrodes were used for measuring current and potential, could not be possible to separate the two contributes and remove the contact resistance, function of the intensity of current that flows.

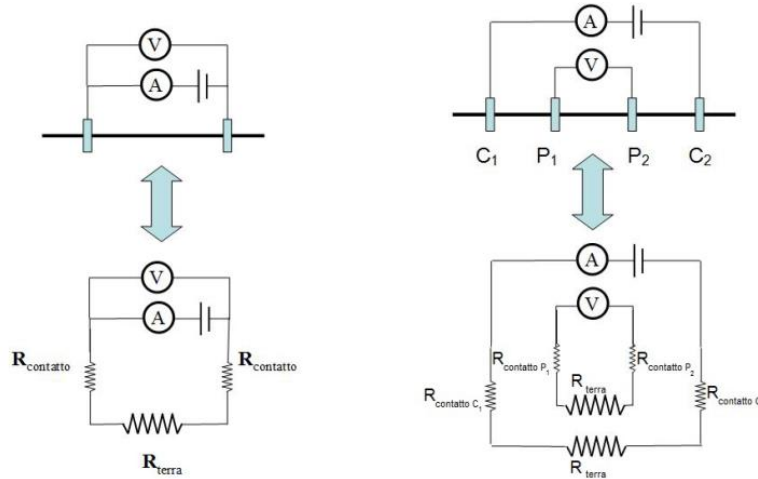


Fig. 4. 6, DC-resistivity dipole - on the left - and quadrupole - on the right -. From Cassiani, G. lectures

Until now, we assumed the perfect homogeneity of the medium in which is generated the electric field. However, a geological section may show heterogeneities and series of lithologically defined interfaces which deflect by diffraction the current lines: they will arrange following the minimum resistance paths, according to Fermat's principle. If we consider a two-layer domain (as schematized in Fig. 4.7), we can see how the current-flux lines are modified according to both vertical and lateral variations in subsurface resistivity.

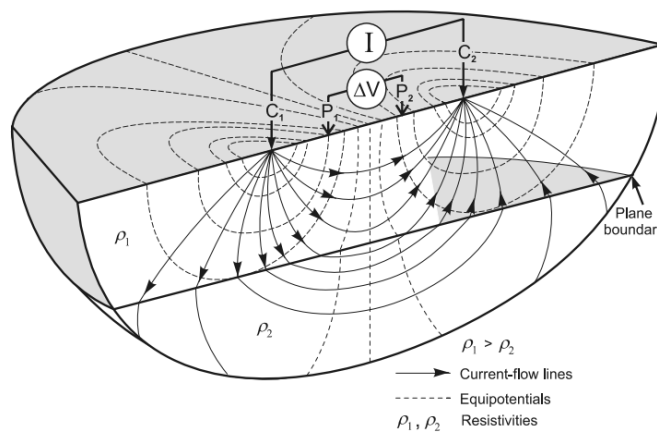


Fig. 4. 7, Principle of resistivity measurement with a four-electrodes array in a nonhomogeneous system. From Knödel, K., Lange, G., Voigt, H.J., 2007

The heterogeneity in resistivity distribution inside the Earth allow us to re-arrange equation (4.16) to solve for an apparent resistivity ρ_a , which is interpreted to be the resistivity that would have been measured if we were considering a homogeneous, flat earth domain.

$$\rho_a = \frac{k \Delta V}{I} \quad (4.21)$$

The real resistivity values are determined through the inversion process that will be described later. Consider that ρ_a can be written as a product of the measured Earth impedance $Z = \Delta V/I$ and a geometric factor K that depends only on the chosen electrodes array.

$$k = 2\pi \left[\left(\frac{1}{r_1} - \frac{1}{r_3} \right) - \left(\frac{1}{r_2} - \frac{1}{r_4} \right) \right]^{-1} \quad (4.22)$$

4.1.6 Electrode arrays

An electrode array is a geometric configuration describing the relative position of current and potential electrodes in a quadrupole [7, Binley & Kemna 2005].

Several configurations are available, and each should be chosen according to the objective of the study, the depth of investigation, site access, and instrument limitations. The most commonly used electrode arrays in resistivity surveys are represented in Fig. 4.8.

Distinctive characteristics are the intensity of the signal, essential for signal to noise (S/N) ratio and the lateral and vertical resolution. They both are strictly related to the electrode spacing set by the array: as bigger is the electrode distance as deeper the current lines penetrate, at the expense of a minor resolution. Thus, when the length is short, the current paths investigate only the upper part of the subsurface domain and therefore may not explore the lower layer.

As a rule of thumb the investigation depth is set at 1/5 of the length of the array, but it also strongly influenced by the cable length, by the power supply and by the electrical characteristics of the investigated domain.

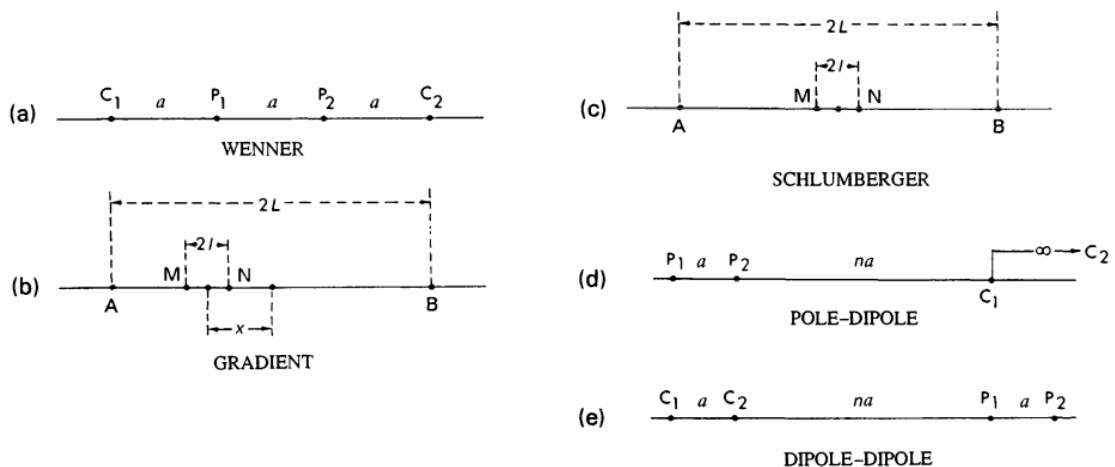


Fig. 4. 8, Example of most popular electrode configurations in resistivity and induced polarization surveys. C and P indicate respectively current and potential electrodes. It is also common for the gradient and Schlumberger arrays to use A,B for the current and C,D for the potential electrodes. Modified after Sharma, P.V., 1997

As shown in Fig. 4.9, the resolution is quite concentrated at the injection point: 50% of the current flows upon a depth about half of electrode spacing and quickly decrease with their distance. This fact is due to the diffusive nature of the equations that describe the current transmission. Consequently, electrode spacing rules the resolution, that results higher in proximity of the electrodes.

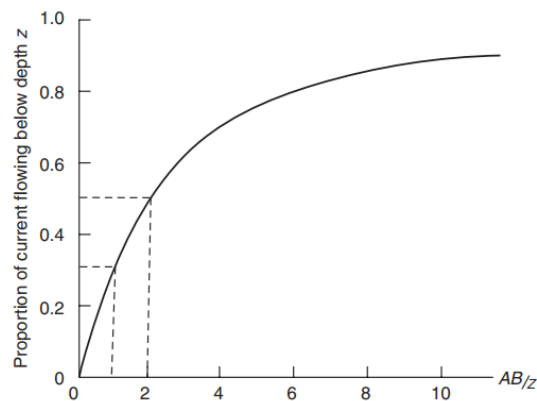


Fig. 4. 9, Proportion of current flowing below a depth z (m); AB is the current electrode half-separation. From Reynolds, John M., 2011

4.2 Induced Polarization

Induced polarization (IP) is a current-stimulated electrical phenomenon observed as a delayed voltage response in earth materials, associated with subsurface charge distributions.

According to the same physical principle, the self-potential (SP) method exploits the natural electrochemical processes that create a preferential free ions distribution.

This phenomenon has been noted by Conrad Schlumberger about 100 years ago, used during the II World War by USA Navy to detect mines at sea and then developed during the late 60s for exploration of porphyry and massive sulphide deposits. In recent decades, with the advance of instrumentations and computational abilities, has found increasing applications in groundwater and environmental studies as well as in characterizing subsurface organic contaminant plumes and other complex biogeochemical environments.

4.2.1 Theoretical background

Induced polarization represents the attitude of micro-heterogeneous materials (e.g., rock or soil) to transport and accumulate charge carriers (ions and electrons) due to the imposition of an external electric field. This effect is understandable only if the three main conduction mechanisms within the ground [56, Ward S.H. 1988] are tackled: electronic, electrolytic and surface conductivity (Fig. 4.10).

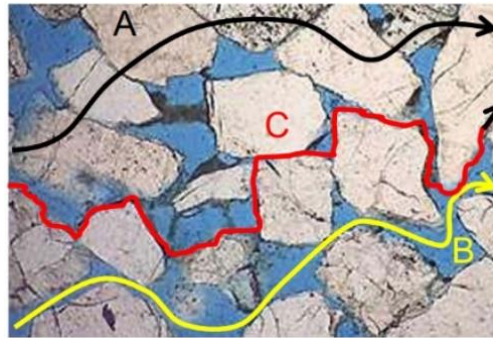


Fig. 4. 10, Electrical conduction mechanisms: A. electronic - by matrix, B. electrolytic - by pore water and C. surface conductivity - by grain-water interface. From Flores-Orozco, A. lectures

Thus, interfaces between pore-fluid electrolytes and minerals, very widespread in the subsurface, are associated with contrasts in conduction mechanisms and charge-carrier mobilities.

These generate an electrochemical impedance to current flow and therefore induce charges to accumulate at or near the mineral-electrolyte interface, polarizing the ground until the driving current is switched off. The impedance value depends on the size and polarity of the charge carriers.

Many fundamental studies have been performed on polarizations occurring in porous media and in colloidal suspensions, pointing out that, at IP frequencies (below 1kHz), the dominating mechanisms are:

- Membrane polarization, that can occur when electric current is passed through sediments in which clay is dispersed among larger mineral grains. The mobility of ions in relatively constricted pores is impeded by less-mobile ions: indeed, the surface of clay is negatively charged and attracts cations from the pore-fluid electrolyte.

Clay minerals act as ion selective membranes, retaining positive charges inside the Stern and Diffusive layers, comprising the Electrical Double Layer (Fig. 4.11), enhancing a stronger IP response than other sediments.

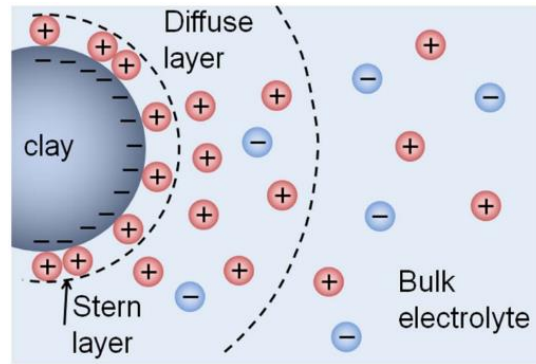


Fig. 4. 11, Electrical double layer. From Flores-Orozco, A. lectures

- Electrode polarization, found in rocks containing mineral grains of high electrical conductivity as metals that can partially block the movement of ions within the pore-fluid electrolyte.

The conduction mechanisms involved are different, electronic on the metal side and ionic on the electrolyte side. Therefore, electrons transfer from and back grain-electrolyte is permitted by redox reactions that start only after the overcoming of an energy barrier, the one that causes charges to accumulate at the junction and consequently a stronger IP response.
- A third type of polarization is the Interfacial or Maxwell-Wagner effect, a purely physical effect caused by electric charges that accumulate at conductivity interfaces within a heterogeneous medium. This effect can become important at relatively high IP frequencies, greater than 1 kHz, which may be of interest in the GPR technique.

4.2.2 Methods

IP effect can be measured in either time-domain (TDIP), commonly expressed with electrical resistivity (ρ) and chargeability (m), or frequency-domain (FDIP), given in terms of the complex electrical resistivity (ρ^*) with real and imaginary components, or by its magnitude and phase (Fig. 4.12).

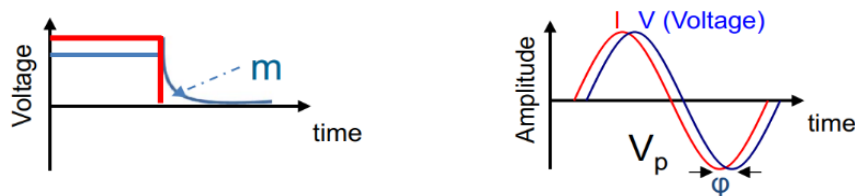


Fig. 4. 12, TDIP and FDIP. From Flores-Orozco, A. lectures

4.2.3 Time-domain IP

TDIP, also called pulse transient technique, measure the overvoltage as a function of time (Fig. 4.13).

If the ground is polarizable, opposite charges pile up along discontinuity surfaces that separates media with different resistivity during the current injection. The voltage measured in the subsurface drops rapidly from its initial value to a non-zero value and thereafter decays slowly after current interruption, often with a characteristic stretched-exponential shape.

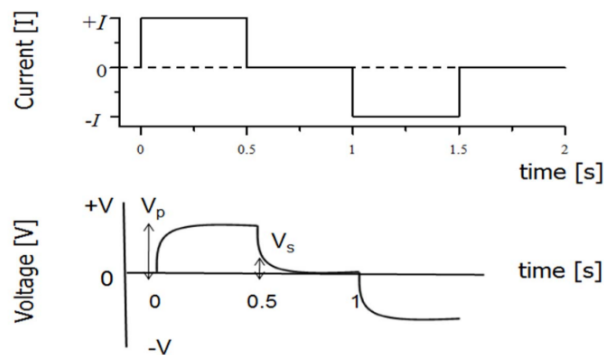


Fig. 4. 13, Alternating current injection and potential decay. From Flores-Orozco, A. lectures

A way to measure the time-domain IP effect passes through the chargeability m [mV/V], namely the area below the curve from the residual voltage after the current interruption (Fig. 4.14). The chargeability of the ground is its polarizability averaged over a predefined time window during the stretched exponential decay and measures the magnitude of the secondary voltage observed after switching the current off:

$$m_i = \frac{1}{(t_{i+1} + t_i) U_p} \int_{t_i}^{t_{i+1}} U(t) dt \quad (4.23)$$

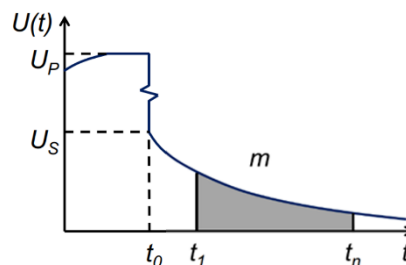


Fig. 4. 14, Chargeability. From Flores-Orozco, A. lectures

where t_1 typically is bigger than 100 ns.

The decay rate is related to different materials and it assess their capacitive effect: fast decay corresponds to small sediments and slow decay to bigger sediments (Fig. 4.15).

The main parameters that controls the size of the IP effect are the current source, the saturation, the type and amount of minerals, the porosity, the salinity and the texture of sediments.

Additionally, a significant is the interfacial geometric factor S_p [$1/\mu\text{m}$], the surface area of the mineral grains per unit volume of the saturating fluid.

Material	Chargeability, M [ms]	Material	Chargeability, M [ms]
20% sulfides	2,000 – 3,000	Quartites	5 – 12
8 – 20% sulfides	1,000 – 2,000	Argillites	3 – 10
2 – 8% sulfides	500 – 1,000	Sandstone	3 – 12
Volcanic tuffs	300 – 800	Schists	5 – 20
Sandstone	100 – 500	Gneiss	6 – 30
Dense volcanic rocks	100 – 500	Volcanic rocks	8 – 20
Shale	5 – 100	Gravel	3 – 9
Granite, grandodiorite	10 – 50	Alluvium	1 – 4
Limestone, dolomite	10 – 20	Water	0

Left side: observed values with a pulse-length of 60 s and integral chargeability values measured over the entire decay-curve.
 Right side: observed values with a pulse-length of 3 s, and integral chargeability values measured between 0.002 – 1 s

Fig. 4. 15, Chargeability values observed in different rocks. Modified after Telford, W.M., Geldart, L.P., Sheriff, R.E., 2010

4.2.4 Frequency-domain IP

In FDIP, an alternating current I of frequency f (range of mHz–kHz) is injected into the ground. The IP effect appears as a phase lag (φ_a) between the two sinusoidal waves of the applied current and the measured voltage.

A measure of the IP effect in the frequency domain is the phase angle φ [mrad] defined, at frequency f , as the difference in the phase of the measured voltage with respect to that of the injected current (Fig. 4.16). This value is diagnostic of the subsurface mineralization and, since the phase of the voltage lags behind that of the causative current, it is common to be negative ($-\varphi$).

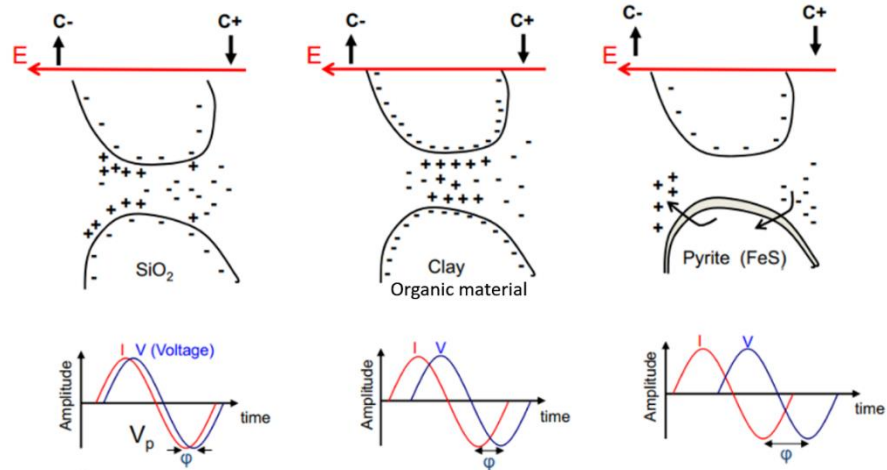


Fig. 4. 16, Electrical conduction and Induced Polarization effect in different earth materials. Modified from Flores-Orozco, A. lectures

The injected alternating current, variable in time, allow us to re-write the Ohm's law as a function of frequency:

$$V(\omega) = Z(\omega) \cdot J(\omega) \quad (4.24)$$

where the complex electrical impedance Z^* is defined in cartesian form with real and imaginary parts, the resistance (R) and the reactance (X), this last associated to energy storage phenomena:

$$Z = R + iX \quad (4.25)$$

Therefore, it is possible to express the impedance Z^* as the ratio between sinusoidal voltage V^* and current J^* , defined as complex quantities:

$$Z^* = \frac{V^*}{J^*} \quad (4.26)$$

$$Z^* = \frac{|V|e^{i(\omega t + \phi)}}{|J|e^{i\omega t}} = |Z|e^{i\phi} = \log_{10} |Z| + i\phi \quad (4.27)$$

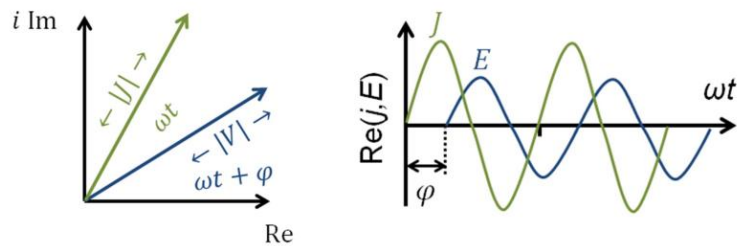


Fig. 4. 17, Complex electrical impedance. From Flores-Orozco, A. lectures

As can be deduced from this last expression (4.27), obtained using Eulerian notation, the evaluation of Z^* is directly linked to the knowledge of frequency-domain IP parameters, magnitude $|Z|$ and phase (ϕ).

Inserting the expression (4.27) into the apparent resistivity equation

$$\rho_a = K \frac{V}{I} = K Z \quad (4.28)$$

it results in:

$$\sigma^* = \frac{e^{i\varphi}}{K|Z|} = |\sigma| e^{i\varphi} = \sigma' + i\sigma'' \quad (4.29)$$

where σ^* is called complex conductivity. This quantity permits to describe the simultaneous conduction and capacitive properties of geological media, respectively with real and imaginary components.

In field surveys, the complex conductivity (σ^*) is measured at a single frequency.

Measurements repeated at different frequencies of the injected current (typically 0.01-1000 Hz) are commonly referred to as spectral induced polarization (SIP) and provide information about the frequency dependence of the electrical properties (conductivity and IP): fast polarization effects (e.g. small grains) take place at high frequencies, while slow effects (e.g. big grains) are characteristics at low frequencies.

The SIP method is essentially a measurement of complex resistivity ρ^* , where phase and magnitude are measured over a range of frequencies, and can be only performed with specific monitoring devices (e.g., MPT-DAS-1). For further information see [27, Kemna et al. 2012].

4.2.5 The complex conductivity

The electrical properties of the subsurface materials in the low frequency range (below ~100 kHz) can be represented by the complex conductivity (σ^*), or its inverse, the complex resistivity (ρ^*).

The real component (σ') of the complex conductivity represents the conductive electrical character (energy loss) while the imaginary (σ'') portrays the capacitive nature (energy storage, polarization) of ground materials (Fig. 4.18).

Otherwise, it is possible to express σ^* in terms of its magnitude ($|\sigma|$) and phase (φ):

$$\sigma^* = \sigma' + i\sigma'' = |\sigma| e^{i\varphi} \quad \sigma^* = \log_{10} |\sigma| + \varphi \quad (4.30)$$

where $i = \sqrt{-1}$.

Note that the real and imaginary parts of the complex conductivity are related by

$$\sigma'' = \sigma' \tan \varphi \quad (4.31)$$

Considering that in most practical applications the phase shift is commonly small ($\varphi < 100$ mrad), it is possible to assume that $\sigma' \approx |\sigma|$ and to approximate the phase with the ratio between real and imaginary component, i.e. $\varphi \approx \sigma''/\sigma'$.

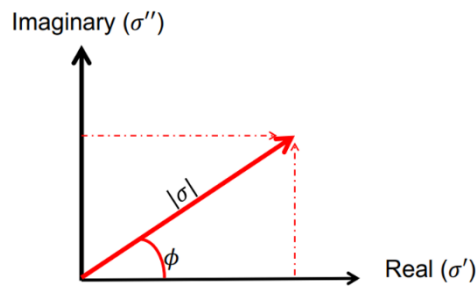


Fig. 4. 18, Real and imaginary components of the complex conductivity (σ^*). From Flores-Orozco, A. lectures

A rapidly evolving interaction between Earth science disciplines has led to the development of Biogeophysics, assessing that imaginary conductivity measurements are valuable proxy indicator for microbial growth and activity in porous media [see 1, Abdel Aal et al. 2004; 4, Atekwana et al. 2004; 13, Davis et al. 2006; 15, Flores-Orozco et al. 2011].

Specifically, it has been observed that microbial processes alter the interfacial electrical properties of media (e.g. mineral surface area weathering, ions releasing), enhancing electrical double layer polarization and causing a rocket in imaginary component (σ'').

Thus, changes in the real and imaginary conductivity can be used to infer biogeochemical processes associated with waste and contaminant degradation, thereby making the complex conductivity measurement a suitable method for, by the way, environmental monitoring.

4.3 Survey configuration and field measurements

4.3.1 Acquisition

The general approach for ERT and IP data acquisition consists in several electrodes placed along a straight line, which location and spacing are chosen according to the objectives of the survey. The measurement of a 2-D cross-section takes place using a resistivity meter, which automatically switches between current and potential electrodes according to the chosen sequence thanks to a multiplexer.

This instrument, which sends the current to each single electrode planned for the test, measures and stores the resulting potential for each quadrupole. The electrodes are linked to the resistivity meter thanks to one or more multicore cables.

For ERT method, current injection is performed through the electrodes as positive and negative pulses to remove the self-potential effects in the signal. The voltage is only measured during the current injection, averaging the potential for a full period of the square wave (Fig. 4.19).

Measurements of IP are made using the same electrode configuration, involving two current and two non-polarizable potential electrodes. When the current applied is

switched off, the voltage between the potential electrodes takes a finite and measurable time to decay to zero because the ground temporarily stores charge and acts like a capacitor.

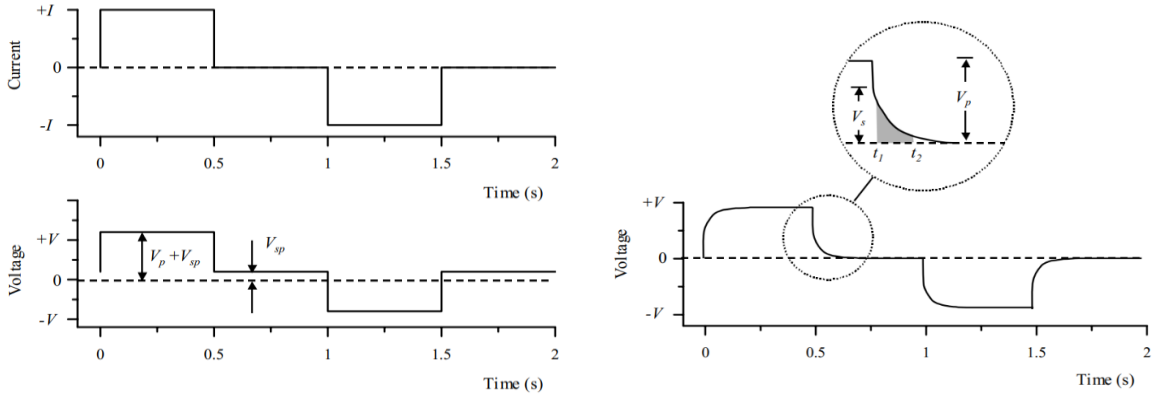


Fig. 4. 19, Left: Current injection as a square wave: alternating current and idealized voltage for field dc resistivity surveys, with primary voltage (V_p) and self-potential (V_{sp}) effects. Right: Real voltage waveform for measurement of time-domain induced polarization. From Binley, A., Kemna, A., 2005

4.3.2 Measuring protocol

ERT and IP measurements were conducted in the eastern part of the landfill area, close to the Mannsworth soccer field. In detail, our aim was to differentiate the shape of the landfill and visualize the supposed organic leachate in the subsurface.

The data were collected along one long profile of approximately 250m, the resultant of a roll-along of 4 single sections oriented parallel to the main field length, as depicted in Fig. 4.20.

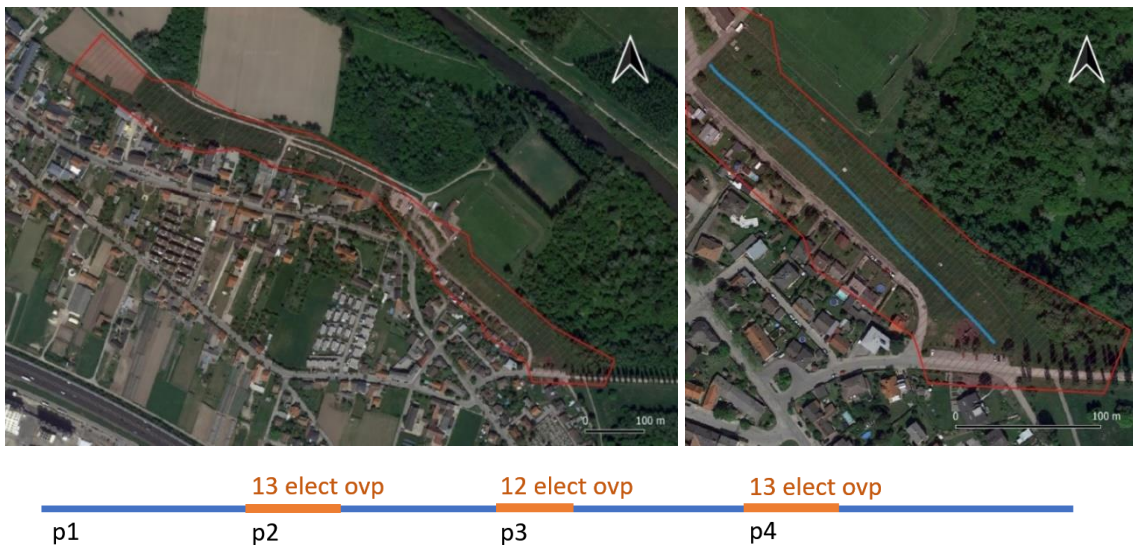


Fig. 4. 20, Study area in Mannsworth, with the reconstructed landfill shape depicted by red marker and the Syscal profile as a blue line. Downward, a schematic representation of the acquisition with the number of overlapped electrodes for each section

For each section, we used multi-core cables and 72 stainless steel electrodes, connected to them with take-out jumpers, with a spacing of 1 m to enhance resolution but sacrificing the investigation depth, according to the shallow target.

The data were acquired using a 10 channels resistivimeter Syscal Pro by IRIS Instruments, that made possible to collect resistivity and TD induced polarization measurements simultaneously through 2A square-wave current injection and a pulse length of 500 ms. The voltage decay was measured along 20 windows, having the same duration of 20 ms and starting after a delay of 50 ms after current shutoff.

Before each acquisition, the contact resistances were regularly checked through the resistivimeter.

An external 12V battery, connected to the Syscal, is used to generate the current for the acquisition.

The measuring device was always placed at the center of each segment, between electrodes 36 and 37.

GPS coordinates were acquired with the GNSS Leica GX1230GG / AX1202GG available at the TU-Wien for the profile georeferentiation.



Fig. 4. 21, Geoelectric equipment at the TU-Wien. From Flores-Orozco, A. lectures

We tested multiple gradient (MG) protocol that enhance the collection of multiple voltage readings for a given current injection. In MG protocol, the potential electrodes are inside of the current pathway (current dipole), designed to raise the signal-to-noise S/N ratio at the expense of lateral resolution (Fig. 4.22). Here, different potential dipoles were arranged within the current dipole, the length of whose increases with the skipped electrodes along the profile.

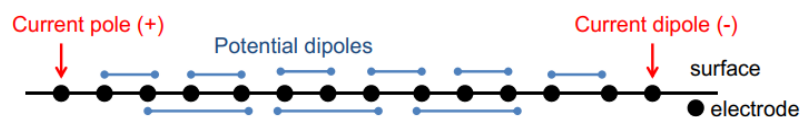


Fig. 4. 22, Multiple gradient configuration. From Flores-Orozco, A. lectures

A first profile was acquired on May 29th but, due to the noisy heavy rain and a small skip chosen for the second and third section of the roll-along, leading a shallow penetration, a second measurement on the same profile was taken on June 1st (Fig. 4.23).

Cable and electrodes were placed using the very line where electromagnetic and seismic surveys were conducted in order to exhaustively characterize the area and compare the results.



Fig. 4. 23, Acquisition moments in the landfill: the rainy conditions of the first field day on the left and the final and the definitive data collection on June 1st on the right

4.3.3 Pseudosection

The first result of a 2–D survey is a pseudosection, which is, in simple words, a suitable representation of raw data.

An example of the construction of a pseudosection is given in Fig. 4.24: each point represents a value of apparent resistivity as a function of quadrupole location along the profile and electrode spacing.

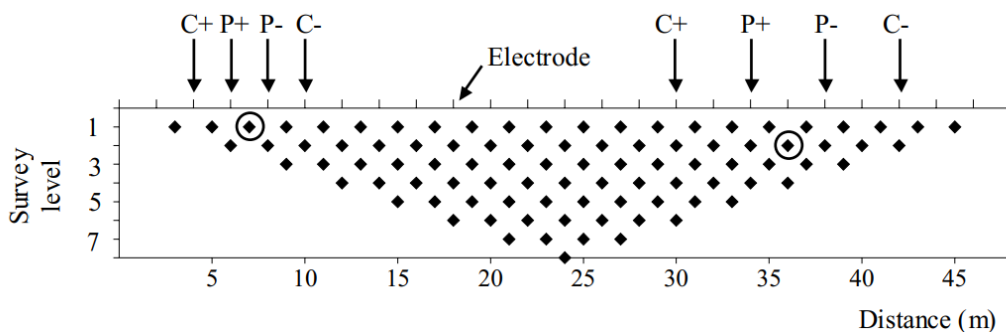


Fig. 4. 24, Building of a pseudosection using a Wenner array. From Binley, A., Kemna, A., 2005

The bigger is the separation between electrodes, the deeper is the survey level and, therefore, the higher is the pseudodepth of the pa value.

Fig. 4.25 shows pseudosections of apparent resistivity and phase related to the first measured segment of the acquisition, obtained by Matlab.

Even though the pseudosection is a useful tool, it is important to underline that it does not correspond to the real resistivity distribution, which can be obtained only through an appropriate inversion process.

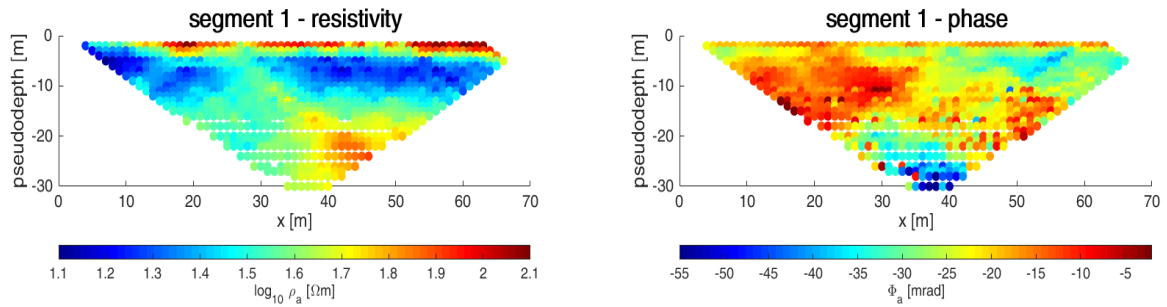


Fig. 4. 25, Pseudosections of apparent resistivity and phase obtained from the first segment of the roll-along

4.4 Processing and Inversion

The acquired data need an appropriate elaboration to be turned into the corresponding resistivity spatial distribution. This process requires mandatory passages, ranging from error assessment to data inversion, that have to be handled with particular care.

4.4.1 Quantification of data error

ERT measurements are affected by errors that need to be properly considered as they could influence the inversion process. Typically, these errors arise as a consequence of poor contact between electrodes and the ground, low current injection or other random external effects. Therefore, an appropriate error assessment is recommended to avoid annoying effects on the inversion procedure, as artefacts or heavy smoothing.

To define the valid ϕ_a values that undergo to inversion, it is important to identify outliers in the data.

All the gathered data were analyzed, processed and visualized with Matlab.

Our tests consider configurations related to high signal strength (favored by MG large dipole lengths) and with high spatial resolution (favored by MG smaller dipole lengths). Thus, the S/N of the resistance R measured (from which ρ_a is computed) is high, which prevents the distributions from “smearing out” at the lower and upper limits.

In order to assess the effect on the S/N of the measurement, the histograms in Fig. 4.26 illustrate the distribution of apparent resistivity (ρ_a), measured resistance (R), and apparent phase shift (ϕ_a) data collected along the total profile.

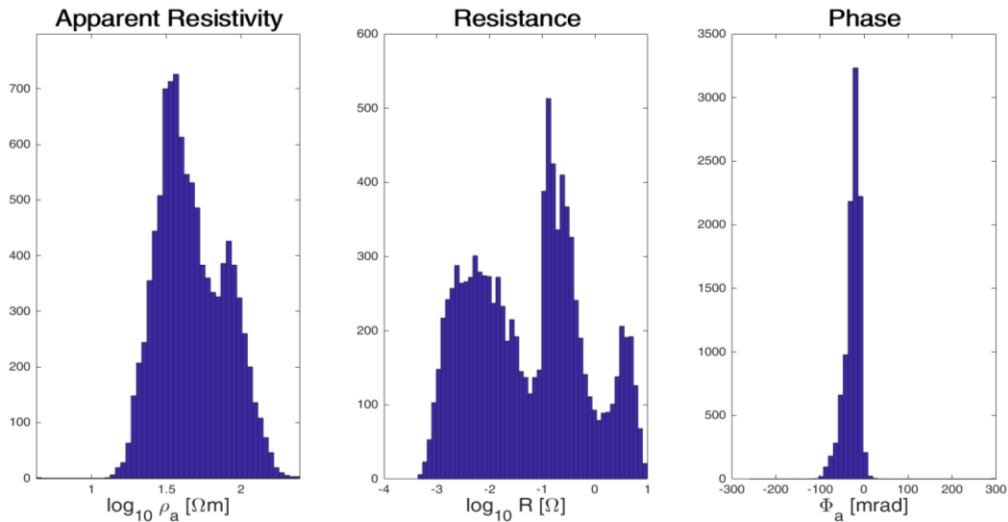


Fig. 4. 26, Histograms of the apparent resistivity ρ_a , measured resistance R, and apparent phase shift ϕ_a along the measured profile at the Mansworth landfill using MG measuring protocol. These schemes are referred to the total rolled profile, composed by four single sections

The analysis of the normal and reciprocal misfit is a common practice in electrical imaging, where reciprocal refers to the re-collection of the normal quadrupole after interchanging the current and potential dipoles.

Due to the MG measuring scheme, lacking reciprocal readings, first outliers were defined as those with collected potential readings below 1 mV, since their scattered trend shown in (Fig. 4.27). The same applied for negative R measured values, clearly related to poor contact between the electrodes and the ground.

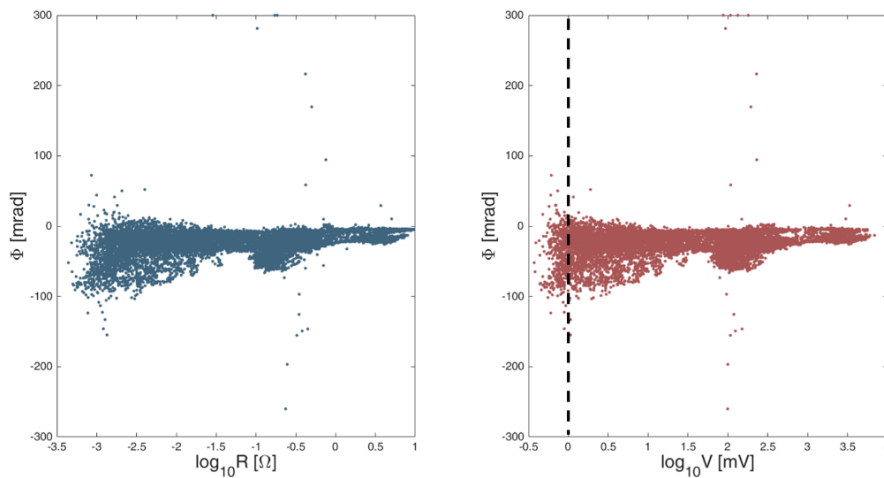


Fig. 4. 27, Measured resistance R and voltage V plotted against apparent phase ϕ

Since IP measurements are planned to record the delayed response of a chargeable subsurface, the measured resistivity phase shifts should be negative or zero ($\phi_a \leq 0$). As a result, positive ϕ_a values indicate the presence of random and systematic error in the data and consequently had been removed. The histograms in Fig. 4.28 show the leftover data after the filtering process just depicted, and the corresponding pseudosections are showed in Fig. 4.29.

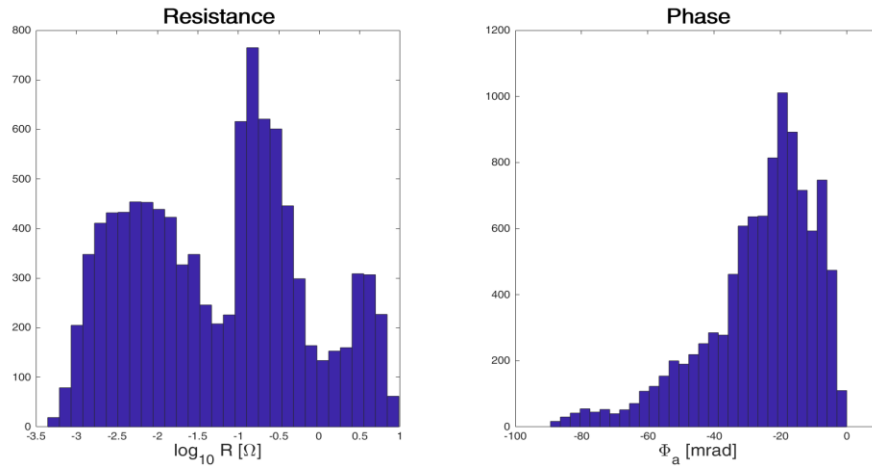


Fig. 4. 28, R and ϕ histograms after filtering procedure

The measurements remained after the removal of outliers were considered to be affected only by random errors, the size of which can be incorporated into the inversion.

Linear relationships between the measured resistances and their associated error, as proposed by [6, Binley et al. 1995; 49, Slater & Binley 2006], can be estimated only for dataset with reciprocal readings.

However, the negative power-law model, developed for SIP measurements, recently adopted to describe $\Delta\phi_a$ as a function of R [16] can be used for the inversion of datasets lacking reciprocal readings, such as our case [see 18, Flores-Orozco et al. 2018]

Absolute and relative resistance errors, describing the data uncertainty for the measurements collected in the Mannsworth landfill, were assumed by visual examination of data quality and relying on the analysis described in [16, Flores-Orozco et al. 2012].

Even through, each single section of the entire profile was analyzed and used as a test reference with the aim of evaluating the best inversion parameters.

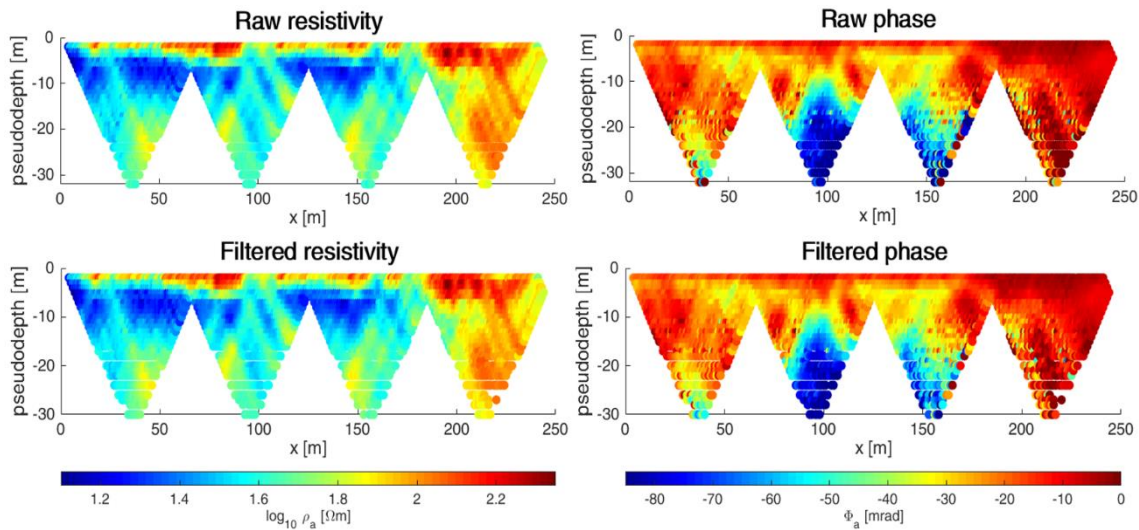


Fig. 4.29, Pseudosections before and after the filtering process

4.4.2 Modeling and data inversion

The main purpose of ERT and IP methods is to acquire the distribution of electrical properties about the interior of a domain based on a set of measurements conducted on its surface.

The investigated system is mathematically determined by a discrete model, obtained by computing theoretical responses from an assumed distribution of the electrical properties (Fig. 4.30).

This electrical forward problem, to be solved, requires the employment of numerical methods (i.e. finite element or finite difference), which are based on a representation of the domain realized thru a grid or a mesh, made of several nodes and elements. Hence, the solution representing the potential field is provided at each node.

To compute the real resistivity distribution that explains the dataset made of our electrical measurements, however, the “inverse problem” needs to be solved. Given some measured quantities collected on the surface, we use a theoretical relationship to derive the values of the set parameters of a model that reproduces the given field observations.

Unfortunately, both forward and inverse problems are difficult tasks because they have no unique solution: there exist a large number of models that effectively produce the same response, fitting the data within a given level of uncertainty.

Nevertheless, by systematically restricting the model search via predefined characteristics, a single relevant solution can be obtained. This is commonly achieved through the application of the “Occam’s razor” principle, which considers as the best solution the smoothest model agreeing with the data within their error level [12, Constable S.C. 1987]. This approach is based on iteratively minimizing an objective

function comprising both data misfit (measured and modeled) and a penalty term which considers deviations from the desired model.

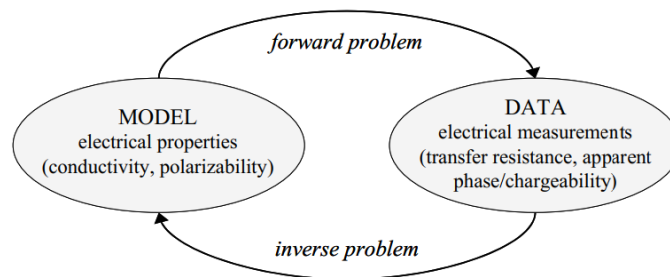


Fig. 4. 30, Definition of electrical forward and inverse problem. From Binley, A., Kemna, A., 2005

In this study, all datasets were inverted with CRTomo, a smoothness-constraint algorithm by Kemna (2000), which performs the inversion to the confidence level determined by an error model. From our given data set in terms of apparent resistivity and apparent phase shifts (ϕ_a), the algorithm solves for the distribution of complex resistivity on a 2D grid of finite-element cells.

The .cfg input file required by CRTomo for the inversion process contains, between the different significant parameters, the references to the dataset and grid paths, the relative and absolute resistance assumed errors, the phase error parameters, the background magnitude and phase and a smoothness regularization in x and z directions.

It was considered reasonable to assume a value of 10% for the relative resistance error because of the overall medium level of noise of the raw dataset. On the other hand, the absolute resistance error was estimated by the inspection of the resistance distribution showed in fig.10 and fixed at 0.001.

According to the target, a 20:1 horizontal-to-vertical smoothness was applied to the inversion and the background magnitude and phase values were left as standard 1000 [Ωm] and -1 [mrad] respectively.

The inversion processes were supervised by the inspection of RMS errors of resistance and phase between the experimental and the modeled data. At the end of each iteration and at the very end of the process, RMS values are computed and displayed in one output file (inv.ctr). In our case, the model converged after 3 iterations with an overall data RMS of 0.9909, in details 0.9912 for the resistivity and 2.520 for the phase, this last calculated with a phase error parameter available in the algorithm assumed to be 5 [mrad].

The results are saved in output files (rho'n'.mag, rho'n'.pha) where 'n' is the final iteration number: the point coordinates are associated to the respective resistivity and phase values. Always through Matlab, the model data obtained were plotted with the purpose to visualize the resulting sections (Fig. 4.31).

The colorscale was fixed by relying on the numerical observation of the results (10 to 315 Ohm*m, turned in \log_{10} values) and the dimensions of the section was set in accordance with the roll-along final length (250m) and the focused depth of interest (8m).

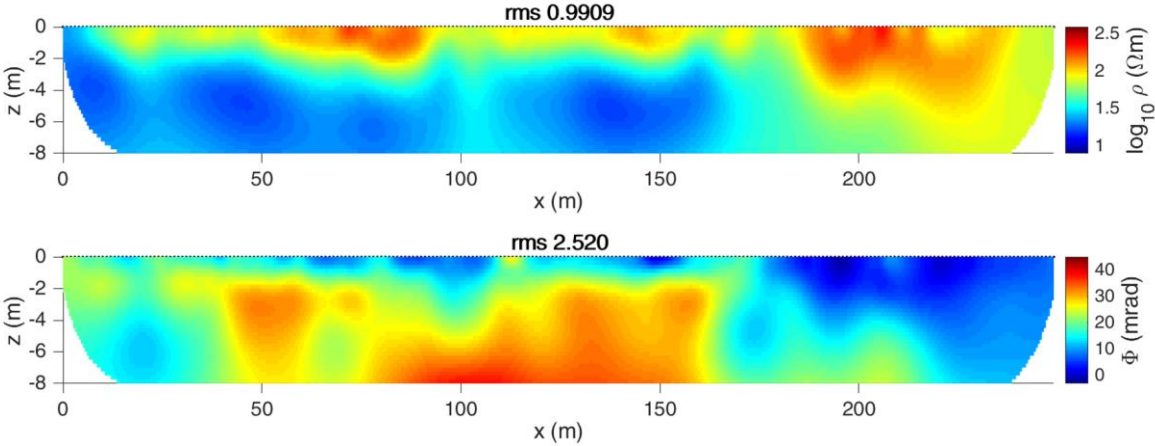


Fig. 4. 31, Resistivity and Phase imaging results from MG data collected along the Mannsworth profile

5 Electromagnetic Induction Methods

The electromagnetic induction (EMI) is a geophysical method that use a low frequency time-varying magnetic field as a source to excite electrical currents in the ground through the principle of electromagnetic induction.

In the literature, the term tends to be used to refer to a huge variety of systems sensitive to the electrical conductivity of the subsurface: changes in size, source functions and receiver-transmitter configurations reflect the scalability of EM methods (from cm to km). Thus, the range of applications of EM methods is large, according to the type of equipment used, and permits to play an important role in mineral exploration and engineering problems since at least the early 1960s.

One of the main advantages of the EM methods is that the process of induction does not require direct contact with the ground. Consequently, the speed with which EM surveys can be made is much greater and allows the method to be used from aircraft and ships, as well as down boreholes.

Data are typically collected as point readings of ground conductivity or in-phase taken at regular intervals along a survey grid, set out over the site area. The spacing of the grid-lines and reading stations is dependent whichever is appropriate: smaller the targets, closer the survey lines and denser spaced the readings.

These methods are sensitive principally to electrical conductivity σ [S/m], which characterizes the ease that current flows through the material when an electrical force is applied. Electric current I [A] quantifies the amount of charge that is moving by an observer in one second.

The conductivity of Earth's materials varies over many orders of magnitude and it is responsive to bulk changes in lithology, porosity, presence and nature of the fluid and metallic content.

A very rough indication of the range of resistivity (inverse of conductivity $1/\sigma$) for soil and rocks is presented in Fig. 5.1.

Rock type	Resistivity range (Ωm)
Consolidated shales	$20-2 \times 10^3$
Argillites	$10-8 \times 10^3$
Conglomerates	$2 \times 10^3-10^4$
Sandstones	$1-6.4 \times 10^8$
Limestones	$50-10^7$
Dolomite	$3.5 \times 10^2-5 \times 10^3$
Unconsolidated wet clay	20
Marls	3-70
Clays	1-100
Alluvium and sands	10-800
Oil sands	4-800

Fig. 5. 1, Resistivities of sediments and rocks, after Telford, W.M., Geldart, L.P., Sheriff, R.E., 2010

5.1 Theoretical background

In order to begin the study of time-varying electromagnetic fields, it is necessary to focus the attention on the basic physics of induction and classical electromagnetism. Therefore, it is essential to refer to J.C. Maxwell who, in the middle of XIX century, drew up the first modern theory of electromagnetism and predicted the existence of combined electric and magnetic (or electromagnetic) fields that propagate through space as electromagnetic waves.

Thus, EM methods use the response of the ground to the propagation of incident alternating electromagnetic waves which are made up of two orthogonal vector components, an electric intensity (\mathbf{E}) and a magnetic flux density or magnetic induction (\mathbf{B}), in a plane perpendicular to the travel direction (Fig. 5.2).

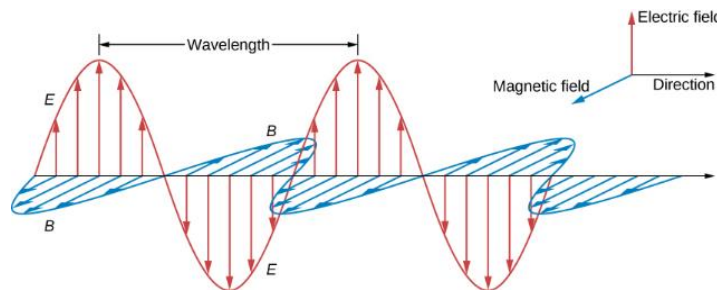


Fig. 5. 2, The plane wave solution of Maxwell's equations has the \mathbf{B} field directly proportional to the \mathbf{E} field at each point, with the relative directions shown. From phys.libretexts.org

An electromagnetic field may be defined in terms of 5 vector fields: \mathbf{E} the electrical intensity [V/m], \mathbf{D} the electric displacement [C/m²], \mathbf{J} the electric current density [A/m²], \mathbf{B} the magnetic induction [T] or [Wb/m²] and \mathbf{H} the magnetic intensity [A/m].

Maxwell's laws are essential to understand the behavior of constant electric and magnetic fields (quasi-stationary fields) used in the most electromagnetic methods.

For direct current (DC) applies the Gauss' laws:

$$\nabla \cdot \mathbf{E} = \frac{\rho}{\epsilon} \quad (5.1)$$

$$\nabla \cdot \mathbf{B} = 0 \quad (5.2)$$

where ρ is the electric charge [C/m³] and ϵ is the dielectric permittivity [C/Vm].

In case of alternating current (AC), Faraday's and Ampère's laws are implemented respectively:

$$\nabla \times \mathbf{E} = -\frac{\partial \mathbf{B}}{\partial t} \quad (5.3)$$

$$\nabla \times \mathbf{B} = \mu_0 \mathbf{J} + \mu_0 \epsilon_0 \frac{\partial \mathbf{E}}{\partial t} \quad (5.4)$$

For the particular case of EMI method, Faraday-Lenz and Ampère’s laws play the fundamental role: the first states that “temporal variations of the magnetic field cause an opposing electrical field” and for the latter “electrical currents and temporal variations of the electrical field cause a magnetic field” (Fig. 5.3).

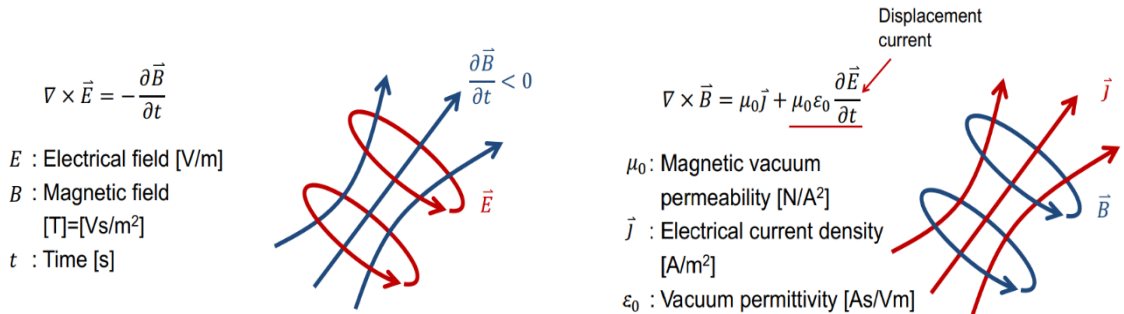


Fig. 5. 3, Representation of Faraday-Lenz (or Induction) and Ampere laws. From Flores-Orozco, A. lectures

EMI exploits the principle of electromagnetic induction by making use of a sensor system that generates a transient primary magnetic $\mathbf{B}_p(r,t)$ field by applying an alternating electric current at a fixed frequency which passes through a transmitter coil TX.

As shown schematically by the Fig. 5.4, a certain number of primary field lines (dark solid lines) flux through the conductive target. Due to the time-varying character of the magnetic field, the instantly generated electromotive force induces eddy currents (light solid lines) of density $\mathbf{J}(r, t)$ to flow in the conductor. These currents, in turn, subsequently generate a secondary magnetic field $\mathbf{B}_s(r, t)$ sensed by the receiver coil (dashed lines) that is characteristic of the target geometry, and its position and conductivity.

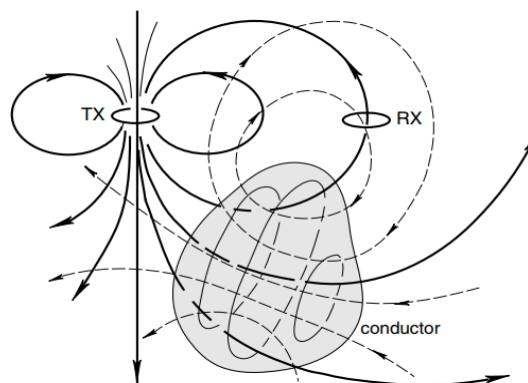


Fig. 5. 4, Schematic illustration of a loop-loop electromagnetic target prospecting. From Everett, Mark E. 2013

The RX coil measures the superposition of primary and secondary field, therefore the voltage induced contains both the primary signal from the TX and the secondary

electromagnetic response of the target (Fig. 5.5). Since the primary signal is known, depending only on the TX–RX configuration, it can be removed, leaving only the unknown target response.

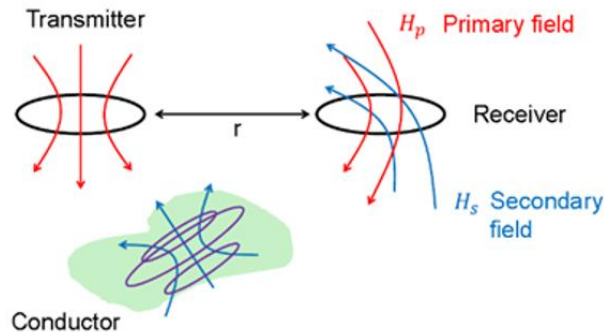


Fig. 5. 5, Representation of field injection and detection in TX and RX coils. From Flores-Orozco, A. lectures

To comprehend the EM method peculiarities, it is worthwhile to recall that the geological medium under investigation is considered to be electrically neutral because of its equal amount of positive and negative charge carriers. Consequently, where the subsurface is homogeneous there is almost no difference between the fields propagated above the surface and through the ground and the survey aim becomes the detection of targets with anomalous conductive properties.

The electrical conductivity is related to the density and mobility of the charge carrier within the medium. Therefore, an appreciable induced current does not flow in an insulator such as air or oil since, in these materials, the number density of mobile charges is negligible. It is the induced drift of mobile charges or eddy current J , acting as a secondary source of electromagnetic field, that generates the electromagnetic response measured by geophysicists.

In addition to the mobile charges that are present in conductive geomaterials, there certainly also exist bound charges that are not able to drift freely but nevertheless experience the Lorentz force F in the presence of an applied electromagnetic field. The motion of these bound charges leads to several types of polarization, investigated with the induced polarization IP method.

Therefore, bound charges, confined to individual atoms, and mobile charges, trapped at material interfaces, have no significant contribution to the EM induction response.

5.1.1 Methods

Electromagnetic methods can be classified as either frequency-domain (FDEM) or time-domain (TDEM) systems; the first use EM waves generated in either one or more frequencies, whereas the latter make measurements as a function of time. These

methods can be either passive, utilizing natural ground signals (e.g. magnetotellurics), or active, where an artificial transmitter is used either in the near-field (as in ground conductivity meters) or in the far-field (eg. Very Low Frequency Electromagnetic technology). A first basic classification of active EM systems is given in the figure below.

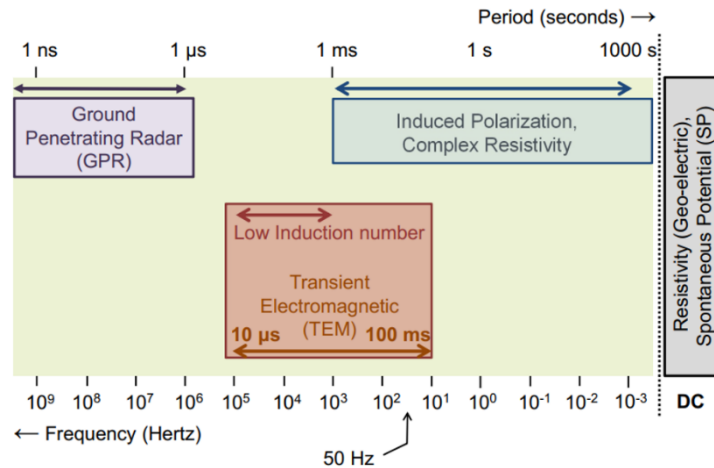


Fig. 5. 6, Classification of active EM systems as function of the employed frequency range. From Flores-Orozco, A. lectures

5.1.2 Electromagnetic methods at low induction number

Electromagnetic induction imaging results presented in this work were performed with the so-called terrain conductivity meters, or more precisely, low induction number electromagnetic methods. The controlled-source variant of the method utilizes low-frequency ($\sim 1\text{--}100$ kHz) time variations in electromagnetic fields that originate at or near the surface and diffuse into the subsurface.

The wavelength of the primary wave, with frequencies greater than 3 kHz, is of the order of 10-100 km while the typical source–receiver separation is much smaller ($\approx 4\text{--}100$ m). Consequently, attenuation due to wave propagation can be ignored and it appears appropriate to consider a planar behavior to the EM waves (Fig. 5.7).

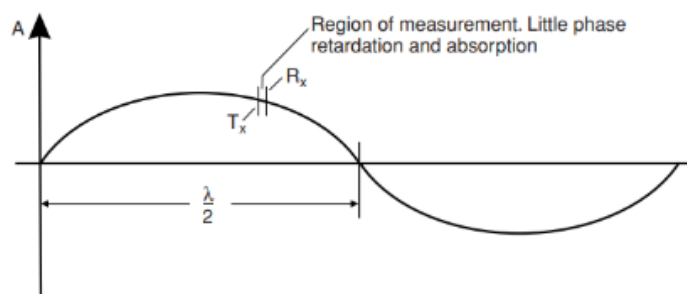


Fig. 5. 7, Source–receiver separation compared with the typical wavelength dimension. From Reynolds, John M., 2011

According to these conditions and assuming the absence of free charges, it is possible to rewrite the Maxwell's laws that describe the propagation of EM wave:

$$\nabla^2 \mathbf{E} - \sigma \mu \frac{\partial \mathbf{E}}{\partial t} = \varepsilon \mu \frac{\partial^2 \mathbf{E}}{\partial t^2} \quad \nabla^2 \mathbf{H} - \sigma \mu \frac{\partial \mathbf{H}}{\partial t} = \varepsilon \mu \frac{\partial^2 \mathbf{H}}{\partial t^2} \quad (5.5)$$

where \mathbf{E} is the electric field vector [V/m], σ the electric conductivity [S/m], μ the magnetic permeability [H/m], ε the electric permittivity [F/m] and \mathbf{H} is the magnetic field vector [A/m].

In both equations, the second derivative represents the wave propagation mechanism, the first derivative the energy dissipation, removed from the wave by the diffusive behavior of the two fields.

Through the Fourier transform it is possible to switch from time to frequency domain, removing thus the time derivatives and obtaining:

$$\nabla^2 \mathbf{E} - j\mu\omega\sigma\mathbf{E} = -\mu\varepsilon\omega^2\mathbf{E} \quad \nabla^2 \mathbf{H} - j\mu\omega\sigma\mathbf{H} = -\mu\varepsilon\omega^2\mathbf{H} \quad (5.6)$$

where j is the imaginary unit and ω is the angular frequency [rad/s].

Now it is possible to identify the wave propagation term where appears ε , and the dissipative one, characterized by σ . The Loss Factor allows to identify the mutual dominance of the two mechanisms according to the value of EM parameters of the medium, and it is expressed as:

$$P = \frac{\sigma}{\omega\varepsilon} \quad (5.7)$$

The diffusive regime is marked by the requirement $\sigma \gg \omega\varepsilon$, which brings $P \gg 1$. The dielectric permittivity plays no physical role in the EM induction method.

Furthermore, the Loss Factor delineates the main distinction from the ground-penetrating radar (GPR) technique that utilizes a higher frequency range >1 MHz, for which wave propagation is the dominant mechanism ($P \ll 1$). Instead, EMI measurements respond almost entirely to the bulk subsurface electrical conductivity σ and, in particular, the spatial distribution of highly conductive zones.

5.1.3 Low induction number electromagnetic imaging

The operating principle of the terrain conductivity meter is based on classical EM induction theory. A time-harmonic current of the form $I(t) = I \sin(\omega t)$ is passed through the TX loop and the primary magnetic field due to the current flowing in the transmitter is in-phase with the current:

$$\mathbf{B}_p(\rho, t) = \mathbf{B}_0(\rho) \sin(\omega t) \quad (5.8)$$

where ρ is the radial distance in a cylindrical coordinate system originated at the center of the TX loop.

A conductive ground anomaly responds to the time-varying primary magnetic flux by establishing a system of electromagnetic eddy currents, whose secondary magnetic field

$\mathbf{B}_s(\rho, t)$ is organized such that it tends to oppose the change $\partial\mathbf{B}_p/\partial t$ in primary flux. Essentially, the changing primary flux establishes an electromotive force (emf) in the ground, which responds by generating a back-emf to restore the equilibrium that existed before the change occurred in the primary flux, according to Lenz's law.

The secondary magnetic field then has the form

$$\mathbf{B}_s(\rho, t) = \mathbf{B}_1(\rho) \sin(\omega t + \varphi) \quad (5.9)$$

where $|\mathbf{B}_1| \ll |\mathbf{B}_0|$, and φ is the phase shift caused by the induced currents which are not completely in-phase with the primary magnetic flux. The magnitude of the phase shift depends on the electrical conductivity of the ground: if it is perfectly conducting, $\varphi=90^\circ$ and the secondary magnetic field is completely out of phase, otherwise if it is perfectly resistive, $\varphi=0^\circ$ and the secondary magnetic field is completely in-phase.

In general, as shown in Fig. 5.8, the secondary magnetic field is delayed and attenuated with respect to the primary magnetic field, indicative of EM induction as an energy-dissipating $\partial/\partial t$ process.

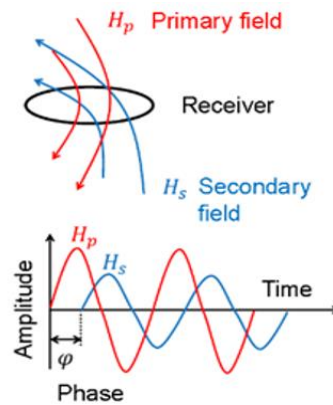


Fig. 5. 8, Primary and secondary fields detected in Rx coil. From Flores-Orozco, A. lectures

Through the identity

$$\sin(\omega t + \varphi) = \sin \omega t \cos \varphi + \cos \omega t \sin \varphi \quad (5.10)$$

it is possible to decompose the total magnetic field $\mathbf{B}_T(\rho, t)=\mathbf{B}_0(\rho, t)+\mathbf{B}_p(\rho, t)$ into two orthogonal components:

$$\begin{aligned} \mathbf{B}_T(\rho, t) &= \mathbf{B}_0(\rho)\sin\omega t + \mathbf{B}_1(\rho)\sin(\omega t + \varphi) \\ &= \mathbf{B}_0(\rho)\sin\omega t + \mathbf{B}_1(\rho) \sin \omega t \cos \varphi + \mathbf{B}_1(\rho) \cos \omega t \sin \varphi \\ &= [\mathbf{B}_0 + \mathbf{B}_1 \cos \varphi] \sin\omega t + [\mathbf{B}_1 \sin \varphi] \cos \omega t \end{aligned} \quad (5.11)$$

such that $\mathbf{R} = |\mathbf{B}_0 + \mathbf{B}_1 \cos \varphi|$ is called the real (in-phase) response and $\mathbf{Q} = |\mathbf{B}_1 \sin \varphi|$ is the quadrature (out-of-phase) response, that in most cases is very small c.a. 10^{-6} . The quantities (R, Q) are measured by the EM instrument.

Given that $\mathbf{B}=\mu\mathbf{H}$, it is now possible to define the Transfer function as the ratio between the secondary and primary field detected in the receiver

$$\frac{H_S}{H_P} = \frac{b^2 + ib}{1 + b^2} \quad (5.12)$$

where the induction number (b), for a given system, is a function of the angular frequency of the primary field (ω), the separation between the transmitter and receiver coils (l), the magnetic permeability (μ) and the bulk electrical conductivity (σ) of the earth.

$$b = \mu\sigma\omega l^2 \quad (5.13)$$

Terrain conductivity meters are designed with l and ω to work at low induction number ($b < 1$), at which the response is dominated by the ratio between secondary to primary magnetic field (Fig. 5.9).

If $b \ll 1$, the imaginary “quadrature” component has all the information about the electrical conductivity of the ground,

$$Im \frac{H_S}{H_P} \gg Re \frac{H_S}{H_P} \quad (5.14)$$

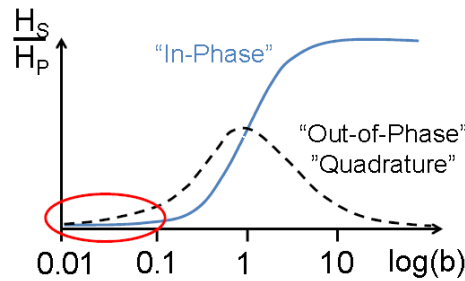


Fig. 5. 9, Real and imaginary components of the magnetic field, with the low induction number zone inside the red circle. From Flores-Orozco, A. lectures

and the transfer function for coplanar coils over a homogeneous half space can be written as

$$\frac{H_S}{H_P} = \frac{i\mu\omega\sigma r^2}{4} \quad (5.15)$$

Assuming that μ in subsurface materials is close to one as in vacuum, the measured response is then only controlled by the electrical properties. This fact permits to obtain the apparent electrical conductivity σ in the subsurface quasi in real time

$$\sigma = \frac{4}{\mu_0\omega r^2} Im \left(\frac{H_S}{H_P} \right) \quad (5.16)$$

and, as a contactless technique, EMI permits to map large areas in reasonably low acquisition times. Over highly conductive terrain only, (e.g. metal structures), the induction number increases significantly and the readings in [S/m] are no longer valid.

Values of σ represent a nonlinear average of the electrical conductivity values of the examined volume across a depth range that depends on the coil distance and orientation. Tx and Rx coils can be orientated horizontally (horizontal coplanar, HCP) or vertically (vertical coplanar, VCP) with respect to the ground surface. Increasing the coil separation,

in combination with VCP loops, enhances the depth range for the σ measurement [see 31, McNeill J.D. 1980].

Modern commercial instruments typically provide more than one Tx/Rx pair and therefore can provide σ for different depth ranges.

By the end, vertical profiles of the electrical conductivity of the examined volumes can be obtained from inverse modelling of σ data sets measured for different depths of investigation (i.e., varying coil separation and orientation).

5.1.4 Attenuation and Skin Effect

The depth of penetration of the EMI method is limited by the efficiency of the conversion of the transmitted electromagnetic energy into kinetic energy of the mobilized subsurface charge carriers. In an isotropic resistive medium, EM waves would travel virtually indefinitely. However, in the real world, where surface conductivities are significant, the depth of penetration is often very limited and the waves are damped (Fig. 5.10).

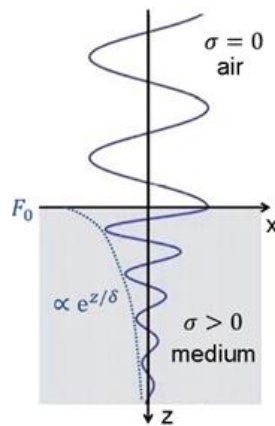


Fig. 5. 10, Damping of an EM wave. From Flores-Orozco, A. lectures

Amplitude of EM radiation decreases exponentially from the surface towards the inside and the attenuation of a downgoing planewave is given by

$$F(z) = F_0 e^{-z/\delta} \quad (5.17)$$

where F_0 is the original amplitude and δ is called skin depth [m], which represents the distance a wave must travel before its amplitude has decayed by a factor of $1/e$ (37%) from its initial amplitude

$$\delta = \sqrt{\frac{2}{\mu\omega\sigma}} \quad (5.18)$$

The depth of penetration is largely a function of frequency and the conductivity of the media present through which the EM radiation is to travel (Fig. 5.11), where $\omega = 2\pi f$ [radians/s] and f is the frequency, σ [S/m] is the conductivity, and μ is the magnetic permeability.

In the EM method, the magnetic permeability is almost always assumed to be equal to its free space value, $\mu = \mu_0 = 4\pi \times 10^{-7}$, even in the presence of magnetite-bearing rock formations.

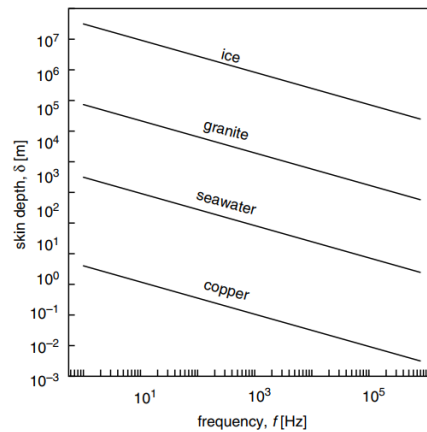


Fig. 5.11, Frequency dependence of skin depth for some different earth materials. From Everett, Mark E. 2013

A realistic estimate of the depth to which a conductor would give rise to a detectable EM anomaly is $\approx \delta/5$ (rule of thumb).

As stated before, the usual frequencies ($< \text{kHz}$) used in EMI exploration, attenuation effects are virtually negligible, but signal losses occur by diffusion.

Given a known frequency for a particular equipment system, the unknown is the vertical variation of conductivity with depth. However, the higher the electrical conductivity σ , the greater the efficiency and consequently the smaller the depth of penetration.

5.2 Survey configuration and field measurements

5.2.1 Acquisition

In this study we applied EMI measurements to map lateral changes in subsurface electrical properties using the CMD-Explorer by GF Instruments (Fig. 5.12), a multi-depth probe which uses three receiver coils with separations of 1.48 m, 2.82 m, and 4.49 m to the transmitter coils.

The Explorer adopt an operating frequency of 10kHz and the acquisition can be performed both in manual and in continuous mode.

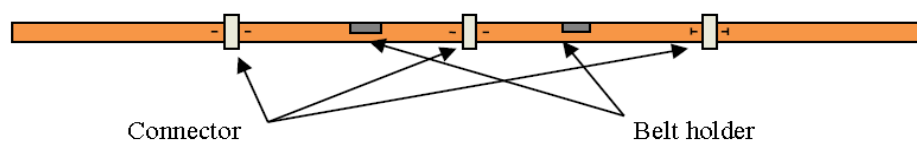




Fig. 5. 12, CMD-Explorer used in this work, a picture during its use in the landfill and an illustration taken from the GF Instruments user manual

5.2.2 Measuring protocol

All measurements on the landfill area in Mannsworth were performed in continuous mode using both Hi and Lo settings, for effective depth ranges of 2.2 m, 4.2 m, 6.7 m and 1.1 m, 2.1 m, 3.3 m respectively.

The sampling period was 0.5s, hence at an average walking speed (5 km/h) σ_a values were collected approximately every 0.7 m along the walking tracks.

The pattern used to cover the entire area (c.a 60mx200m) consisted in two sets of parallel profiles: the first composed by straight segments separated 4m each other, the second by diagonal tracks in the opposite direction, as presented in Fig. 5.13. However, the opposite walking direction between the two sets led to mirror structures in the diagonal profiles because of change in the orientation of the coils. As this is a well known problem arising in electromagnetic methods, the dataset collected along diagonal profiles were nevertheless examined but then discarded in the final σ_a output, also because the normal ones were dense enough to properly cover the area.

In addition, a single profile which crosses the whole field length was acquired, located on the same ERT and seismic acquisition line (Fig. 5.14).

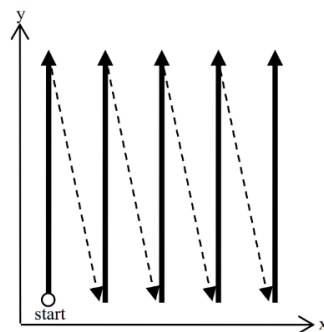


Fig. 5. 13, CMD Explorer acquisition pattern. From GF Instruments user manual

The measured conductivity values were geo-referenced by GPS measurements: for each single segment were acquired 2 GPS measurement, one at its start and one at its end, and then linearly interpolated to recreate the path walked with the Explorer.

In total, the data set consists of approximately 20000 σ_a values with the survey performed within 10 h.

EMI measurements were planned to map the entire extension of the area and delineate lateral variations in the electrical conductivity. In this study we only present maps of the σ_a directly recovered from measurements, not discussing the inversion of EMI data and associated uncertainties, which is required to solve for vertical variations in σ_a . Each map was obtained by plotting the geo-referenced measured σ_a values on QGis (Fig. 5.15).



Fig. 5. 14, Distribution of measurement points from the CMD-Explorer: the area mapped (direct -orange- and diagonal -blue- lines) and the longitudinal -red- profile, georeferenced and plotted in QGis

5.3 Processing and results

As stated before, we had no interest in recreating a conductivity model with electromagnetic dataset but only to obtain a fast overview of its apparent lateral variations in the study area. For this reason, the data were analyzed before with Matlab, removing the negative σ_a values, considered to be affected by random errors, and then just visualized in in order to compare the results obtained with the other techniques.

In general, all the maps reveal consistent patterns and σ_a values, permitting the identification of two main regions: (i) a first area of elevated σ_a (> 50 mS/m) that occupies the main surface of the landfill located in the north-west side and a second (ii) area characterized by low σ_a values (< 10 mS/m), located at the south-eastern region of the site, corresponding to the flattening of the topography.

Higher σ_a values can be observed following the south borders of all the shallowest maps, clearly related to the metal households' pipes of the nearby village.

To evaluate the similitudes for the consecutive depth ranges, in Fig. 5.15 different images are presented. We note here, that anomalously high σ_a values (> 100 mS/m) are associated with the response of metal from anthropogenic structures (e.g., pipes and metal plates) also seeping out from the ground and will not be further addressed.

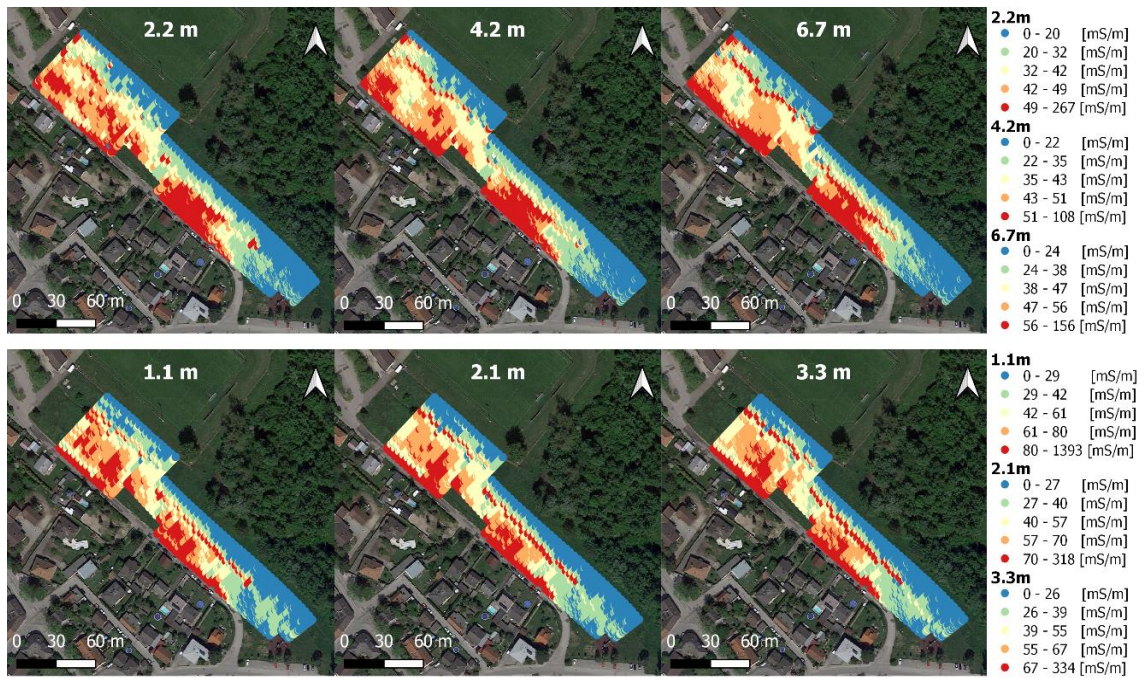


Fig. 5. 15, Different σ_a images for consecutive depth ranges of the CMD-Explorer, georeferenced and plotted in QGIS

Considering the minor differences between the maps of 1.1, 2.1 and 3.3 m, characterized by an only modest variation in σ_a (~ 5 mS/m), we can interpret only minimal vertical variations in shallow subsurface materials (between 0.5 and 3 m depth). The same pattern can be visible in all the maps of Hi configuration, with a homogeneous decrease in σ_a values, due to the distancing of the influence of the most superficial pipes and metal structures.

6 Results and Discussions

The aim of this chapter is to discuss the results obtained. A sequence of sections is made to describe them for each technique separately.

6.1 EMI

Fig. 6.1 presents the interpolated maps of σ_a values for the six collected depth ranges (Lo mode: 1.1, 2.1, 3.3 m - Hi mode: 2.2, 4.2, 6.7 m), displayed with Matlab to observe with a more accurate and customizable scale the noticeable differences. As stated before, given the higher variability in σ_a observed in the shallower EMI measurements, we classify the area above the 5m into two main regions arranged in west-east direction: (i) a high apparent conductivity region (>50 mS/m) related to shallowly corrugated topography and (ii) a region of lower apparent conductivity values (< 10 mS/m), associated to a flattening in the topography. Shallow metallic structures contaminate the dataset with anomalously high σ_a values, and are clearly identified in the most superficial maps.

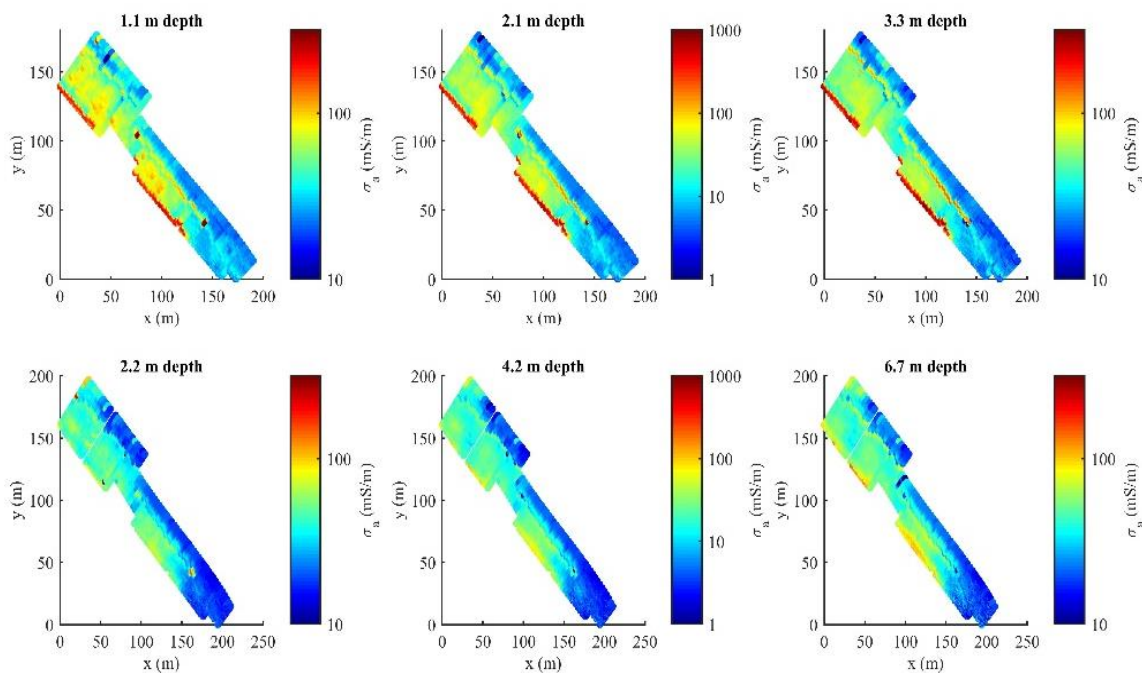


Fig. 6. 1, Interpolated maps of σ_a values acquired for the six collected depth ranges, visualized with Matlab

Comparison of the maps reveal a significant increase in the σ_a values for the central area of the landfill. Such increase in the electrical conductivity suggests the presence in leachate and organic gas content in that area, but also the occurrence of the aeration system that cross the landfill body, assumed to be between 1.2 and 2 m deep [8, Brandstätter et al. 2013].

The correlation between the changes in topography and the σ_a features suggests a link between the EMI maps and geomorphological patterns. The superficial sway of the ground shows a spatial correlation with higher σ_a values in all EMI maps, presumably due to gas content and subsidence, related to waste compaction and degradation.

The lateral variations in the σ_a values in all EMI maps may be explained by the different materials, solid, leachate and gasses, filling the landfill. Furthermore, σ_a patterns observed also in all EMI maps are consistent with the location of the lateral ending of the landfill, which is characterized by a transition in the south-eastern region from high (~ 50 mS/m) to low (~ 10 mS/m) conductivity values.

The higher degree of organic matter and gasses constituent the leachate, in addition to the aeration pipes that is known to pass through the landfill, explain the high conductivity pattern that shapes the scanned area and allows the identification of its lateral ending. The display of the longitudinal profile acquired over the same area with ERT, IP and SW methods, help us to set the landfill ending at around 205 meter (where the 0 m correspond to the North-West side, close to the parking) (Fig. 6.2).

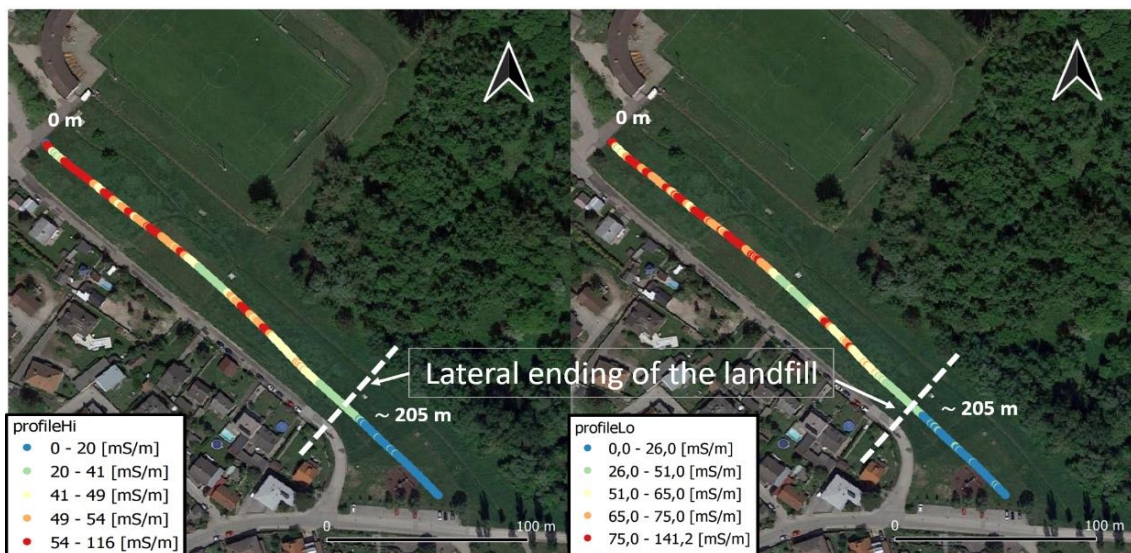


Fig. 6. 2, Apparent conductivity values along the profile acquired in Hi (left) and Lo (right) mode, georeferenced and plotted in QGIS

It is necessary to consider the sensitivity at depth associated with the geometry of the instrument in order to interpret the different EMI maps in Fig. 6.1 (the depth means depth under the probe).

Thus, the highest sensitivity for 2.2m and 4.2m maps is find out to be between ~ 0.25 and 3 m depth, clearly demonstrating the influence of conductive waste materials, and shallow biogas and leachate production, on the σ_a values. Instead, the sensitivity of deepest EMI measurements (6.7m) is assumable to be between 0.5 and 4 m (Fig. 6.3). Hence, the increase in σ_a values at depth for the central area of the landfill seems to be

related to the contribution of both the waste and degraded materials both the unit below. For further details reference is made to [31, McNeill J.D. 1980; 23, GF Instruments short guide].

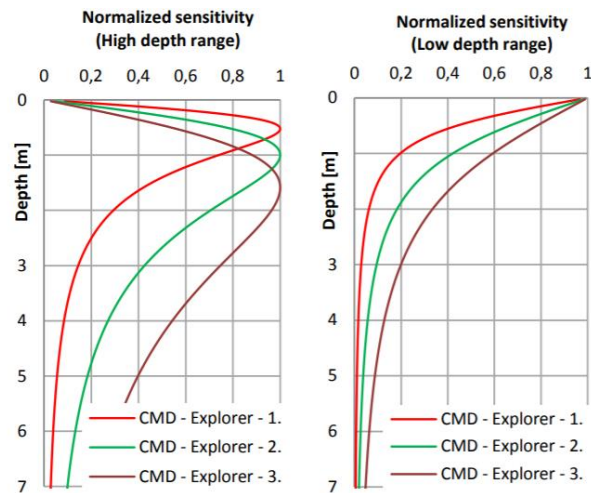


Fig. 6. 3, Plots of the normalized sensitivity function for the three depth ranges in Hi and Lo depth range for the CMD-Explorer. From GF Instruments: Short guide for electromagnetic conductivity mapping and tomography

6.2 ERT & IP

The ERT results from the longitudinal profile show the presence of an upper more resistive body ($\sim 300 \Omega\text{m}$, Fig. 4.31), associated to the top and excavated soil which outlines the dump, reaching approximately 2 m depth from the surface.

Below this, the resistivity values go down, outlining a conductive area possibly explained by the presence of the municipal solid waste in addition to the construction and demolition waste, which are expected to fill the deposit at such depths (Fig. 1.2).

However, the thickness of this irregular body is definitely bigger than the assumed waste width and it is characterized by an unclear boundary. This result can be explained considering a vertical migration of conductive leachate at the bottom of the landfill and beneath it.

The increasing of resistivity in the south-eastern part of the profile, with a sharp transition from $\sim 10 \Omega\text{m}$ to $\sim 300 \Omega\text{m}$ allows to indicate the lateral ending of the landfill, in completely agreement with EMI results showed before (Fig. 6.1, Fig. 6.2). The higher resistivity values of the landfill's surroundings and the lack of conductive anomalies are fairly associated to the undisturbed alluvial deposits that compose the area, finding then a favorable match with the available stratigraphic surveys [see 55, Valtl M. 2005].

The IP measurements, on the other hand, seem to indicate the existence of polarizable spots linked to the aeration system pipes, irregularly arranged but persistent into the landfill body between 2 and 8 m depth.

These lateral variations may be also indicative of the presence of biogas and ions caused by bacterial activity, thus linked to variable hydraulic properties (i.e. porosity, hydraulic conductivity) and consequently zones of preferential accumulation of biochemical reaction products.

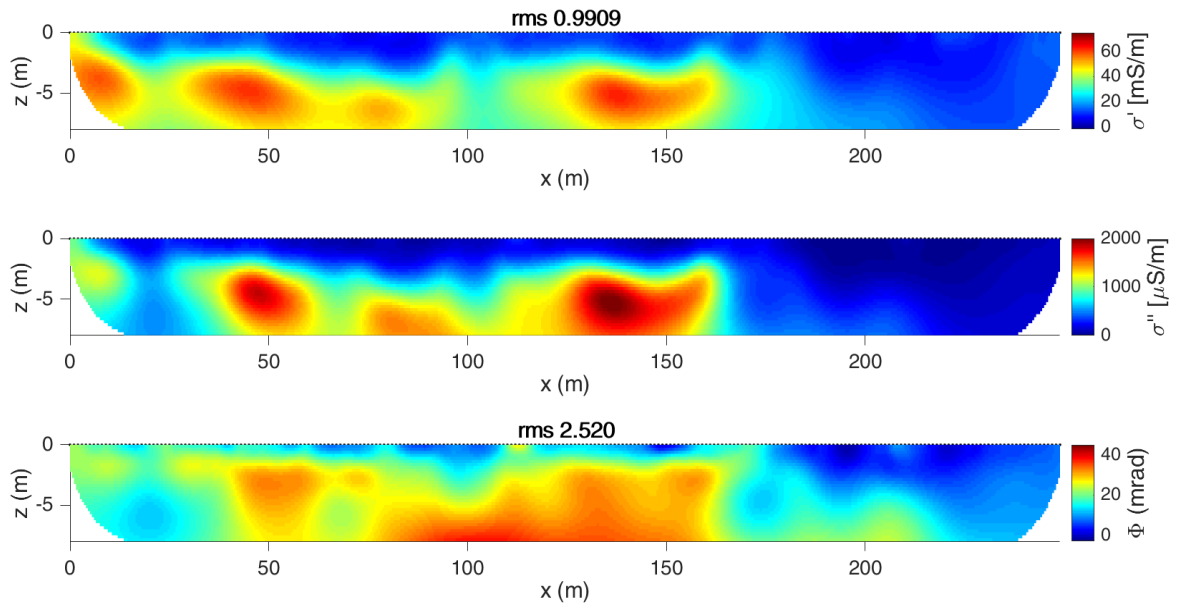


Fig. 6. 4, Imaging results expressed in terms of the real and imaginary components of the complex electrical conductivity followed by phase plot, along the Mannsworth profile. Courtesy of Flores-Orozco

The interpretation of solely resistivity properties gained by means of ERT can be limiting. In this regard, the real (σ') and imaginary component (σ'') of the complex conductivity are separated and showed in Fig. 6.4.

Whether the first represents the conductive electrical character, here related to the thickness of the waste deposit, the second is sensitive to variations in capacitive behavior. The outcomes appear to show two strongly capacitive spots located at 5 m depth in correspondence of 50 and 150 m from the beginning of the profile, and a minor third deeper anomaly located around 80 m.

As stated previously, this might be related to the unevenly presence of gas in depth in addition to the existence of the aeration system. Increasing the content of biogas and considering the pipes (e.g., between 2 and 8 m depth), σ'' increases in spots reaching values higher than 2000 $\mu\text{S}/\text{m}$.

The σ' profile reveals only minor changes down to 8 m. There is an increase in conductivity values from ~ 1 mS/m between ground surface and 2 m depth to ~ 60 mS/m between 2 and 8 m, supposedly indicating a rising in conductive filling material and leachate, as stated before.

Given the partial clearness of the field results, somewhat due to the physical limitations encountered in the nature of the site, we resorted to the support of MASW, in order to

discriminate the landfill bottom. Thus, in comparison with previous studies, the implementation of surface waves method beside the classical related almost on the electrical properties of the subsurface, had allowed an improved understanding and interpretation of the imaging result

6.3 Surface Waves

The obtained results from the application of MASW technique confirm its reliability and sensitiveness to mechanical properties of the medium, clearly emphasizing the differences between the area of filling material and the subsoil beneath the landfill. Frequency – Phase velocity plots shown before (Fig. 6.5), already point out that diversity. In the first two pseudo-2D sections, a marked and substantial increase in velocities with depth is shown (from less than 100 m/s to above 280 m/s), with a clear step located at \sim 4m. This result is broadly in agreement with the assumed section in correspondence with the landfill and even the velocities are consistent with the excavated silty soils with filling waste and the continental silty sands respectively, clearly marking the bottom of the landfill.

The third profile, on the other hand, is referred to a location who crosses the south-eastern limit of the landfill, estimated at around 205 m, characterized by the transition to continental silty sands undisturbed soils with a general higher velocity range (230-300 m/s).

Some small discrepancies are evident by comparing the outcomes obtained by normal and reverse shots related to the same investigated point in depth (Fig. 3. 25). This is reasonably due to the lack of homogeneity of the area and the consecutive energy dispersion, which promotes the existence of higher vibrational modes. These last, however, fall outside from the goals of this study and for this reason have not been considered.

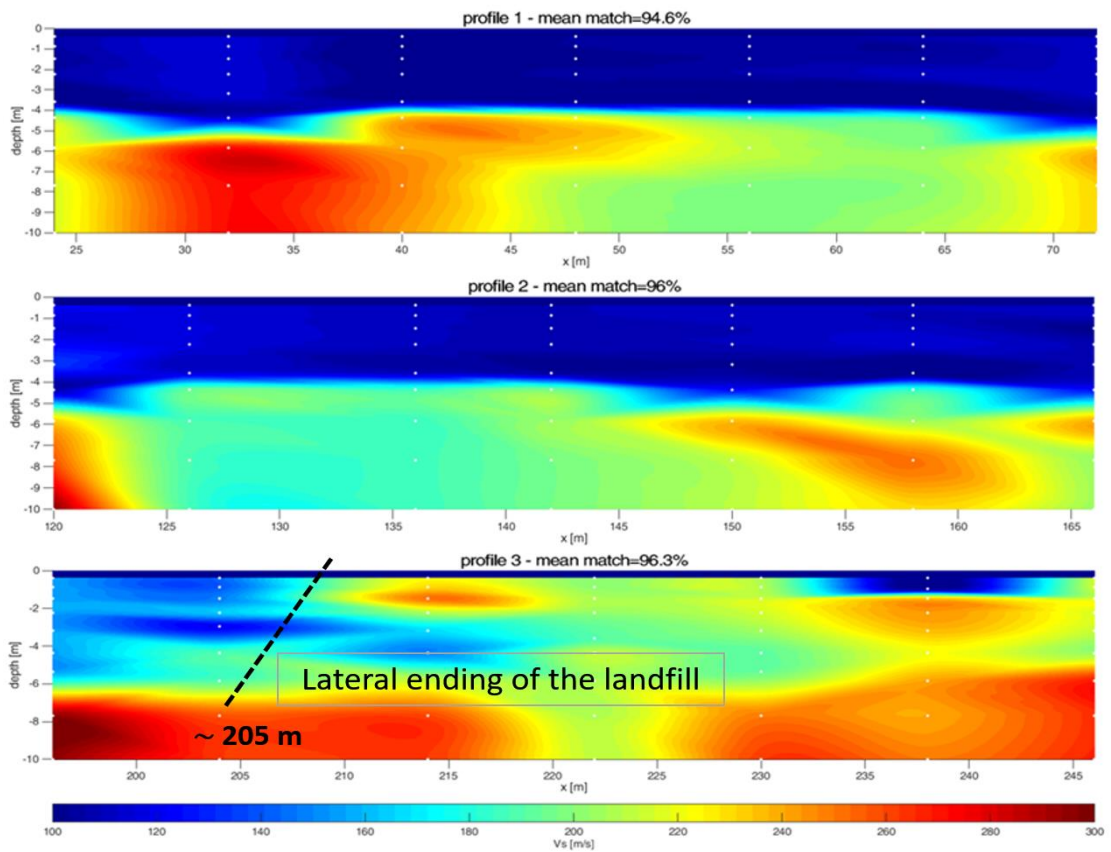


Fig. 6. 5, The three V_s sections obtained from the interpolation of each single 1D inversion, georeferenced to the ERT profile

Lastly, it is the case to remember the unlucky adopting of the seismic streamer, made inappropriate by the grass surface conditions of the landfill. Not having capitalized on his benefits has prevented a fast and wider coverage of the study area.

7 Conclusions

The combined use of different geophysical techniques and the joint interpretation of the acquired data has allowed to overcome the uncertainties due both to the complex site structure, both to the irresoluteness of single methods taken separately.

Dismissed landfills are difficult to characterize using direct investigations, above all concerning the risk to get worse the integrity of the bottom of the structure and to facilitate the spread of pollutant compounds. In this case, geophysics can obtain spatially distributed information over large areas with good resolution and lesser risks.

The investigation of the structure was conducted across through a detailed geophysical survey with the aim to define the composition and geometric characteristics of the Heferlbach's landfill.

In particular, ERT, IP and MASW measurements have been collected along a line crossing the eastern border of the landfill, in order to verify the thickness of the waste, evaluate the bottom surface and visualize possible preferential pathways of leachate in the underlying vadose zone.

The first two methods, well established for this kind of application, did not allow, however, to obtain a clear outcome for our study site. On the other hand, the role of surface waves is henceforth verified and widely reckoned in near surface applications, as geotechnical and environmental problems, to locate sharp V_s variations. It is important to emphasize that these velocities are only related to the solid matrix of the enlightened medium and not influenced by the fluid contents as V_p , thus showing the strength of this method to derive geometric and mechanical variations.

Instead, EMI measurements were conducted to mark lateral changes in subsurface and to get an aerial mapping of electrical apparent conductivity, with a faster and effective multi-depth acquisition and the need of few manpower. However, the method is susceptible to different sources of non-controllable noise (i.e. highly conductive materials that compose the soil, the existence of unknown clay lenses, asphalt, etc.).

Our results demonstrate the possibility to improve the interpretation of electrical conductivity images in complex situations, as landfills, by adding the information gained by means of the images of the surface waves.

Table of Figures

CHAPTER 1

FIG. 1. 1, HEFERLBACH LANDFILL IN MANNSWÖRTH, NIEDERÖSTERREICH, AND THE SOUTH-EAST INVESTIGATED AREA.....	8
FIG. 1. 2, AVERAGE DEPTH PROFILE OF THE LANDFILL HEFERLBACH, FROM BRANDSTÄTTER ET AL. 2013	9
FIG. 1. 3, SCHEMATIC EVOLUTION AND CONSEQUENT PRODUCTION OF LEACHATE AND BIOGAS IN HEFERLBACH LANDFILL.....	9
FIG. 1. 4, GENERAL PLAN OF THE HEFERLBACH LANDFILL, FROM BRANDSTÄTTER ET AL. 2016	10

CHAPTER 3

FIG. 3. 1, LEFT: 2D RADIATION PATTERN OF RAYLEIGH SURFACE WAVES GENERATED BY A VERTICAL POINT SOURCE. RIGHT: ELLIPTICAL POLARIZATION OF PARTICLE MOTION IN A RAYLEIGH WAVE IN A HOMOGENEOUS, LINEAR ELASTIC HALF-SPACE. AT THE FREE BOUNDARY, THE PARTICLE ORBIT IS RETROGRADE; AT DEPTH OF 0.2λ IT BECOMES PROGRADE. FROM FOTI, S., LAI, C. G., RIX, G. J., STROBBIA C., 2012.	18
FIG. 3. 2, MODAL CURVES IN F-K (A) AND F-V (B), F-K SPECTRUM (C) WITH A DOMINANT FIRST MODE, FROM A SYNTHETIC SEISMOGRAM (E). THE TWO SECTIONS OF THE SPECTRUM (D) SHOW THE LOWER ENERGY OF HIGHER MODES. FROM SOCCO, L.V, STROBBIA, C., 2004	20
FIG. 3. 3, SPHERICAL DIVERGENCE OF THE ENERGY. THE PROGRESSIVE DIMINUTION OF ENERGY PER UNIT AREA CAUSED BY SPHERICAL PROPAGATION FROM AN ENERGY SOURCE. FROM REYNOLDS, JOHN M., 2011.....	20
FIG. 3. 4, RELATION BETWEEN POISSON'S RATIO AND VELOCITY OF PROPAGATION OF COMPRESSION (P), SHEAR (S) AND RAYLEIGH (R) WAVES IN A LINEAR ELASTIC HOMOGENEOUS HALFSpace, FROM RICHART ET AL., 1962.....	21
FIG. 3. 5, AMPLITUDE RATIO VS. DIMENSIONLESS DEPTH FOR RAYLEIGH WAVE IN A HOMOGENOUS HALFSpace, FROM RICHART ET AL., 1970.....	21
FIG. 3. 6, GEOMETRIC DISPERSION OF RAYLEIGH WAVES: TRENDS WITH DEPTH OF THE VERTICAL PARTICLE MOTION ASSOCIATED WITH THE PROPAGATION OF TWO HARMONIC WAVES IN A LAYERED MEDIUM. FROM FOTI, S., LAI, C. G., RIX, G. J., STROBBIA C., 2012	22
FIG. 3. 7, FLOW CHART OF SURFACE WAVE TESTS, FROM FOTI, LAI, RIX, STROBBIA 2012	23
FIG. 3. 8, PARAMETER IDENTIFICATION ON THE BASIS OF GEOMETRIC DISPERSION. FROM FOTI, LAI, RIX, STROBBIA 2012... ..	24
FIG. 3. 9, COMBINATION OF ACTIVE AND PASSIVE SOURCE SURFACE WAVES MEASUREMENTS. FROM FOTI, S., LAI, C. G., RIX, G. J., STROBBIA C., 2012	25
FIG. 3. 10, SCHEMATIC VIEW OF THE ESSENTIAL FIELD EQUIPMENT: SOURCE, RECEIVERS AND DIGITAL ACQUISITION DEVICE. FROM FOTI, S., LAI, C. G., RIX, G. J., STROBBIA C., 2012	26
FIG. 3. 11, SCHEMATIC REPRESENTATION OF A MOVING COIL GEOPHONE: A COIL IS SUSPENDED IN A MAGNETIC FIELD AND ITS OSCILLATIONS GENERATE A CURRENT. FROM FOTI, S., LAI, C. G., RIX, G. J., STROBBIA C., 2012	27
FIG. 3. 12, GEODE EXPLORATION SEISMOGRAPHS FROM THE UNIVERSITY OF PADOVA, USED DURING THE FIELD WORK.....	27
FIG. 3. 13, SAMPLING OF A CONTINUOUS SIGNAL INVOLVES READING THE VALUES OF THE SIGNAL AT A FINITE DISCRETE SET OF POINTS. THE SAMPLED SIGNAL IS DEFINED ONLY AT A SERIES OF EVENLY SPACED TIME INSTANTS. FROM FOTI, S., LAI, C. G., RIX, G. J., STROBBIA C., 2012	28
FIG. 3. 14, AN EXAMPLE OF ALIASING IN THE TIME DOMAIN. FROM IFEACHOR, E.C., JERVIS, B.W., 1993.....	29
FIG. 3. 15, SCHEMATIC REPRESENTATION OF THE SW ACQUISITIONS	30
FIG. 3. 16, GEOPHONES ON LAND STREAMER, ADOPTED FOR THE FIRST ACQUISITION	31
FIG. 3. 17, SCHEMATIC REPRESENTATION OF THE LAST ACQUISITION WITH THE SUBSURFACE PORTION COVERED. FROM BARONE I.	31
FIG. 3. 18, ACQUISITION SCHEME OF EACH SINGE SECTION OF THE LAST PROFILE	32
FIG. 3. 19, ACQUIRED AND NORMALIZED SEISMOGRAMS FOR THE SHOT #1001: STANDARD AND WIGGLE PLOTS.....	33
FIG. 3. 20, FUNDAMENTAL AND HIGHER MODES IN THE F-K SPECTRUM	34
FIG. 3. 21, PICKING OF THE MAXIMA INTO THE F-K SPECTRUM AND THE RELATIVE DISPERSION CURVE.....	34
FIG. 3. 22, COMPARISON BETWEEN NORMAL AND REVERSE SHOTS FROM A SELECTION OF THE FIRST 24 GEOPHONES, RELATED TO THE SAME POSITION IN DEPTH AND BELONGING TO THE FIRST SECTION OF THE 01.06 PROFILE.....	35
FIG. 3. 23, INVERSION OUTPUT OF PARKSEIS. THE RED POINTS DENOTE THE INPUT VALUES FROM THE DISPERSION CURVE AND THE BLUE LINE IS THE V_s -DEPTH PROFILE OBTAINED.....	36
FIG. 3. 24, OVERALL INVERSION MATCHES.....	37

FIG. 3. 25, 2D VS TOMOGRAPHY OBTAINED BY LINEAR INTERPOLATION OF THE GATHERED INVERSIONS (BOXES BELOW) CONSTITUTING THE FIRST PROFILE P1	37
CHAPTER 4	
FIG. 4. 1, DEFINITION OF RESISTIVITY, FROM EVERETT, MARK E. 2013.	38
FIG. 4. 2, CONDUCTIVITY-RESISTIVITY VALUES OF VARIOUS GEOLOGICAL MATERIALS. MODIFIED AFTER PALACKY, G., 1987.	39
FIG. 4. 3, ELECTRICAL POLARIZATION AND MIGRATION MECHANISMS. FROM EVERETT, MARK E. 2013	39
FIG. 4. 4, ELECTRIC FIELD FOR A POINT CHARGE IN A HALF-SPACE. FROM TELFORD, W.M., GELDART, L.P., SHERIFF, R.E., 2010.....	42
FIG. 4. 5, CURRENT (C) AND POTENTIAL (P) ELECTRODES PLACED ON THE SURFACE OF A HOMOGENEOUS HALF-SPACE AND DISTRIBUTION OF THE CURRENT AND POTENTIAL LINES. FROM WARD, S. H., 1988	42
FIG. 4. 6, DC-RESISTIVITY DIPOLE - ON THE LEFT - AND QUADRUPOLE - ON THE RIGHT -. FROM CASSIANI, G. LECTURES.....	43
FIG. 4. 7, PRINCIPLE OF RESISTIVITY MEASUREMENT WITH A FOUR-ELECTRODES ARRAY IN A NONHOMOGENEOUS SYSTEM. FROM KNÖDEL, K., LANGE, G., VOIGT, H.J., 2007	43
FIG. 4. 8, EXAMPLE OF MOST POPULAR ELECTRODE CONFIGURATIONS IN RESISTIVITY AND INDUCED POLARIZATION SURVEYS. C AND P INDICATE RESPECTIVELY CURRENT AND POTENTIAL ELECTRODES. IT IS ALSO COMMON FOR THE GRADIENT AND SCHLUMBERGER ARRAYS TO USE A,B FOR THE CURRENT AND C,D FOR THE POTENTIAL ELECTRODES. MODIFIED AFTER SHARMA, P.V., 1997	45
FIG. 4. 9, PROPORTION OF CURRENT FLOWING BELOW A DEPTH Z (M); AB IS THE CURRENT ELECTRODE HALF-SEPARATION. FROM REYNOLDS, JOHN M., 2011	45
FIG. 4. 10, ELECTRICAL CONDUCTION MECHANISMS: A. ELECTRONIC - BY MATRIX, B. ELECTROLYTIC - BY PORE WATER AND C. SURFACE CONDUCTIVITY - BY GRAIN-WATER INTERFACE. FROM FLORES-OROZCO, A. LECTURES.....	46
FIG. 4. 11, ELECTRICAL DOUBLE LAYER. FROM FLORES-OROZCO, A. LECTURES.....	47
FIG. 4. 12, TDIP AND FDIP. FROM FLORES-OROZCO, A. LECTURES	47
FIG. 4. 13, ALTERNATING CURRENT INJECTION AND POTENTIAL DECAY. FROM FLORES-OROZCO, A. LECTURES	48
FIG. 4. 14, CHARGEABILITY. FROM FLORES-OROZCO, A. LECTURES	48
FIG. 4. 15, CHARGEABILITY VALUES OBSERVED IN DIFFERENT ROCKS. MODIFIED AFTER TELFORD, W.M., GELDART, L.P., SHERIFF, R.E., 2010	49
FIG. 4. 16, ELECTRICAL CONDUCTION AND INDUCED POLARIZATION EFFECT IN DIFFERENT EARTH MATERIALS. MODIFIED FROM FLORES-OROZCO, A. LECTURES	50
FIG. 4. 17, COMPLEX ELECTRICAL IMPEDANCE. FROM FLORES-OROZCO, A. LECTURES.....	50
FIG. 4. 18, REAL AND IMAGINARY COMPONENTS OF THE COMPLEX CONDUCTIVITY (Σ^*). FROM FLORES-OROZCO, A. LECTURES	52
FIG. 4. 19, LEFT: CURRENT INJECTION AS A SQUARE WAVE: ALTERNATING CURRENT AND IDEALIZED VOLTAGE FOR FIELD DC RESISTIVITY SURVEYS, WITH PRIMARY VOLTAGE (VP) AND SELF-POTENTIAL (VSP) EFFECTS. RIGHT-: REAL VOLTAGE WAVEFORM FOR MEASUREMENT OF TIME-DOMAIN INDUCED POLARIZATION. FROM BINLEY, A., KEMNA, A., 2005 ..	53
FIG. 4. 20, STUDY AREA IN MANNSWORTH, WITH THE RECONSTRUCTED LANDFILL SHAPE DEPICTED BY RED MARKER AND THE SYSCAL PROFILE AS A BLUE LINE. DOWNWARD, A SCHEMATIC REPRESENTATION OF THE ACQUISITION WITH THE NUMBER OF OVERLAPPED ELECTRODES FOR EACH SECTION.....	53
FIG. 4. 21, GEOELECTRIC EQUIPMENT AT THE TU-WIEN. FROM FLORES-OROZCO, A. LECTURES	54
FIG. 4. 22, MULTIPLE GRADIENT CONFIGURATION. FROM FLORES-OROZCO, A. LECTURES	54
FIG. 4. 23, ACQUISITION MOMENTS IN THE LANDFILL: THE RAINY CONDITIONS OF THE FIRST FIELD DAY ON THE LEFT AND THE FINAL AND THE DEFINITIVE DATA COLLECTION ON JUNE 1ST ON THE RIGHT	55
FIG. 4. 24, BUILDING OF A PSEUDOSECTION USING A WENNER ARRAY. FROM BINLEY, A., KEMNA, A., 2005.....	55
FIG. 4. 25, PSEUDOSECTIONS OF APPARENT RESISTIVITY AND PHASE OBTAINED FROM THE FIRST SEGMENT OF THE ROLL-ALONG	56
FIG. 4. 26, HISTOGRAMS OF THE APPARENT RESISTIVITY PA, MEASURED RESISTANCE R, AND APPARENT PHASE SHIFT Φ_A ALONG THE MEASURED PROFILE AT THE MANSWORTH LANDFILL USING MG MEASURING PROTOCOL. THESE SCHEMES ARE REFERRED TO THE TOTAL ROLLED PROFILE, COMPOSED BY FOUR SINGLE SECTIONS	57
FIG. 4. 27, MEASURED RESISTANCE R AND VOLTAGE V PLOTTED AGAINST APPARENT PHASE Φ	57
FIG. 4. 28, R AND Φ HISTOGRAMS AFTER FILTERING PROCEDURE	58
FIG. 4. 29, PSEUDOSECTIONS BEFORE AND AFTER THE FILTERING PROCESS	59

FIG. 4. 30, DEFINITION OF ELECTRICAL FORWARD AND INVERSE PROBLEM. FROM BINLEY, A., KEMNA, A., 2005.....	60
FIG. 4. 31, RESISTIVITY AND PHASE IMAGING RESULTS FROM MG DATA COLLECTED ALONG THE MANNSWORTH PROFILE ...	61
CHAPTER 5	
FIG. 5. 1, RESISTIVITIES OF SEDIMENTS AND ROCKS, AFTER TELFORD, W.M., GELDART, L.P., SHERIFF, R.E., 2010.....	62
FIG. 5. 2, THE PLANE WAVE SOLUTION OF MAXWELL’S EQUATIONS HAS THE B FIELD DIRECTLY PROPORTIONAL TO THE E FIELD AT EACH POINT, WITH THE RELATIVE DIRECTIONS SHOWN. FROM PHYS.LIBRETEXTS.ORG	63
FIG. 5. 3, REPRESENTATION OF FARADAY-LENZ (OR INDUCTION) AND AMPERE LAWS. FROM FLORES-OROZCO, A. LECTURES	64
FIG. 5. 4, SCHEMATIC ILLUSTRATION OF A LOOP-LOOP ELECTROMAGNETIC TARGET PROSPECTING. FROM EVERETT, MARK E. 2013	64
FIG. 5. 5, REPRESENTATION OF FIELD INJECTION AND DETECTION IN TX AND RX COILS. FROM FLORES-OROZCO, A. LECTURES	65
FIG. 5. 6, CLASSIFICATION OF ACTIVE EM SYSTEMS AS FUNCTION OF THE EMPLOYED FREQUENCY RANGE. FROM FLORES-OROZCO, A. LECTURES	66
FIG. 5. 7, SOURCE–RECEIVER SEPARATION COMPARED WITH THE TYPICAL WAVELENGTH DIMENSION. FROM REYNOLDS, JOHN M., 2011	66
FIG. 5. 8, PRIMARY AND SECONDARY FIELDS DETECTED IN RX COIL. FROM FLORES-OROZCO, A. LECTURES	68
FIG. 5. 9, REAL AND IMAGINARY COMPONENTS OF THE MAGNETIC FIELD, WITH THE LOW INDUCTION NUMBER ZONE INSIDE THE RED CIRCLE. FROM FLORES-OROZCO, A. LECTURES	69
FIG. 5. 10, DAMPING OF AN EM WAVE. FROM FLORES-OROZCO, A. LECTURES.....	70
FIG. 5. 11, FREQUENCY DEPENDENCE OF SKIN DEPTH FOR SOME DIFFERENT EARTH MATERIALS. FROM EVERETT, MARK E. 2013	71
FIG. 5. 12, CMD-EXPLORER USED IN THIS WORK, A PICTURE DURING ITS USE IN THE LANDFILL AND AN ILLUSTRATION TAKEN FROM THE GF INSTRUMENTS USER MANUAL.....	72
FIG. 5. 13, CMD EXPLORER ACQUISITION PATTERN. FROM GF INSTRUMENTS USER MANUAL	72
FIG. 5. 14, DISTRIBUTION OF MEASUREMENT POINTS FROM THE CMD-EXPLORER: THE AREA MAPPED (DIRECT -ORANGE- AND DIAGONAL -BLUE- LINES) AND THE LONGITUDINAL -RED- PROFILE, GEOREFERENCIATED AND PLOTTED IN QGIS.....	73
FIG. 5. 15, DIFFERENT Σ_A IMAGES FOR CONSECUTIVE DEPTH RANGES OF THE CMD-EXPLORER, GEOREFERENCIATED AND PLOTTED IN QGIS	74
CHAPTER 6	
FIG. 6. 1, INTERPOLATED MAPS OF Σ_A VALUES ACQUIRED FOR THE SIX COLLECTED DEPTH RANGES, VISUALIZED WITH MATLAB75	
FIG. 6. 2, APPARENT CONDUCTIVITY VALUES ALONG THE PROFILE ACQUIRED IN HI (LEFT) AND LO (RIGHT) MODE, GEOREFENCATED AND PLOTTED IN QGIS	76
FIG. 6. 3, PLOTS OF THE NORMALIZED SENSITIVITY FUNCTION FOR THE THREE DEPTH RANGES IN HI AND LO DEPTH RANGE FOR THE CMD-EXPLORER. FROM GF INSTRUMENTS: SHORT GUIDE FOR ELECTROMAGNETIC CONDUCTIVITY MAPPING AND TOMOGRAPHY	77
FIG. 6. 4, IMAGING RESULTS EXPRESSED IN TERMS OF THE REAL AND IMAGINARY COMPONENTS OF THE COMPLEX ELECTRICAL CONDUCTIVITY FOLLOWED BY PHASE PLOT, ALONG THE MANNSWORTH PROFILE. COURTESY OF FLORES-OROZCO	78
FIG. 6. 5, THE THREE V_s SECTIONS OBTAINED FROM THE INTERPOLATION OF EACH SINGLE 1D INVERSION, GEOREFERENCIATED TO THE ERT PROFILE	80

Bibliography

1. Abdel Aal et al., 2004. Effects of microbial processes on electrolytic and interfacial electrical properties of unconsolidated sediments.
2. Aki, K., Richards, P.G., 1980. Quantitative Seismology: Theory and Methods, Vol. I and II. (W.H. Freeman, San Francisco)
3. Archie, G.E., 1942. The electrical resistivity log as an aid in determining some reservoir characteristics. (Transactions of the AIME)
4. Atekwana et al., 2004. Evidence for microbial enhanced electrical conductivity in hydrocarbon-contaminated sediments. (GEOPHYSICAL RESEARCH LETTERS)
5. Atekwana et al., 2019. Geophysical Signatures of Microbial Activity.
6. Binley et al., 1995. Regularized image reconstruction of noisy electrical resistance tomography data. (Process Tomography)
7. Binley, A., Kemna, A., 2005. DC Resistivity and Induced Polarization methods. (In: Rubin Y., Hubbard S.S. (eds) Hydrogeophysics. Water Science and Technology Library, Springer)
8. Brandstätter et al., 2013. Site specific in-situ aeration completion criteria: case study "Heferlbach".
9. Brandstätter et al., 2016. In situ Belüftung von Deponien in Feld und Labor: Projekt "Heferlbach".
10. Busato, L., 2017. Non-invasive monitoring and numerical modeling of the soil-plant continuum. (PhD thesis)
11. Cassiani, Giorgio. Course materials provided by lectures. Dipartimento di Geoscienze, Università degli Studi di Padova, A.Y. 2018/2019.
12. Constable, S.C., 1987. Occam's inversion: A practical algorithm for generating smooth models from electromagnetic sounding data. (Geophysics)
13. Davis et al., 2006. Microbial growth and biofilm formation in geologic media is detected with complex conductivity measurements.
14. Everett, Mark E. 2013. Near-Surface Applied Geophysics. (Cambridge University Press)
15. Flores-Orozco et al., 2011. Using complex resistivity imaging to infer biogeochemical processes associated with bioremediation of a uranium-contaminated aquifer. (Journal of Geophysical Research)
16. Flores-Orozco et al., 2012. Data error quantification in spectral induced polarization imaging. (Geophysics)
17. Flores-Orozco et al., 2018. Complex-conductivity imaging for the understanding of landslide architecture. (Engineering Geology)
18. Flores-Orozco et al., 2018. Decay curve analysis for data error quantification in time-domain induced polarization imaging. (Geophysics)
19. Flores-Orozco, Adrian. Course materials provided by lectures. Department of Geodesy and Geoinformation, TU-Wien, A.Y. 2018/2019.
20. Foti, S., Hollender, F., Garofalo, F. et al., 2018. Guidelines for the good practice of surface wave analysis: a product of the InterPACIFIC project. (Bull Earthquake Engineering)
21. Foti, S., Lai, C. G., Rix, G. J., Strobbia C., 2014. Surface wave methods for near-surface site characterization. (CRC press, Taylor & Francis group)
22. Gallistl et al., 2018. Delineation of subsurface variability in clay-rich landslides through spectral induced polarization imaging and electromagnetic methods.
23. GF Instruments, 2016. Short guide for electromagnetic conductivity mapping and tomography.

24. Hashemi, J.M., Boaga, J., Petronio, L., Perri, M.T., Strobbia, C., Affattato, A., Romero, R., Cassiani, G., 2019. Detection of lateral discontinuities via surface waves analysis: A case study at a derelict industrial site. (Journal of Applied Geophysics)
25. Ifeachor, E.C., Jervis, B.W., 1993. Digital Signal Processing: A Practical Approach. (Pearson Education Ltd.)
26. Ivanova A., 2017. Geoelectrical characterization of a landfill ongoing aeration. (Bachelor thesis)
27. Kemna et al., 2012. An overview of the spectral induced polarization method for near-surface applications. (Near Surface Geophysics)
28. Knödel, K., Lange, G., Voigt, H.J., 2007. Environmental Geology. Handbook of field methods and case studies. (Springer)
29. Lai, C. G., Wilmanski, K., 2005. Surface Waves in Geomechanics: Direct and Inverse Modelling for Soils and Rocks. (Springer)
30. Long, T. L., 2002. Seismic surface-wave tomography of waste sites. (Georgia Institute of Technology, US)
31. McNeill, J.D., 1980. Electromagnetic terrain conductivity measurement at low induction numbers. (Technical note TN-6, Geonics limited)
32. Miller et al., 1955. On the partition of energy between elastic waves in a semi-infinite solid. (The Royal Society publishing)
33. Nafe, J.E., Drake, C.L., 1957. Variation with depth in shallow and deep water marine sediments of porosity, density and the velocities of compressional and shear waves. (Geophysics)
34. Nazarian, S., Stokoe, K.H., 1984. Nondestructive testing of pavements using surface waves. (Transportation Research Record)
35. Paap et al., 2010. Characterization of landfills using a multidisciplinary approach.
36. Palacky, G., 1987. Resistivity Characteristics of Geological Targets. (In: Nabighian, M., Ed., Electromagnetic Methods in Applied Geophysics-Theory, Society of Exploration Geophysicists)
37. Park et al., 1999. Multichannel analysis of surface waves. (Geophysics)
38. Park et al., 2001. Seismic Characterization of Geotechnical Sites by Multichannel Analysis of Surface Waves (MASW) Method. (Kansas Geological Survey)
39. Park et al., 2001. "Seismic characterization of geotechnical sites by multichannel analysis of surface waves (MASW) method." (Tenth International Conference on Soil Dynamics and Earthquake Engineering (SDEE), Philadelphia)
40. Park, Choon B., 2005. "MASW horizontal resolution in 2D shear-velocity (V_s) mapping." (Open-File Report, Lawrence: Kansas Geologic Survey)
41. ParkSEIS©: <http://www.parkseismic.com/ParkSeis.html>
42. Peruzzo, L., 2015. Caratterizzazione geofisica di un tratto d'argine ricostruito in seguito a rotta. (MSc thesis)
43. Rayleigh, L., 1885. On Waves Propagated along the Plane Surface of an Elastic Solid. (London Mathematical Society)
44. Reynolds, John M., 2011. An introduction to Applied and Environmental Geophysics. (John Wiley & Sons)
45. Richart et al., 1962. Foundation vibrations. (Transactions of the American Society of Civil Engineers)
46. Richart et al., 1970. Vibrations of soils and foundations. (Prentice-hall, Inc)
47. Sanchez-Sesma, F. J. et al., 2011. Energy Partitions among Elastic Waves for Dynamic Surface Loads in a Semi-Infinite Solid. (Bulletin of the Seismological Society of America)
48. Sharma, P.V., 1997. Environmental and Engineering Geophysics. (Cambridge University Press)

49. Slater, L., Binley, A., 2006. Synthetic and field-based electrical imaging of a zerovalent iron barrier: Implications for monitoring long-term barrier performance. (Geophysics)
50. Socco et al., 2010. Surface-wave analysis for building near-surface velocity models. Established approaches and new perspectives. (Geophysics)
51. Socco, L.V, Strobbia, C., 2004. Surface-wave method for near-surface characterization: a tutorial. (Near Surface Geophysics)
52. Sogade et al., 2006. Induced-polarization detection and mapping of contaminant plumes. (Geophysics)
53. Soupios et al., 2007. Application of integrated methods in mapping waste disposal areas.
54. Telford, W.M., Geldart, L.P., Sheriff, R.E., 2010. Applied Geophysics. (Cambridge University Press, 2nd edition)
55. Valtl, M., 2005. Altablagerung "Heferlbach": Gefährdungsabschätzung und Prioritätenklassifizierung.
56. Ward, S. H., 1988. The resistivity and induced polarization methods. In "Symposium on the Application of Geophysics to Engineering and Environmental Problems", 1988. (Society of Exploration Geophysicists)
57. Wyllie et al., 1958. An experimental investigation of factors affecting elastic wave velocities in porous media. (Geophysics)